

AD 639 057

CALIFORNIA INSTITUTE OF TECHNOLOGY

CIT - ELECTRON TUBE & MICROWAVE
LABORATORY REPORT

A NONLINEAR STUDY OF
BEAM PLASMA AMPLIFICATION

by

Robert L. Poeschel

Technical Report No. 33

Nonr 220(50)

SEPTEMBER 1966

CALIFORNIA
INSTITUTE OF

OCT 16 1975

TECHNOLOGY

A REPORT ON RESEARCH CONDUCTED UNDER
CONTRACT WITH THE OFFICE OF NAVAL RESEARCH

A NONLINEAR STUDY
OF BEAM PLASMA AMPLIFICATION

Robert L. Poeschel

Technical Report No. 33

September 1966

Research sponsored
by the U. S. Office of Naval Research
Contract Nonr 220(50)

California Institute of Technology
Pasadena, California

-iii-
ABSTRACT

The interaction between an electron beam and the plasma oscillations it excites in traversing a plasma region effectively changes the magnitude and direction of the force between beam electrons. This effect has been studied theoretically and experimentally by computing and observing beam electron velocities and phases for a beam which is initially velocity modulated at frequency ω and allowed to drift through a plasma filled region of plasma frequency ω_p . When $\omega > \omega_p$ the force between electrons is repulsive and effectively increases in magnitude as ω approaches ω_p . When $\omega < \omega_p$, the force between electrons becomes a force of attraction, to within a given inter-electron spacing, and the maximum effect is also at the resonance condition $\omega \sim \omega_p$. This property could be used to improve the efficiency of electron bunching in a klystron type amplifier by filling the drift space with a plasma of appropriate density.

The beam behavior is studied theoretically by computing in an exact, nonlinear manner, the trajectories of a disc model electron beam which traverses a linear, dielectric model plasma. The parameters varied are the beam space charge conditions (beam current), the degree of initial velocity modulation, and the ratio of modulation frequency to plasma frequency (ω/ω_p). Computations show that it is possible to bunch the beam electrons to within 85% of delta function bunching under some beam and plasma conditions. The electron beam behavior is studied experimentally by observing the beam electron velocity phase distribution with a crossed-field velocity analyzer, and observing the beam current waveform (density-phase distribution) using a wide-band

sampling oscilloscope. Experimental results show essentially the same beam behavior as predicted by the computations with some differences which are attributed to variation in the plasma density along the beam path.

CONTENTS

I	INTRODUCTION	1
	A. Definition and Discussion of the Problem	1
II	THEORETICAL METHOD	5
	A. Model and Assumptions	5
	B. Application of Theory to Computations	10
III	EXPERIMENTAL METHOD	14
	A. Experimental Approach to the Problem	14
	B. Experimental Apparatus	16
	C. Method of Collecting and Analyzing Data	26
	D. Characteristics of the Experiment	30
IV	RESULTS	38
	A. Theoretical Results	38
	B. Experimental Results	65
V	CONCLUSIONS	81
	A. Summary and Conclusions	81
	B. Suggestions for Further Work	85
	APPENDIX A - The Equations of Motion	86
	B - The Acceleration Force Law	92
	C - The Computer Program	103
	REFERENCES	106

I. INTRODUCTION

A. Definition and Discussion of the Problem

The purpose of this investigation is to study the nonlinear behavior of a velocity modulated electron beam interacting with a plasma. The interaction of interest is between the beam electrons and the plasma oscillations which they excite. This interaction was first predicted by Bohm and Gross (1) and numerous attempts to observe their predictions followed. Boyd, Field and Gould (2),(3) succeeded in observing these interactions and extended the theory to include finite geometry effects. Other investigators reported similar findings (4), (5) but the agreement between theory and experiment was in all cases rather qualitative. In these and other investigations too numerous to mention, attention is focused on the interaction between the electron beam and the "slow" plasma wave which it excites. This widespread interest in the plasma wave interaction is principally due to the high gain which is predicted theoretically when the slow wave structure of a traveling wave amplifier is replaced by a plasma column. The use of a plasma column for this purpose would also eliminate the structural problems which arise at millimeter wavelengths. A major difficulty in using this type of interaction is electron beam coupling--both between the beam and the input-output circuit, and between the beam and the plasma surface wave. Gould and Allen (6) have shown theoretically that the gain and efficiency of a klystron type amplifier can be improved by filling, or partially filling, the drift space with a plasma of appropriate density. Chorney (7) has reported measurements

on a klystron type beam-plasma amplifier which support these computed predictions. In this configuration the plasma acts as an inductive medium, rather than a slow wave structure. The effect is a volume effect which modifies the force between electrons causing them to attract instead of repel.

In investigations which deal with amplification and efficiency in beam type devices, the efficiency of the circuit used to couple the signal to and from the beam is difficult to assess, especially in the presence of a plasma. Consequently investigations which measure these parameters are only capable of indirectly determining the processes which occur in the beam-plasma interaction. For this reason, this investigation does not consider input-output properties, but instead the beam electron properties: electron velocities and currents as functions of position and time. The problems considered are concerned with the amplification or bunching processes rather than with amplifiers, and hence no attempt is made to solve coupling problems or to explore and optimize amplification or gain.

The model considered in this investigation is essentially the configuration of a klystron type amplifier with a plasma partially filling the drift region, and with no output coupler. The analytic study employs the analysis and computational method of Gould (6) which treats the electron beam in an exact, nonlinear manner, while considering the plasma to be a linear, dielectric medium whose properties depend on the plasma density, electron temperature, and collision frequency. This analysis provides information about the beam electron velocities and crossing times (or phase) as a function of drift position. The

experimental investigation provides measurements of beam electron velocity and phase at the point of beam collection. The effects of the beam-plasma interaction on the plasma are not observed in either the theoretical study or the experimental measurements.

Both the theoretical computations and the experimental measurements provide results in the same form. The computational method represents the electron beam by a finite number of charged discs and the result of the computation is the velocity and crossing time (phase) for each disc as a function of drift distance. These results are translated into velocity versus phase plots with drift distance as a parameter. The number of discs having phases (crossing times) within a specified phase interval corresponds to the bunching (current modulation) of the beam. Experimentally, the velocity and phase of the beam electrons are determined by allowing a portion of the beam to pass through the collector into a velocity sensitive deflection system. The phase (or time of entering the deflection system) is obtained by synchronously deflecting the beam at a sub-multiple of the velocity modulation frequency. In this manner the velocity and phase of the beam electrons can be obtained from the deflection observed on a phosphored screen. The bunching of the beam is measured by observing the current waveform with a 50 ohm terminated probe located near the beam collector, and a sampling oscilloscope. When the computed bunching information (number of discs per phase interval) is translated into a current waveform, the theoretical and experimental results can be compared directly for the drift distance corresponding to the plane of the collector.

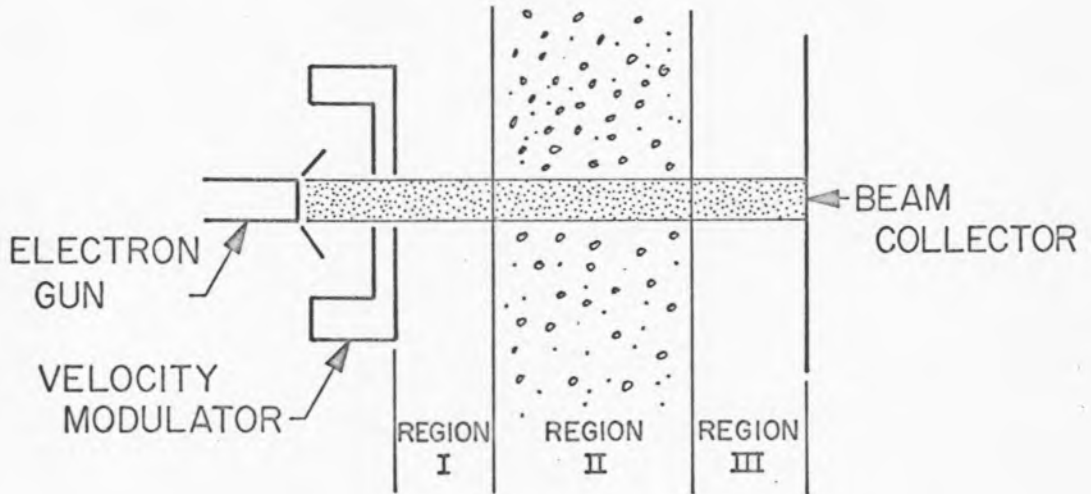
The theoretical method has some advantages over the experiment in that the velocity-phase information can be obtained at as many points along the drift path as desired, and the effects of varying one parameter at a time are observed. Consequently, computations are made to determine the effects of beam space charge forces, plasma space charge forces and their dependence on the plasma properties, and the initial velocity modulation of the beam. The experimental study also explores the effects of beam space charge forces, plasma space charge forces, and initial velocity modulation over a somewhat smaller range of values. The comparison between computed results and experimental results is only partially quantitative due to difficulty in assessing experimental parameters. This is due to several facts. The plasma is--for the most part--beam generated, there is no feasible means available for independently determining the plasma density, and the beam and plasma parameters cannot be varied independently. Enhanced bunching is observed, however, and the observed similarities and differences in the computed and experimental results can be explained by a plasma density variation along the beam path.

II. THEORETICAL METHOD

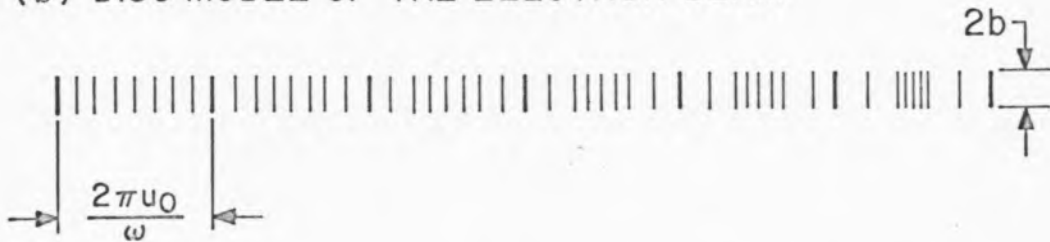
A. Model for the Theoretical Computations

The model for the beam-plasma amplifier analyzed by Gould (6) is shown in Figure 2.1a. An electron beam is velocity modulated at frequency ω and allowed to drift to the point of collection as shown. The drift region is divided into three parts. Regions I and III are evacuated, and Region II contains a uniform, warm plasma characterized by a plasma frequency ω_p , a collision frequency ν , and an electron thermal speed w . The electron beam is described analytically by the method of Tien et al (9), and Webber (10) as a series of N charged discs per modulation cycle. The discs have a charge q , a finite radius b , and are considered to be rigid and move only in the axial z direction with an average velocity u_0 . Figure 2.1b shows pictorially the disc representation of such a velocity modulated beam as it would look at a given instant of time. Each cycle extends over an electronic wavelength ($2\pi u_0/\omega$). It is seen that as the beam progresses along its path (to the right) there is a tendency for the discs to bunch near the center of the cycle which is easily explained in terms of simple ballistics in the absence of space charge effects. The model shown in Figure 2.1b would appear exactly the same at a time $2\pi/\omega$ later, except each cycle would be shifted a distance $2\pi u_0/\omega$ to the right. Using this model, the trajectory of each disc can be computed by writing its equation of motion in terms of a summation of the forces exerted on the disc in question by all the other discs. Thus for the n th disc, the basic equations are

(a) MODEL FOR BEAM PLASMA AMPLIFIER



(b) DISC MODEL OF THE ELECTRON BEAM



(c) MODEL FOR SUMMING ACCELERATION FORCE A_{nm}

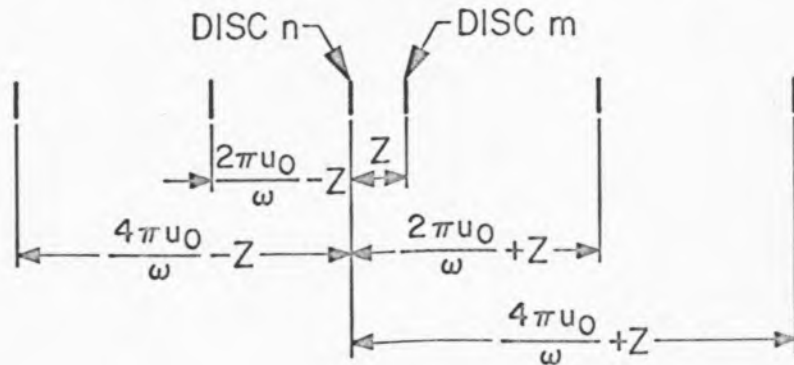


Figure 2.1 Models for the Theoretical Analysis

$$\frac{dv_n}{dt} = \sum_{n \neq m}^N a_{nm} \quad (2.1)$$

$$\frac{dz_n}{dt} = v_n \quad (2.2)$$

where v_n and z_n are the velocity and position of disc n and a_{nm} is the force due to disc m and its counterparts (as seen in Figure 2.1c) which accelerate disc n .

In the vacuum region the force f_{nm} between a test disc n and a disc m has been shown by Tien (8) to have a particularly simple form

$$f_{nm} = \frac{q^2}{2\pi\epsilon_0 b^2} e^{-\frac{2}{b}z} \quad (2.3)$$

where q and b are the charge and radius of the disc, and z is the separation between disc n and disc m seen in Figure 2.1c ($z = |z_n - z_m|$). By summing up the contributions due to the counterparts of disc m , the acceleration force a_{nm} can be expressed in simple exponential form, as seen in Appendix B. In the plasma region the force between discs cannot be expressed in a simple analytic form due to the complicated way in which the potentials of the beam excited plasma oscillations modify the coulomb force, and therefore must be computed numerically. This computation makes use of a technique similar to that used by Bohm and Pines (11) in calculating the energy lost by fast particles traveling through a plasma (the so-called plasma Cherenkov effect). This method describes the

plasma by a dielectric constant and makes extensive use of Fourier transforms.

The equations of motion, their normalization, and the computational methods are discussed in Appendix A, with Appendix B being devoted to discussion of the acceleration force computations. The normalized independent variable becomes the drift distance Z , and the normalized dependent variables become the disc velocity $V_n(Z)$ and the disc crossing time at position Z , $T_n(Z)$. The crossing time can be interpreted as the phase of disc n relative to the disc belonging to the same modulation cycle which was emitted at $t = 0$ with the average velocity $v = u_0$. As defined in Appendix A, Z is measured in units of the electronic wavelength $2\pi u_0/\omega$, $V_n(z)$ in units of u_0 , and $T_n(z)$ in units of $1/\omega$. Thus the theoretical approach supplies the disc (electron) velocity and crossing time (phase) as a function of the drift distance.

The disc model chosen for the electron beam allows an exact, nonlinear description of the motion of the discs representing the beam but allows no transverse motion of the beam electrons. This assumption implies the presence of a large magnetic field, but the effect of the magnetic field on the interaction is not included. The step by step integration procedure used requires the evaluation of forces arising from discs which are ahead of the point of integration and errors will be introduced if the velocity or phase of the discs varies greatly from its counterpart in adjacent modulation cycles. This does not seem to be a serious restriction since the method has been successful in the

analysis of Tien et al, and Webber. The use of Fourier transforms in describing the plasma requires that the plasma remain linear, as does the use of equation 2.1 in the plasma region. This is not a serious restriction since, in the small signal theory, the higher order terms become significant in the beam equations at much smaller signals than in the plasma equations. Gould has shown that the condition which must be met is

$$\left(\frac{\beta_e - \gamma}{\gamma}\right)^2 \ll 1 \quad (2.4)$$

where $\beta_e = \omega/u_0$, and γ is the propagation constant for the space charge waves excited by the beam electrons. In short, the growth constant must not be too large. This is not a serious restriction for this study, since the behavior of the beam electrons becomes highly nonlinear before this condition is violated. This is reasonable on physical grounds, since the restoring forces in the plasma are greater than those in the beam, while the same fields act on both. For convenience in integrating the acceleration force and the equations of motion, the plasma is also assumed to be isotropic, homogeneous, and to have sharp boundaries. Reflections from the axial and radial boundaries are neglected since the plasma oscillations which are of interest here diffuse away from the point of excitation slowly (at plasma electron thermal speed) and are rapidly damped out by a relatively small number of collisions. The effect of the magnetic field is neglected in the plasma description and to justify this $\omega_p \gg \omega_{ce}$ where ω_{ce} is the electron cyclotron frequency. For the assumption

of confined axial flow in the electron beam $\omega_{ce} \gg \omega_{pb}$ where ω_{pb} is the electron beam plasma frequency. Thus the condition on the magnetic field is

$$\omega_{pb} \ll \omega_{ce} \ll \omega_p \quad (2.5)$$

which is not usually well satisfied in the experimental configuration. Nevertheless, the magnetic field is neglected in the analysis for simplicity's sake.

B. Application of Theory to Computation

The theoretical approach outlined in the previous section and discussed in detail in Appendices A and B has been utilized in a rather versatile computer program by Gould, as discussed in some detail in Appendix C. The computer program, written for the IBM 7094, permits variation of the drift length, the beam properties, the initial velocity modulation, and the plasma properties by means of the input data. The initial beam condition (velocity modulation) may either be computed or read in from cards. Since the acceleration force term cannot be expressed analytically in the plasma region, it would be necessary to numerically evaluate a rather complicated integral expression each time the acceleration force is needed in integrating the equations of motion. Rather than do this, an acceleration force law table is computed for the plasma parameters specified in the input data by evaluating the acceleration force integral for a set of disc spacings (also determined by the input data). The acceleration force table values are punched on cards for future use, and the program is

written so as to bypass the force table computation and read a set of force table values from data cards for appropriate input data. Thus in integrating the equations of motion in the plasma region, the acceleration force term is evaluated by a "table look-up" procedure using quadratic interpolation--considerably decreasing the computation time.

The numerical computation has several forms of output. The principal outputs are the values of normalized velocity V , and relative phase T , (really T' as defined in Appendix A) for each disc. These values are printed out at intervals of the drift distance Z , specified by the input data and punched on cards at the final Z position. The Fourier components of the current are computed at each print-out position using the expression

$$I(t) = \frac{I_0}{N} \sum_{i=1}^N V_i \delta(\omega t - T_i) \quad (2.6)$$

$$= \sum_{n=0}^{\infty} A_n \cos n\omega t + B_n \sin n\omega t \quad (2.7)$$

The Fourier coefficients are evaluated in the usual manner and the normalized Fourier current components are given by

$$I_n = (A_n^2 + B_n^2)^{1/2} \quad (2.8)$$

The first three components are computed and printed out with the V and T data. The $T_i(Z)$ are continuously plotted as a function of Z , one curve for each disc, providing a sort of "smear camera" record.

of the relative phases (or positions) of the discs in one modulation cycle as it progresses along its path. These plots clearly indicate the crossover points (points at which faster discs overtake slower ones) and add considerable insight into the beam behavior. In addition to Gould's basic program, the T_i are used to compute a normalized current waveform, e.g. $I(t)/I_0$. This is done by smearing out the axial dimension of the charged disc to a gaussian rather than δ function shape. Thus in terms of the relative phase

$$\frac{I(t)}{I_0} = k \sum_{i=1}^N e^{-\left(\frac{\omega t - T_i}{\tau}\right)^2} \quad (2.9)$$

where τ is the rise time of the measuring device and k is the normalizing constant which makes $I/I_0 = 1$ when the discs are equally spaced in phase (or distance) and is a function of both N and τ . This computation is useful, mainly, for comparison with the experimentally measured current.

The computer program is well suited for use in varying plasma, electron beam, and geometric parameters for the purpose of optimizing the beam bunching or amplification process if the axial plasma density distribution is uniform. If, as in reality, there is an axial plasma density variation, but negligible radial density variation in the region of the beam, the plasma region can be further subdivided into several regions each represented by the average plasma density for that region. This technique has been used by Allen (6) and Chorney (7) in efforts to construct a practical beam plasma amplifier, and in this investigation to assess the effects of the presence of an axial plasma

density profile. While this technique partially accounts for the axial variation in the plasma frequency and the consequent change in the acceleration forces, the neglect of the axial boundary conditions becomes more serious. As was shown by Nickel, Parker and Gould (8), the presence of a density profile gives rise to resonance oscillations, thus by neglecting reflections at axial boundaries, both the conditions for which these resonance oscillations occur and their influence on the beam behavior are completely overlooked. Hence the observed behavior may be radically different from that predicted using this technique. While it is almost certain that the experimental plasma has an axial density variation, the theoretical computational study uses a uniform plasma region. Furthermore, the range of parameters used in the computations is limited, for the most part, to the range achievable in the experiment. This is primarily due to the computer time required--approximately two and one-half minutes per set of parameters.

The theoretical results are thus obtained in the form of point plots of the normalized velocity V versus the relative phase T for each of the N discs in a modulation cycle as a function of the drift distance Z . The spacing (in phase) between the points gives a visual indication of the degree of bunching, and the normalized fundamental Fourier component I_1/I_0 and the current waveform $I(\omega t)/I_0$ add quantitative information. The plots of $T_i(Z)$ versus Z , referred to as phase trajectories, have no experimental counterpart, but are valuable in that they portray at a glance, the beam behavior over its entire path.

III. EXPERIMENTAL METHOD

A. The Experimental Approach

The experimental apparatus is designed to correspond, as nearly as possible, to the theoretical model used in the computational study. Since this analysis concentrates on the behavior of the beam electrons (discs), the experimental approach is concerned only with measurement of the electron beam properties. The experimental model is essentially the same as the theoretical model of Figure 2.1a with Regions I and III being very short. The experimental apparatus is shown pictorially in Figure 3.1. The electron beam is velocity modulated by the re-entrant cavity and drifts through a Penning discharge plasma region. At the point of beam collection, two beam properties are measured as functions of time--beam electron velocity and beam electron current or density. In the theoretical approach these quantities are computed as a function of drift distance along the beam path, but this is not feasible experimentally, and comparison with theory can be made for only one position. The electron velocity is measured by allowing a small portion of the beam to pass through the collector and into a time resolved, cross-field velocity analyzer which is synchronized to the modulation frequency. The beam current is sampled by collecting a portion of the beam with a 50 ohm terminated probe and a sampling oscilloscope. These quantities are measured as functions of electron beam current, initial velocity modulation, magnetic field, background pressure, and Penning discharge current. No attempt is made to change the geometry of the experiment or to optimize the amplification

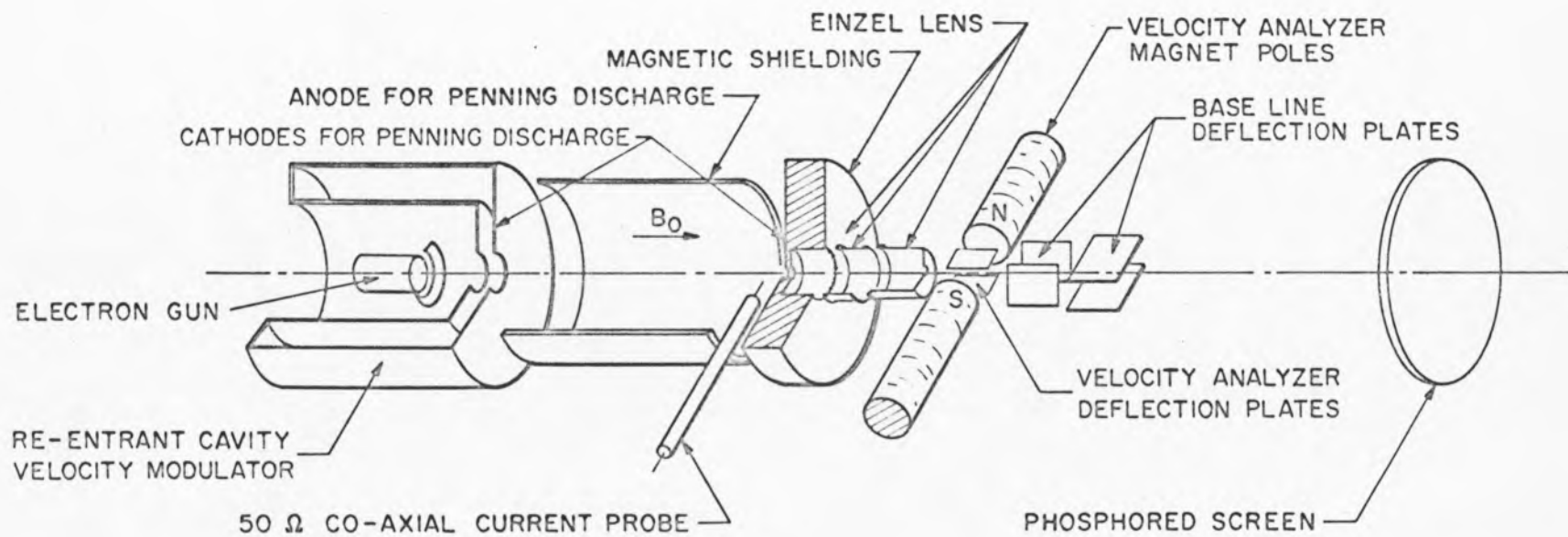


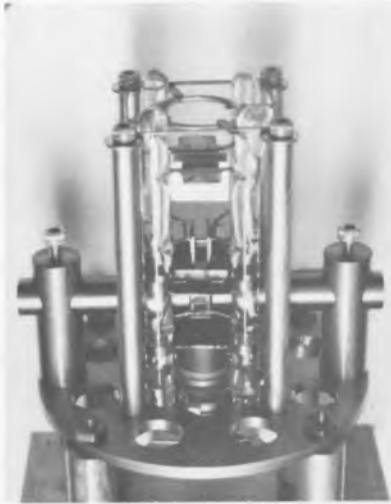
Figure 3.1 Pictorial Drawing of Experimental Apparatus

conditions.

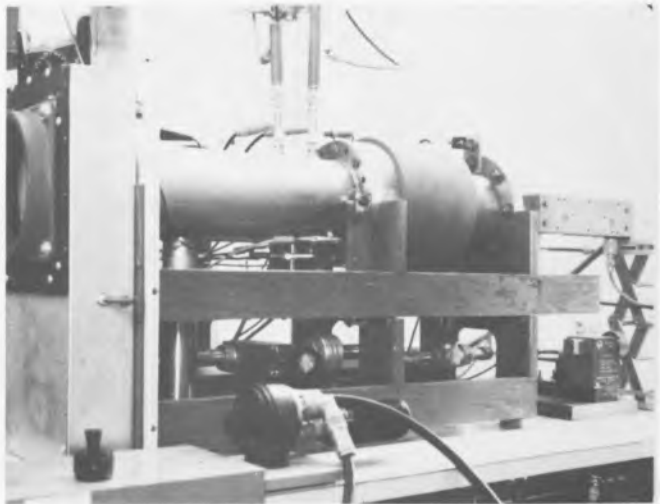
B. The Experimental Apparatus

While the experimental model is conceptually simple, the experimental apparatus is a rather complex assembly of vacuum apparatus, electronics, and instrumentation. The basic components shown pictorially in Figure 3.1 can be grouped in two categories, the beam-plasma interaction components, and the velocity analyzer components. These components are separated in Figure 3.1 by the component labeled "magnetic shielding". This component actually divides the vacuum chamber which supports, aligns and encloses the components of Figure 3.1 into a beam-plasma vacuum chamber and a velocity analyzer vacuum chamber. The velocity analyzer deflection system sub-assembly is shown in photograph (a) of Figure 3.2, the beam-plasma interaction components and the mounting flange which provides alignment are shown in photograph (c), and the vacuum container is shown in photograph (b). The flange seen near the center of the cylinder is the dividing plane for the two chambers, the beam-plasma interaction chamber lies to the right, the velocity analyzer chamber lies to the left as viewed in photograph (b). By closing the valve seen in the lower center of (b) the two chambers are isolated except for the small beam sampling hole which is 0.127 mm (0.005 in.) in diameter. Thus the chambers may be maintained at different pressures by admitting gas into the beam-plasma chamber with the leak valve seen in the lower right-hand corner of photograph (b). The pressure in the beam-plasma region is monitored with a Bayard-Alpert type ionization gauge. The axial

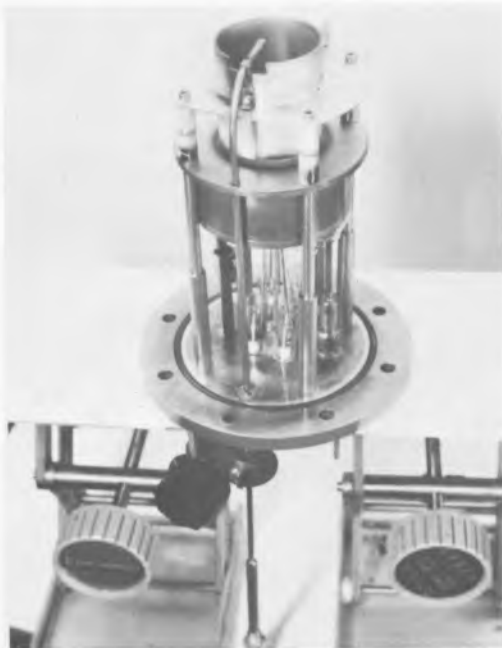
(a)



(b)



(c)



(d)



FIGURE 3.2 PHOTOGRAPHS OF EXPERIMENTAL APPARATUS.

- (a) Velocity Analyzer Deflection System Sub-Assembly
- (b) Close-Up of Vacuum Chamber which Contains the Apparatus
- (c) Components of the Beam-Plasma Interaction Region and Mounting Flange
- (d) Complete Experimental Apparatus and Instrumentation

magnetic field B_0 is required both for collimation of the electron beam and operation of the Penning discharge. It is provided by an external solenoid which is aligned mechanically to the cylindrical vacuum wall. The axial field is prevented from penetrating the velocity analyzer region by iron shielding material. The magnetic field is operated in the range 100 to 200 gauss in order to satisfy the condition

$$\omega_{pb} < \omega_c < \omega_{pp} \quad (3.1)$$

where ω_{pb} is the electron beam plasma frequency, ω_c is the electron cyclotron frequency and ω_{pp} is the plasma frequency of the plasma filling the drift region.

The electron beam is formed by an electron gun which is normally operated at one kilovolt accelerating potential with current variable from a few microamperes to fifteen milliamperes, and has a beam diameter of four millimeters. The electron gun is a rectilinear flow type with a barium impregnated cathode and is fully immersed in the axial magnetic field B_0 . The beam current is controlled by varying the bias voltage on a control electrode, for small changes, and by varying the cathode temperature. At the maximum beam current the beam plasma frequency is 180 mc ($\omega_{pb}/2\pi$) and the beam space charge wavelength λ_g is 30.4 cm. Since the drift length L from the point of velocity modulation to the beam collector is only 5.84 cm, the maximum ratio L/λ_g is 0.19 --less than a quarter space charge wavelength.

The velocity modulation cavity was designed to resonate at 1100 mc using the data given in Moreno (12). The dimensions of the

cavity in Moreno's notation are $\rho_2 = 3.73$ cm, $\rho_1 = 1.91$ cm, $Z_0 = 2.96$ cm, and $\delta = 0.3$ cm. The cavity is tunable by ± 5 mc by varying the depth of insertion of a tuning slug. Power is fed into the cavity from a 50 ohm transmission line by a loop type coupler which was adjusted to give a minimum V.S.W.R. of 1.18 at the resonant frequency 1100 mc. Using the V.S.W.R. method of Ginzton (13) the cavity was determined to be slightly under-coupled with a coupling coefficient $\beta = 0.85$ and the quality factors $Q_L = 1235$, $Q_0 = 2615$ and $Q_{ext} = 2970$. These parameters were measured with a 1 ma beam current passing through the modulation gap.

In the design of the experimental apparatus, it was intended that the plasma in the drift region be generated by a Penning discharge. As will be seen later in the discussion of the results, the beam itself generates a plasma which is of nearly sufficient density for beam-plasma interaction at the modulation frequency used here. The Penning discharge configuration is thus used to augment the density of the plasma generated by the beam. The Penning discharge consists of a cylindrically shaped anode and two planar cathodes which are positioned as "ends" of the anode cylinder. An axial magnetic field prevents the "fast" cathode electrons from a direct transit to the anode thus enhancing their ability to make ionizing collisions and maintain a discharge at low pressures. At low pressures (10^{-4} to 10^{-5} torr) Knauer (14) has shown that the central region of the discharge contains a neutral plasma whose potential is approximately cathode potential, and whose density is proportional to anode current. The simplicity of the Penning discharge configuration and the

depression of the plasma potential toward the cathode potential were prime factors in its selection. Noise and undesirable anomalous diffusion mechanisms known to be present in the discharge have not been observed at low magnetic fields (below 400 gauss), hence these troublesome properties are avoided. The configuration of the Penning discharge used here has a cylindrical anode 5 cm in diameter and 5 cm in length with the distance between cathodes being 5.84 cm. The cathodes of the Penning discharge are operated at ground potential, one cathode being used as the collector for the electron beam. Thus the cathode of the electron beam is operated at high negative potential, the anode of the Penning discharge at high positive potential.

The instantaneous current probe is simply a molybdenum wire extending from a rigid 50 ohm coaxial transmission line. The transmission line is bent so that the probe swings in an arc across the electron beam when the line is rotated as seen in photograph (c) of Figure 3.2. Vacuum seals are accomplished with o-rings and a hermetic BNC type connector so that the probe may be positioned externally. Reflections resulting from the hermetic BNC connector were measured with a time domain reflectometer and found to be of the order of ten percent. The sampling oscilloscope used for the probe measurement has an optimum rise time of 60 to 70 psec (measurement of the output of a step function generator known to have a 100 psec rise time verified that the scope rise time is at least less than 100 psec). This is approximately one-tenth the modulation period and, consequently, the probe measurement should be capable of displaying

essentially all the details of the beam current behavior of interest in this investigation. The probe is located as near to the plane of the beam collector as possible.

The velocity analyzer is patterned after those used by Cutler (15) and Gewartowski (16) in studies of traveling wave devices. The small hole (0.127 mm in diameter) in the collector allows a fraction of the beam current to enter the velocity analyzer. This "sample" of the beam is first focused by an einzel lens, then passes through the velocity sensitive deflection system, then passes through a time dependent deflection system and drifts to impinge on a phosphored screen. The velocity sensitive deflection system consists of a pair of magnetic pole pieces which deflect the beam vertically and a set of electric deflection plates which also deflect it vertically, but in the opposite direction. The electric and magnetic fields are adjusted so that electrons of the average or unmodulated beam velocity pass through the system without being deflected. If the electric deflecting field E_y and the magnetic deflecting field B_x are assumed to be uniform and to act over the same drift length s , the condition for balance is that the deflection y_d vanish, or

$$y_d = - \frac{e \ell s}{m u_o} [u_o B_x + E_y] = 0 \quad (3.2)$$

where ℓ is the distance from the deflection system to the phosphored screen, and e , m , and u are respectively the charge, mass, and velocity of the electrons being deflected. Thus for balance,

$$E_{y_o} = - u_o B_{x_o} \quad (3.3)$$

and for $u = u_0 + \Delta u$ with Δu small,

$$\Delta y_d = \frac{els}{\mu_0^2} E y_0 \frac{\Delta u}{u_0} \quad (3.4)$$

Thus the vertical deflection is seen to be linearly proportional to the fractional change in velocity. The time sweep is accomplished with two sets of deflection plates, one providing horizontal deflection and the other vertical deflection. The voltage applied to these plates is a sinusoidal voltage at one-fourth the beam modulation frequency, or 275 mc. The signal applied to the horizontal plates is ninety degrees out of phase with and equal in amplitude to the vertical signal resulting in a circular sweep of the unmodulated beam. Thus the deflections x_d and y_d are given by

$$y_d = A \sin \omega t$$

$$x_d = A \cos \omega t$$

which when written in polar form give

$$r = A e^{i\omega t}$$

so that

$$\theta = \omega t$$

and therefore arc length on the circumference of the "sweep" circle is linearly proportional to time. Since the modulation frequency is four times the "sweep" frequency, four cycles of modulation are displayed around the circumference of the sweep circle as seen in

Figure 3.4a of part C of this chapter. The circular trace of the unmodulated beam is superimposed as a base line on which the time base may be marked off. The vertical displacement of the modulated beam trace from this base line is the desired measure of velocity. The sweep deflection plates are also used to position the beam, both vertically and horizontally by application of d.c. voltages which are isolated from the r.f. by an LC coupling circuit.

The phosphored screen forms part of the vacuum envelope and is simply the face of an oscilloscope cathode ray tube which has been cut off with a portion of the glass envelope. The glass envelope was ground flat and smooth at the cut so that a vacuum seal could be obtained with an o-ring and a specially designed flange. The original phosphor was replaced by a high intensity, standard green phosphor signified as P31. A carbon ring was coated on the inside of the envelope section for post deflection acceleration.

A block diagram showing the connection of the r.f. components is shown in Figure 3.3. Synchronization and simultaneous tuning of the modulation and "sweep" signals is accomplished by generating r.f. power at the "sweep" frequency of 275 mc and then multiplying this signal by a factor of four to obtain the 1100 mc signal for the velocity modulator. The power oscillator delivers ten watts, of which approximately five watts are fed into the sweep circuits and five watts into the multiplier. The sweep circuits consist of resonant tuned stubs and line stretchers which are adjusted to obtain the proper amplitude and phase relationship between the "sweep" deflection plates to give a circular sweep. The frequency multiplier has an

output of approximately 1.25 watts for five watts input and this amplitude is then controlled by a continuously variable attenuator. The phase shifter in the 1100 mc line is merely for convenience in adjusting the reference between the modulation phase and the phase of the velocity analyzer sweep so that a waveform like that of Figure 3.4a is obtained. The oscillator is tuned to cavity resonance by minimizing the reflected power. Incident and reflected power are measured at the point of coupling into the velocity modulation cavity with 20 dB directional couplers, bolometer sensing elements and power bridges. A coaxial switch allows the cavity input to be easily diverted both for zeroing of these power bridges and for providing unmodulated beam reference traces. The sampling oscilloscope is synchronized to the 275 mc signal since the amplitude available is larger, and synchronization to the lower frequency is less difficult. The phase relationship of the oscilloscope display is adjustable by a delay control incorporated in the oscilloscope, consequently absolute synchronization of phase is not possible.

The entire assembly of the apparatus is seen in photograph (d) of Figure 3.2. The instrument racks and the apparatus are positioned so that both the velocity analyzer screen and the oscilloscope screen can be seen by the experimenter while making adjustments. Consequently the effect of varying a given parameter is quickly and easily observable.

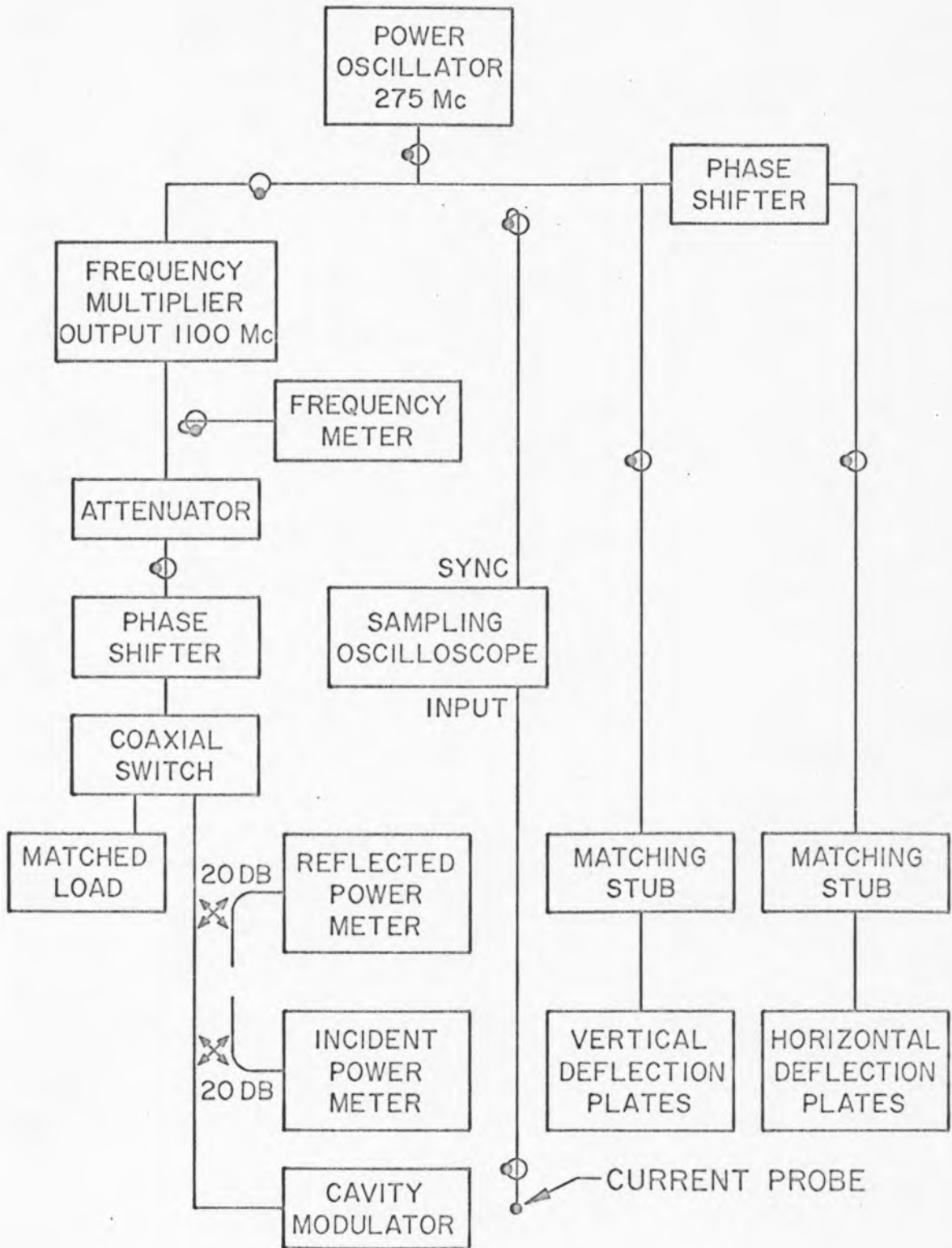


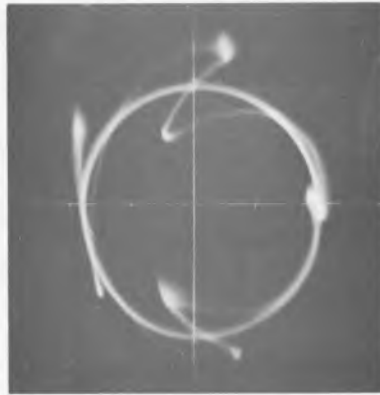
Figure 3.3 Block Diagram of Experiment Electronics

C. Method of Collecting and Analyzing Data

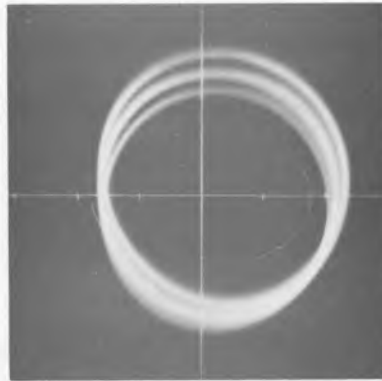
Collection of experimental data consisted of taking a set of polaroid photographs, like those shown in Figure 3.4, for each set of experimental parameters. Figure 3.4a shows the velocity analyzer pattern with the circular unmodulated beam pattern (base line) superimposed. Whenever the modulated pattern displays any fine detail in the vicinity of the base line, this base line is omitted for clarity. Figure 3.4b shows a set of calibration traces for 3.4a obtained by changing the beam velocity by $\pm 2.5\%$ (a change of ± 50 volts electron gun voltage). Figure 3.4c shows the sampling oscilloscope waveform of the current collected by the probe with the unmodulated current level superimposed. The step by step procedure followed in obtaining such a set of photographs was as follows:

1. Record all parameters
2. Switch modulation signal to matched load
3. Zero power bridges
4. Switch modulation signal to modulating cavity
5. Tune oscillator and adjust power input
6. Photograph velocity analyzer and sampling oscilloscope waveforms
7. Switch modulation signal to matched load
8. Superimpose unmodulated beam signal on photographs of 6 *
9. Measure d.c. probe current with ammeter and record
10. Superimpose unmodulated velocity analyzer patterns with electron gun voltages of 950, 1000 and 1050
11. Check all parameter values.

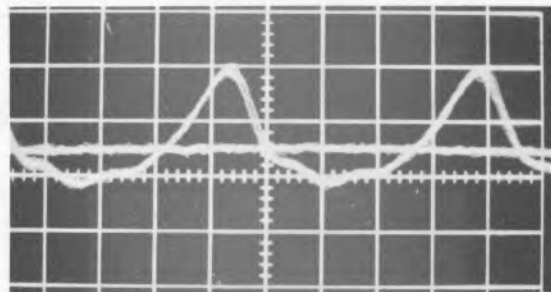
*Base line is not superimposed on all velocity analyzer photographs.



(a) VELOCITY ANALYZER WAVEFORM



(b) CALIBRATION FOR THE VELOCITY ANALYZER



(c) SAMPLING OSCILLOSCOPE TRACE
OF CURRENT WAVEFORM
10m V/div , 0.2 nsec/div

Figure 3.4 Representative Data

The photographs shown in Figure 3.4a,b represent the form in which the velocity analyzer data appears and is photographed. However, the photographs shown here are for illustration and are somewhat overexposed for useful data reduction. The data is reduced from these photographs by placing a strong light behind the photograph and carefully tracing the desired portion of the waveform and the grid axes with a finely pointed drawing pencil. The velocity analyzer patterns of Figure 3.4a and b are traced in superposition, using the grid axes for alignment. Reduction then consists of dividing the base line for one modulation cycle (the one centered at the top of the pattern) into a minimum of ten time intervals with drawing instruments, and constructing vertical deflection lines at these intervals. The velocity deviation can then be measured in terms of the calibration deflection at each time interval and tabulated. Since the arrival time or relative phase of the electrons shown on the screen is the phase at the plane of the sweep deflection plates, it must be corrected in terms of their velocity and the drift distance ℓ_1 between the entrance to the velocity analyzer and the sweep deflection plates. The arrival time t at the sweep deflection plates is related to the correct arrival time t_{corr} by

$$t = t_{\text{corr}} + \frac{\ell_1}{V}$$

where V is the electron velocity and $V = u_0 + \Delta u$, thus

$$\omega t = \omega t_{\text{corr}} + \frac{\omega \ell_1}{u_0 \left(1 + \frac{\Delta u}{u_0}\right)}$$

In terms of normalized variables

$$T_{\text{corr}} = T - \frac{L_1}{1 + \frac{\Delta u}{u_0}} \quad (3.5)$$

and for small $\frac{\Delta u}{u_0} = \Delta V$ this becomes

$$T_{\text{corr}} = T = L_1(1 - \Delta V) = T - L_1 + L_1\Delta V \quad (3.6)$$

Since the L_1 is simply a shift of reference, not dependent on velocity, the correction to T , ΔT , is given by

$$\Delta T = L_1\Delta V \quad (3.7)$$

Thus from the tabulated values of T and ΔV obtained from the data photographs, the values of T_{corr} and V are obtained for comparison with theory. For comparison with the computed current waveform, the experimental current waveform of Figure 3.4c is normalized to the average or d.c. current value. For this purpose the base line or zero current deflection is located on the current photograph using the average current trace, the measured probe current, and the deflection sensitivity. Thus the ratio of the instantaneous to average current deflection is obtained from the photograph for a sufficient number of points to reconstruct the normalized waveform.

While many parameters were varied to determine their effect on the data, the principle parameters of interest are beam current, initial velocity modulation and plasma density. The beam current was measured with a milliammeter in the cathode circuit of the electron gun. The initial velocity modulation is proportional to the power

input to the cavity and was measured using a 20 dB directional coupler, a bolometer sensing element and a power bridge. The plasma density is for the most part an unknown in the experiment. No independent method of measuring the plasma density was provided for in the design of the experiment, since the standard techniques are either too inaccurate to be of any use, or too difficult to incorporate without perturbing the experimental configuration. Since the Penning discharge plasma density is known to be proportional to discharge current, this was intended to be the measure of plasma density. The beam generated plasma makes this means of monitoring plasma density unreliable, however, since plasma density is a function of background pressure, and beam current, in addition to Penning discharge current.

D. Characteristics of the Experiment

While not directly pertinent to the beam-plasma investigation, several calibrations and other properties of the experimental apparatus are worth mentioning. A direct calibration of the velocity analyzer is used in collecting the data by photographing the deflection change due to a change in the electron gun voltage for each data point. This calibration procedure accounts directly for the decrease in deflection due to the use of post deflection acceleration and for astigmatism effects. Derivation of equation 3.4 assumes that the electric and magnetic deflecting fields are uniform and act over the same volume. In the first velocity analyzer constructed, the magnetic field was found to act over a much larger volume than the

electric field, and balance could not be achieved for very large magnetic fields. This was remedied by using mu metal shielding and confining the magnetic deflection field to the same region as the electric deflection region. In terms of the beam voltage V_o , and deflection voltage at the balance condition V_{do} , equation 3.4 becomes

$$\Delta y_d = \frac{V_{do}}{2V_o} \frac{\ell s}{d} \cdot \frac{\Delta u}{u_o} \quad (3.8)$$

where d is the spacing between the deflection plates. For the experimental apparatus the approximate dimensions are $\ell = 34$ cm, $s = 0.8$ cm and $d = 0.35$ cm. With $V_{do} = 400V$, $V_o = 1000V$ and $\Delta u/u_o = 0.05$, equation 3.8 gives

$$\Delta y_d = 0.78 \text{ cm}$$

The average of several experimentally observed deflections is

$$\Delta y_d = 0.72 \text{ cm}$$

which was considered sufficiently close agreement.

The most critical calibration relates the modulating cavity power input to the velocity modulation of the electron beam. The maximum fractional change in velocity $\Delta u/u_o$ is given by

$$\Delta u/u_o = \sqrt{1 + \alpha \frac{V_1}{V_o}} - 1 \quad (3.9)$$

where α is the gap factor, V_1 is the maximum gap voltage, and V_o is the electron beam acceleration voltage. For small V_1/V_o

$$\Delta u/u_o \approx \frac{\alpha}{2} \frac{V_1}{V_o} \quad (3.10)$$

The cavity gap voltage can be related to the cavity power input by the cavity Q by

$$Q = \frac{W}{P_{ave}} \quad (3.11)$$

where W is the stored energy and P_{ave} is the average power input to the cavity. Writing W in terms of a volume integral

$$W = \int_{\text{volume}} \epsilon_o \frac{E^2}{2} dV \quad (3.12)$$

For the re-entrant cavity the electric field is concentrated in the gap region, a cylinder of radius ρ , and height δ so that for the cavity in question,

$$W \approx \frac{\epsilon_o}{2} E_{max}^2 \pi \rho^2 \delta \quad (3.13)$$

and with $E_{max} = V_1 \delta$

$$W = \epsilon_o \frac{V_1^2 \pi \rho^2}{2\delta} \quad (3.14)$$

Thus

$$\dot{Q} = \frac{\omega \epsilon_o V_1^2 \pi \rho^2}{2\delta P_{ave}} \quad (3.15)$$

or

$$V_1 = \frac{2\delta Q P_{ave}}{\omega \pi \epsilon_o \rho^2} \quad (3.16)$$

and

$$V_0 \approx \frac{1}{2} \frac{\alpha}{V_o} \sqrt{\frac{2\delta Q P_{ave}}{\omega \pi \epsilon_o \rho^2}} \quad (3.17)$$

With $\alpha = 0.942$, $V_o = 1000$, $\delta = 0.3$ cm, $\rho_{\perp} = 1.91$ cm, $Q = Q_L = 1235$ (the measured value from B) and $\omega = 6.92 \times 10^9$, VO becomes

$$VO \approx 0.157 \sqrt{P_{ave}} \quad (3.18)$$

where P_{ave} is in watts. This relation was also determined experimentally by using a very low density beam, and determining the power input necessary to give the same deflection as the calibration deflections, $VO = 0.025$. Approximately 25 mW of input power is required to produce this deflection yielding the experimental relation

$$VO = 0.158 \sqrt{P_{ave}} .$$

Since this value is in good agreement with the calculated value, it was used for all data reduction.

The sampling oscilloscope deflection due to the average beam current to the probe was compared with the measured probe current as follows. Operating the electron beam without velocity modulation, the current collected by the current probe was measured using a milliammeter, and then by observing the sampling oscilloscope deflection due to the current probe input with the beam voltage on and off. The change in deflection was found to agree well with the voltage developed across the 50 ohm termination by the measured current. It was later discovered that when the beam is velocity modulated and bunching occurs, the probe signal is proportional to displacement current which flows in the probe circuit as well as collected current. Because of this, the probe signal displays a negative as well as a

positive peak. Roughly speaking, the positive peak is proportional to the total amount of charge in the bunch of electrons which passes the probe position, while the negative peak is proportional to the charge which is not collected but passes by the probe. Since the probe collects only a small portion of the beam, this displacement current may become large when the current is highly bunched, making the amplitude of the probe signal rather unreliable for determining the instantaneous current amplitude. Figure 3.4c shows only a slight negative overshoot in the current waveform, since the current density and the bunching of the current are not very large (1 ma beam). In the next chapter, however, many experimentally obtained waveforms are seen to have large negative peaks, qualitatively indicating a high degree of bunching, and limiting the quantitative interpretation of the waveform. Since the capacitive coupling between the charge of the bunched electrons and the probe is highly sensitive to their geometric relationship, which cannot be accurately determined, it does not seem feasible to attempt calculating a correction for this effect.

One property of the experimental apparatus which is worthy of special mention is the "synchronous detection" nature of the instrumentation. Since both the velocity-analyzer and the sampling oscilloscope are synchronized to the power oscillator, and all circuits are rather narrow band and tuned to the operating frequencies of either 275 or 1100 MC, unwanted signals are not detected and the experimental data is relatively noise free. While the power oscillator has a tendency to drift in frequency, the synchronization is

such that only the oscillator tuning need be frequently checked and adjusted. This is accomplished simply by using the frequency counter, seen in Figure 4d, as a continuous monitor of oscillator frequency.

Perhaps the most difficult feature of the experimental technique is the adjustment of the focus, sweep and balance voltages in the velocity analyzer. If the phase of the sweep voltages is not proper, the time scale along the circumference of the "base line" trace will not be linear, even though the trace appears circular. Focussing of the beam was found to depend on the magnitude of the beam current, the magnetic field, and the pressure and plasma density in the beam-plasma interaction region. It was not always possible to focus the beam satisfactorily with the lens alone, and the magnetic field or the beam current had to be adjusted slightly also. Since a change of nearly any parameter changed the beam properties, intensity of the pattern on the phosphor screen also varied with changes in parameters, and determining the correct exposure for photographing the trace was frequently both difficult and tedious. When the degree of bunching is high, part of the trace is very dim, while the part due to the bunch is very bright. Hence it is exceedingly difficult to find an exposure which does not over-expose the bright area, yet preserves the dim segments needed to establish the time scale (intersections with the base line at 0 and 2π). This difficulty in successfully photographing the velocity analyzer pattern under the nonlinear, bunched beam conditions is perhaps the most severe limitation of the quantitative capability of this technique.

The operation of an electron gun in proximity to a plasma region is probably the most serious problem in a practical beam-plasma amplifier, and this difficulty was experienced in this investigation. While the barium impregnated cathode withstood ion bombardment reasonably well for short periods of time, the total lifetime of the cathode was considerably shortened. In addition, the cathode was observed to change its emission characteristics due to the introduction of the plasma in an unpredictable way. At times, increasing the plasma density (either by increasing background pressure or Penning discharge current) increased the emission; other times it decreased emission. Under some operating conditions (usually irrepeatable) cathode current was observed to slowly increase to a value far in excess of the rated perveance, accompanied by high gain when the beam was modulated, and oscillations in some cases when the beam was unmodulated. If the apparatus was allowed to operate in this mode for any length of time (minutes) the emission ceased and the cathode could be re-activated only with considerable difficulty. This behavior is attributed to a build up of ions which bombard the cathode, heating it to emission temperature in an "auto-cathode" effect. It was found that this phenomena rarely occurred when the cathode was operated in a temperature limited emission regime. No attempt was made to discover the details, or to explain more fully the mechanism of this phenomenon due to its injurious effect on the cathode.

The experimental apparatus represents a compromise in a number of vacuum and microwave techniques, having requirements which

come into conflict. For the most part the apparatus was designed to be constructed with commercially available components. Consequently, the ultimate vacuum attainable was not optimum, and the reflections from the r.f. feed-throughs was not minimum.

IV. RESULTS

A. Theoretical Results

In order to understand the experimental observations, a complete understanding of the theoretically predicted behavior in terms of the measured quantities is helpful. The theoretically predicted behavior is described in terms of the normalized velocities V_i , and arrival times T_i of the discs representing the electron beam as a function of the normalized drift distance Z . The parameters varied are electron beam current I_0 , initial velocity modulation Δu , and plasma density, electron temperature, and collision frequency ω_p , T_e , and ν . The quantities observed experimentally are instantaneous current I , and electron velocity V_1 , and arrival time T at a drift distance Z of 22. The results are in the form of point plots of V_i versus T_i in the theoretical study and continuous plots of V versus T for the experimental study. An instantaneous current waveform is computed from the T_i for each case of the theoretical study for comparison with experiment. Since the T_i are ωt_i , T_i can be considered the relative phase, or phase of the discs or electrons. The computed V_i versus T_i plots or the experimental V versus T plots will therefore be called velocity-phase plots in the discussions which follow.

The first case considered is the simple klystron interaction with no plasma in Region II of Figure 2.1a. The velocity-phase diagrams of Figure 4.1a,b are typical of the theoretical results to be presented and show the discs belonging to one modulation cycle as

they progress through the drift region. The two sets of points shown in Figure 4.1a,b afford a comparison of results computed here (discs represented by dots) with Webber's (9) results (discs represented by triangles). The parameters given are those used in this investigation, rather than Webber's, with $\beta_e = \omega/u_o$, $Z = \beta_e z$, and $(\omega_{pb}/\omega)^2 = 1.77 I_o$ where ω_{pb} is the beam-plasma frequency and I_o is the beam current. This relation between ω_{pb} and I_o applies to all currents stated and numerical values for the ratio ω_{pb}/ω are given, together with current values, in Figure 4.5 for reference. The method of plotting used here is also different from Webber's and his computation gives the discs a slightly different set of initial phases. Apart from this phase difference, the two methods agree quite well and the differences seen in Figure 4.1 are probably due mainly to the re-plotting of Webber's results.

The two sequences of Figure 4.1a,b show the large signal behavior of an electron beam of fixed diameter for two values of beam current at several positions along the drift path. Here, large signal behavior implies that the initial velocity modulation imparts sufficient momentum to the discs to overcome the space charge forces which arise. In (a) beam space charge forces are insignificant and the behavior displayed is essentially ballistic motion of the discs, with the velocity of each disc being only slightly changed from its initial velocity by the relatively small space charge forces. Thus as the discs of a modulation cycle progress along the beam path, those having $V > 1$ advance in phase (T decreases) and those having $V < 1$ are retarded in phase (T increases). For the parameters of 4.1a, some of

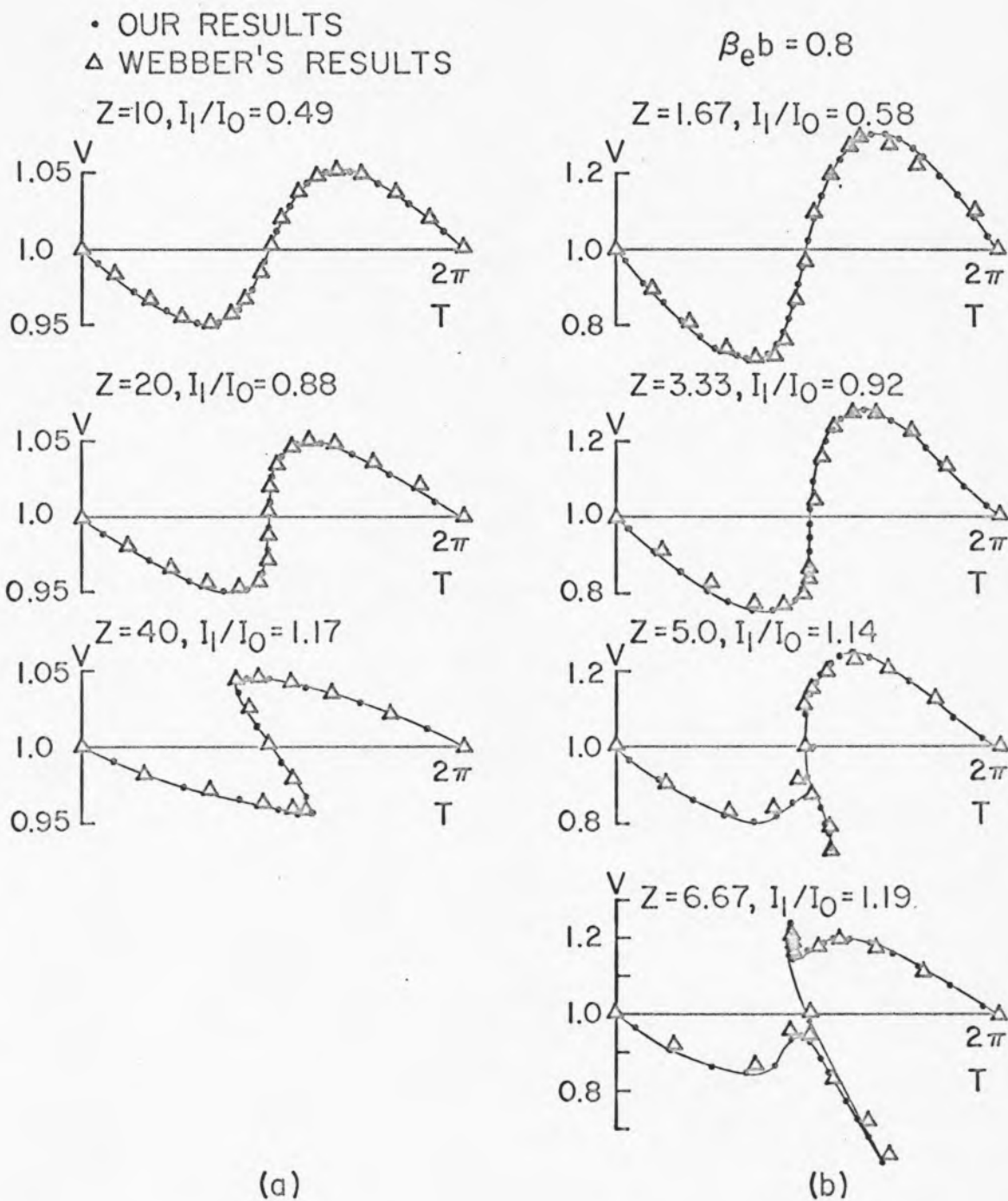


Figure 4.1 (a) Velocity-phase plots for $I_0 = 0.6$ ma, $V_0 = .05$
 (b) Velocity-phase plots for $I_0 = 0.7$ ma, $V_0 = 0.3$

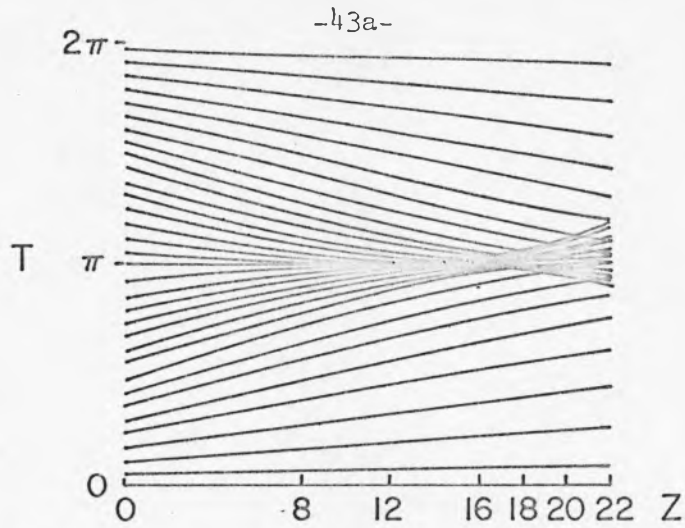
the discs have just overtaken others (in space) at $Z = 20$ and this is said to be the crossover point. This can also be thought of as a crossover in phase, since the relative phase between two discs which have "crossed over" is now reversed. As the cycle is followed to $Z = 40$, it is seen that more discs have "crossed over" with the velocity-phase plot maintaining its familiar "s" shape.

In 4.1b 32 discs have been used in the computation by Gould's method, whereas Webber's results were obtained with 16 discs. This illustrates, as was also noted by Webber, that there are no significant differences in the results obtained using a larger number of discs. The larger current in the beam of 4.1b effectively increases the charge on each disc and therefore the space charge effects in the beam are accordingly larger. Simple crossover as seen in 4.1a does not occur even though some of the discs have sufficient momentum to overcome the space charge forces. As the cycle being followed proceeds from $Z = 1.67$ to $Z = 3.33$ the particles tend to "bunch" in phase near $T = \pi$. This means that discs are also coming closer together in space, increasing the space charge density, and the corresponding repulsive space charge forces. This means that a fast disc which is advancing in phase with increasing Z experiences a retarding force as its phase approaches $T = \pi$ which decreases its velocity and inhibits crossover. Thus, up to the point of crossover, the faster discs whose phases approach $T = \pi$ tend to have their velocities decreased, and by similar reasoning, the slower discs whose phases approach $T = \pi$ tend to have their velocities increased as the cycle progresses along its path. Slightly past $Z = 3.33$ some of the

slower discs fall behind (in space) the bunch in spite of the strong space charge forces, and crossover occurs. Now the repulsive force of the bunch tends to decelerate this slower disc and its velocity is decreased as seen in the $Z = 5$ plot of 4.1b as the cycle progresses downstream. At a point further downstream faster discs overtake (in space) the bunch, and are thereby accelerated to higher velocities as seen in the $Z = 6.66$ plot of 4.1b.

The velocity-phase plots of Figure 4.1a,b thus illustrate the effect of beam space charge in large signal behavior for the extremes of space charge conditions. The observance of this large signal behavior depends on both the beam current density and the amplitude of the initial velocity modulation, since the "largeness" of the signal is measured in terms of the space charge forces built up in the bunching of the beam. The initial velocity modulation necessary to achieve this behavior in a given beam over a particular drift distance may far exceed the maximum allowable in linear theories. Webber has discussed these intermediate regions in detail for the klystron interaction so that only a few features need be considered here. Figures 4.2 and 4.3 show the behavior of beams having different current values but the same amplitude initial velocity modulation. Figure 4.2 shows the behavior of a 5 ma beam and the velocity-phase plots of 4.2b clearly indicate the same kind of behavior as 4.1b. Figure 4.2a is a plot of the disc phase, T_1 , as a function of drift distance Z . These "phase trajectories" can also be interpreted as the relative spacings or positions of the discs in one cycle as a function of drift distance Z . It can be clearly seen in 4.2a that a number of discs

(a)



(b)

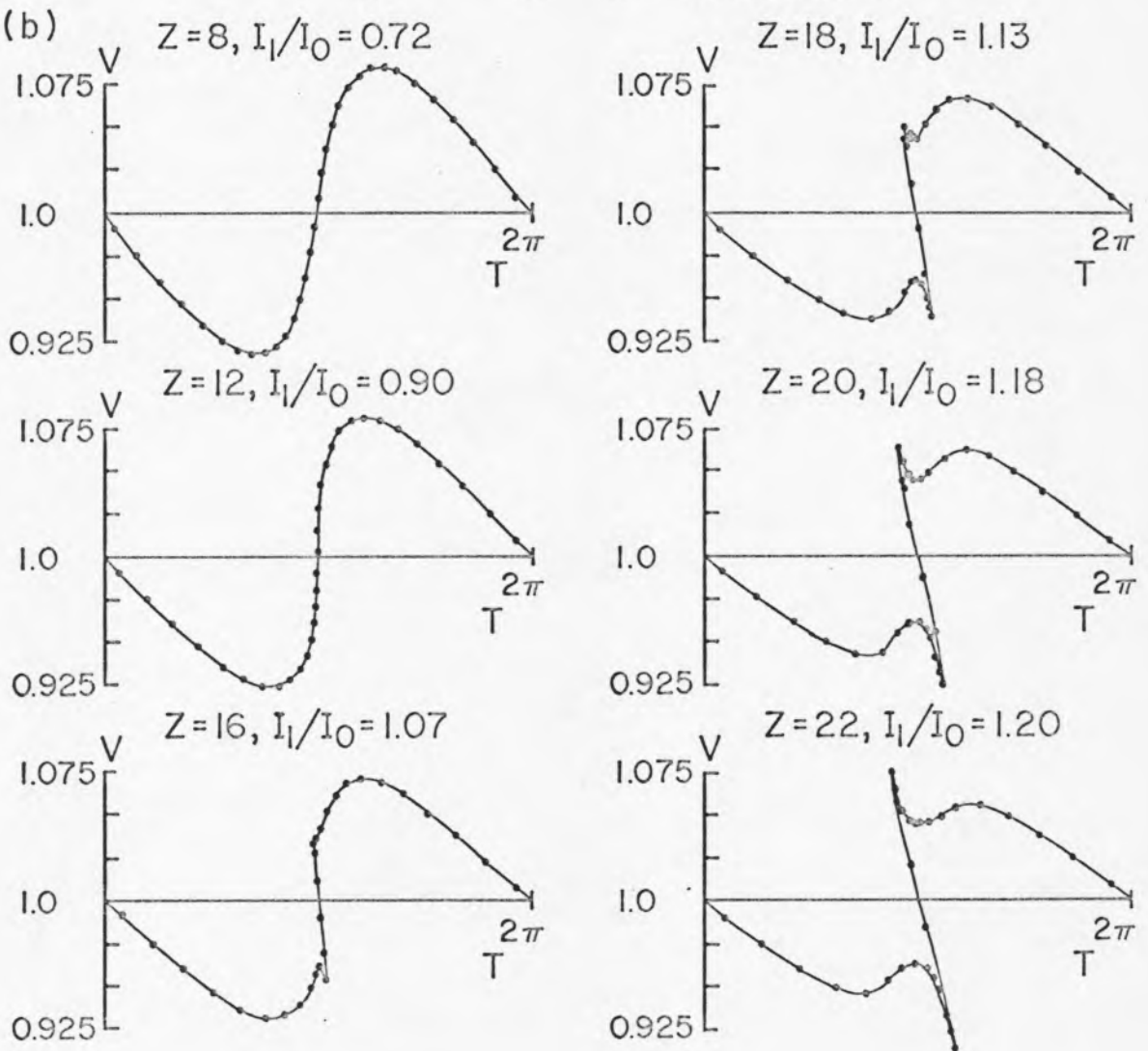
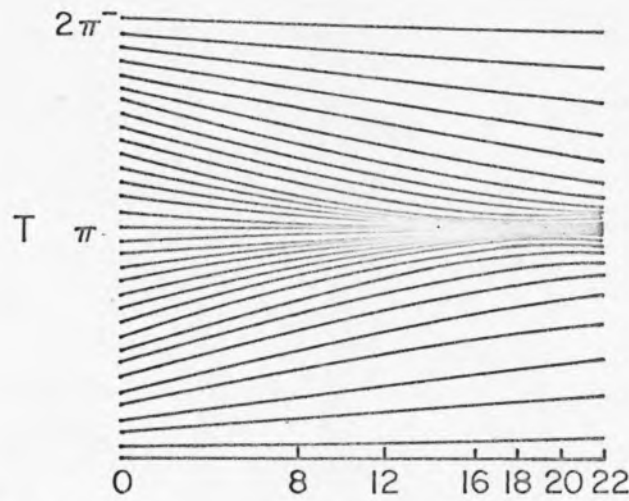


Figure 4.2 (a) Phase trajectories; and (b) velocity-phase plots computed for $I_0 = 5$ ma, $V_0 = .057$, $\beta_e b = 0.74$

(a)



(b)

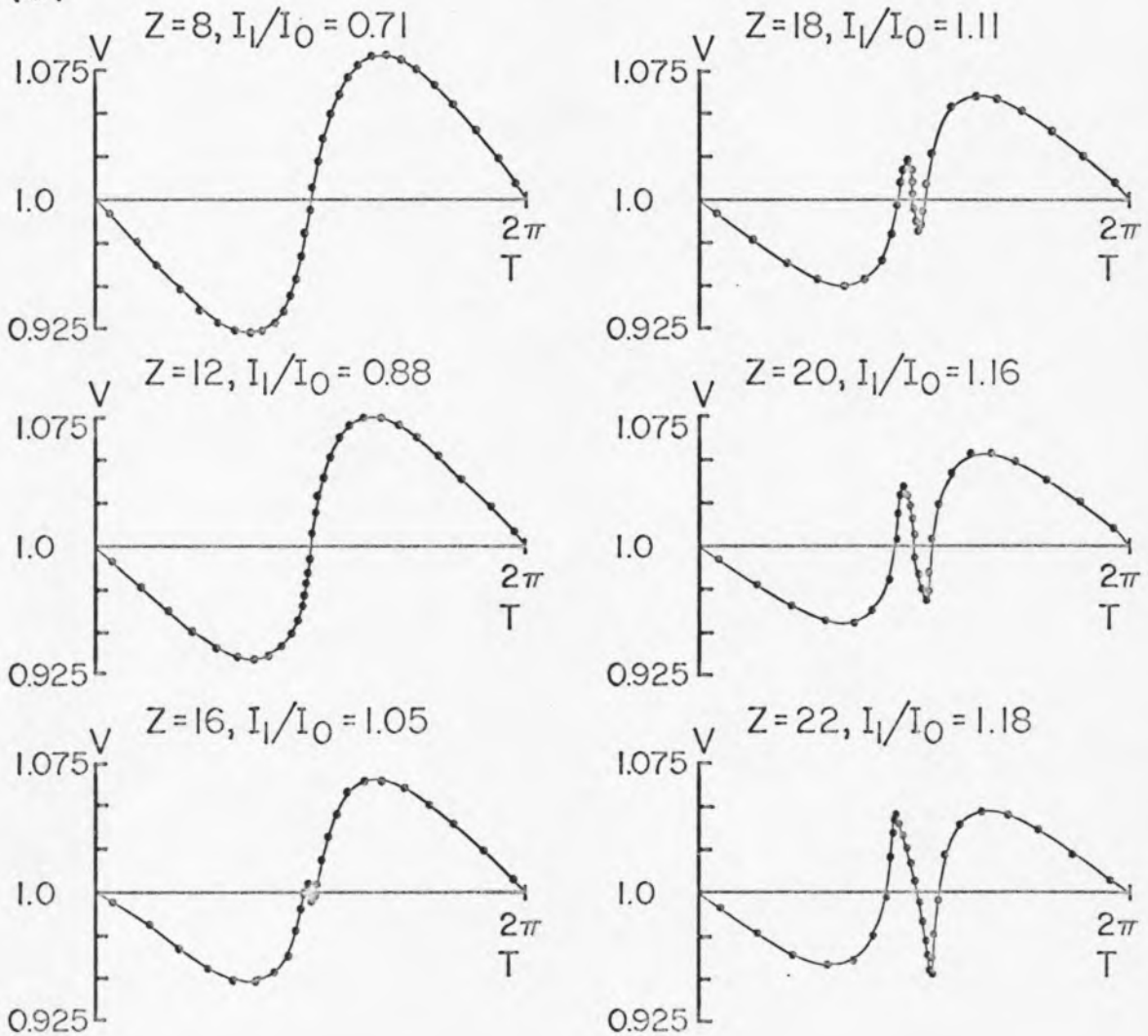


Figure 4.3 (a) Phase trajectories; and (b) velocity-phase plots computed for $I_0 = 10$ ma, $V_0 = 0.067$, $\beta_e b = 0.74$

cross over at approximately $Z = 15$. In Figure 4.3 the beam current is 10 ma and it can be clearly seen both from the phase trajectories and the velocity-phase plots that no crossover occurs. Instead, as the discs begin to bunch in phase (and space) at $T = \pi$, the slow and fast electrons which approach the bunch are so strongly repelled by the space charge forces there that they "rebound" with respect to the bunch. Thus discs which had velocities $V < 1$ before "colliding" with the bunch have velocities $V > 1$ after rebounding, and vice versa. This is clearly evident in 4.3a. For a slightly larger percentage of modulation, crossover occurs for this beam current also, as is seen in Figure 4.4.

The ratio I_1/I_0 which is given for each drift position is the normalized fundamental Fourier component of the current, computed from the velocity-phase information by the method described in Chapter IIB. It is a quantitative measure of the degree of bunching and has a theoretical maximum value of 2 for delta function bunching. Using a purely ballistic analysis (no space charge forces considered) Webster determined the maximum I_1/I_0 to be 1.16. In Webber's nonlinear klystron analysis (9) maximum values of I_1/I_0 range from 1.1 to 1.2 depending on beam radius ($\beta_e b$), initial velocity modulation, and beam current density. Thus it is seen that repulsive space charge forces can contribute to bunching the beam electrons more tightly than is possible if the beam electrons behave purely ballistically. In this study ratios of I_1/I_0 are observed in the range 1.2 to 1.3 with the klystron interaction (no plasma region) and as large as 1.7 for the beam-plasma interaction. These large maximum

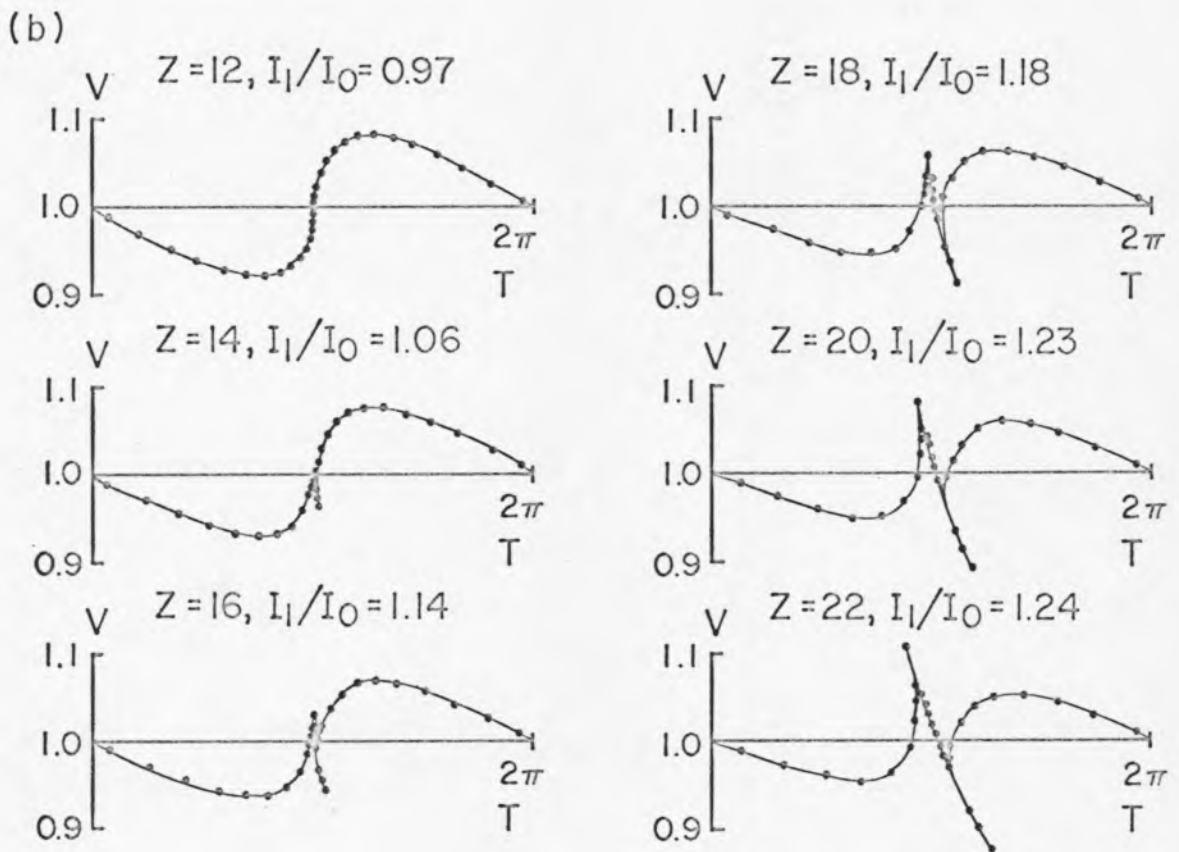
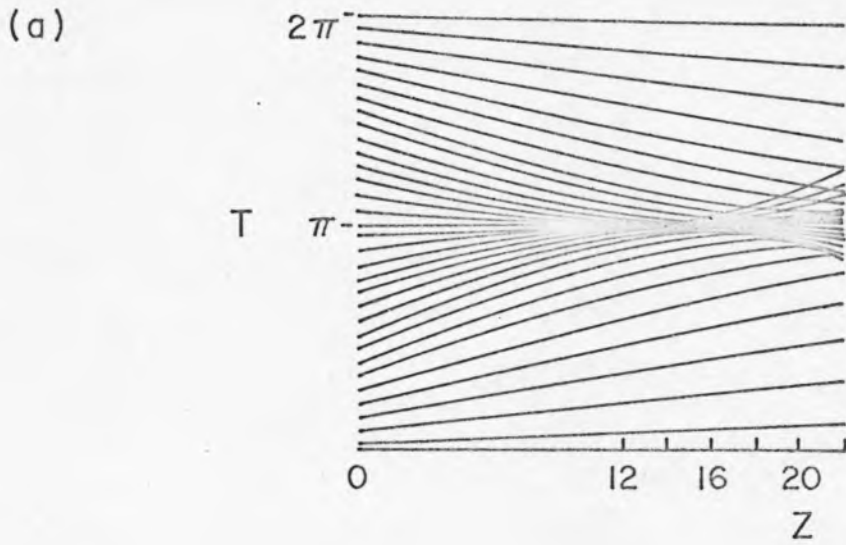


Figure 4.4 (a) Phase trajectories; and (b) velocity-phase plots computed for $I_0 = 10$ ma, and $V_0 = 0.1$ with $\beta_e b = 0.74$.

values occur only when there is large signal beam behavior (crossover occurs), and the maximum value occurs at a drift distance slightly past the crossover point.

Since it is not possible to make observations on the beam as a function of drift distance (Z) in the experimental apparatus, it is instructive to examine the predicted beam behavior in terms of the velocity phase plots at the observation position $Z = 22$. Figure 4.5 shows the effect of increasing beam current (beam space charge) with a fixed value of initial velocity modulation $V_0 = 0.05$. The parameter L/λ_g is the ratio of the drift length to the beam space charge wavelength. Figure 4.6 shows the effect of increasing the initial velocity modulation for a fixed value of beam current $I_0 = 10$ ma. In Figure 4.5 it is seen that for $I_0 = 0.5, 1,$ and 2 ma, beam space charge has little effect and the beam behavior is nearly ballistic. For the higher currents, the beam space charge forces are sufficient to prevent crossover, and for the 50 and 100 ma beams the behavior is essentially "small signal" with $L/\lambda_g > 0.25$ and the phase of the velocity modulation reversed. In Figure 4.6 the behavior displayed is similar to following the cycle along the drift path, although not exactly the same. As was seen in Figure 4.3, the beam behavior for values of $V_0 = 0.087$ in Figure 4.6 indicates beam space charge forces are sufficient to prevent crossover, while for $V_0 = 0.1$ the indication is that crossover has occurred as seen in Figures 4.2 and 4.4. It is seen that for $V_0 = 0.15$ the ratio of I_1/I_0 has decreased from the value for $V_0 = 0.1$ and in fact the maximum ratio

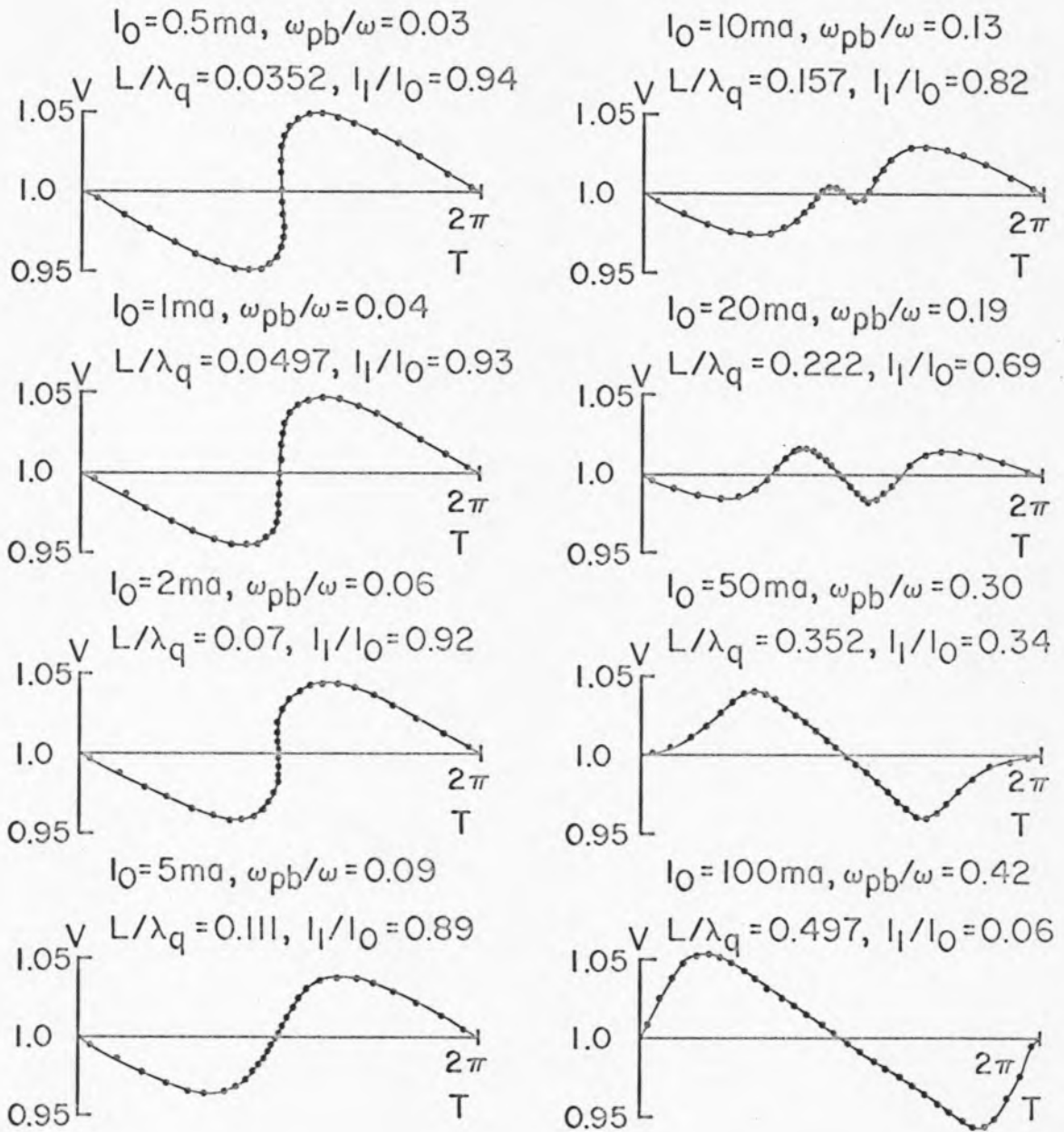


Figure 4.5 Velocity-phase plots computed for varying current values with $V_0 = 0.05$ at $Z = 22$

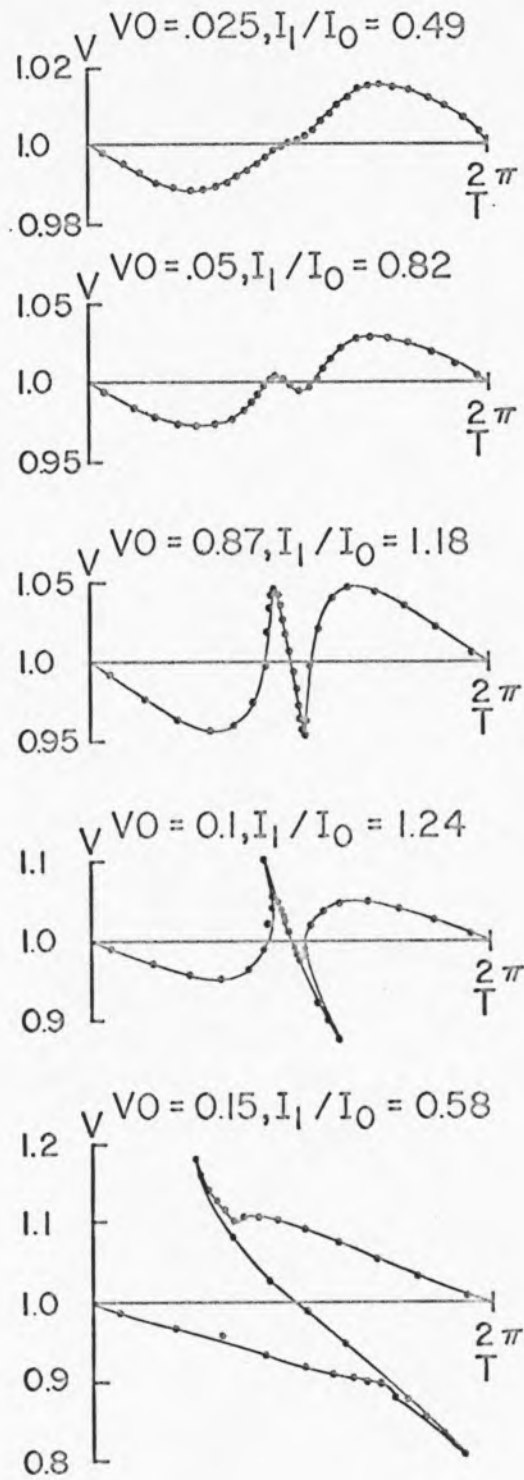


Figure 4.6 Velocity-phase plots computed for varying initial velocity modulation V_0 with $I_0 = 10$ ma at $Z = 22$.

of I_1/I_0 for $V_0 = 0.15$ is 1.19 and occurs for $Z = 13$. Consequently, observation at only one position as shown in Figures 4.5 and 4.6 requires careful evaluation, even when only one parameter is varied.

The preceding discussion has illustrated the beam behavior in terms of velocity-phase plots for various space charge and initial velocity modulation conditions. Now the effect of the plasma on the beam space charge forces will be discussed. As was mentioned earlier, the potentials of the plasma oscillations which are excited by the beam have the effect of changing the force between the beam electrons (discs) and thus the beam behavior is modified. The normalized acceleration force A_{nm} is the force on a disc n due to all discs characterized by the subscript m in the presence of a plasma and is a function of the disc separation ΔZ , shown in the disc model of Figure 4.7a. The dependence of A_{nm} on the ratio ω/ω_p and ΔZ is seen in Figure 4.7b for fixed values of plasma electron temperature T_e and collision frequency ν . For $\omega/\omega_p = 4$ in Figure 4.7b the force between discs is very little modified from the $\omega_p = 0$ condition. For $\Delta Z < \pi$ disc n is closer to disc m than to its counterpart in the next cycle, disc m' . Therefore, disc m experiences a negative force which tends to move it toward disc m' . When $\Delta Z > \pi$ the force is positive, tending to move disc n toward disc m . When $\Delta Z = \pi$ the force is zero and disc n tends to remain midway between disc m and disc m' in stable equilibrium. It can be easily seen that this is a repulsive force since the force increases as the position of disc n approaches that of disc m or m' , and the direction is such that disc n is forced

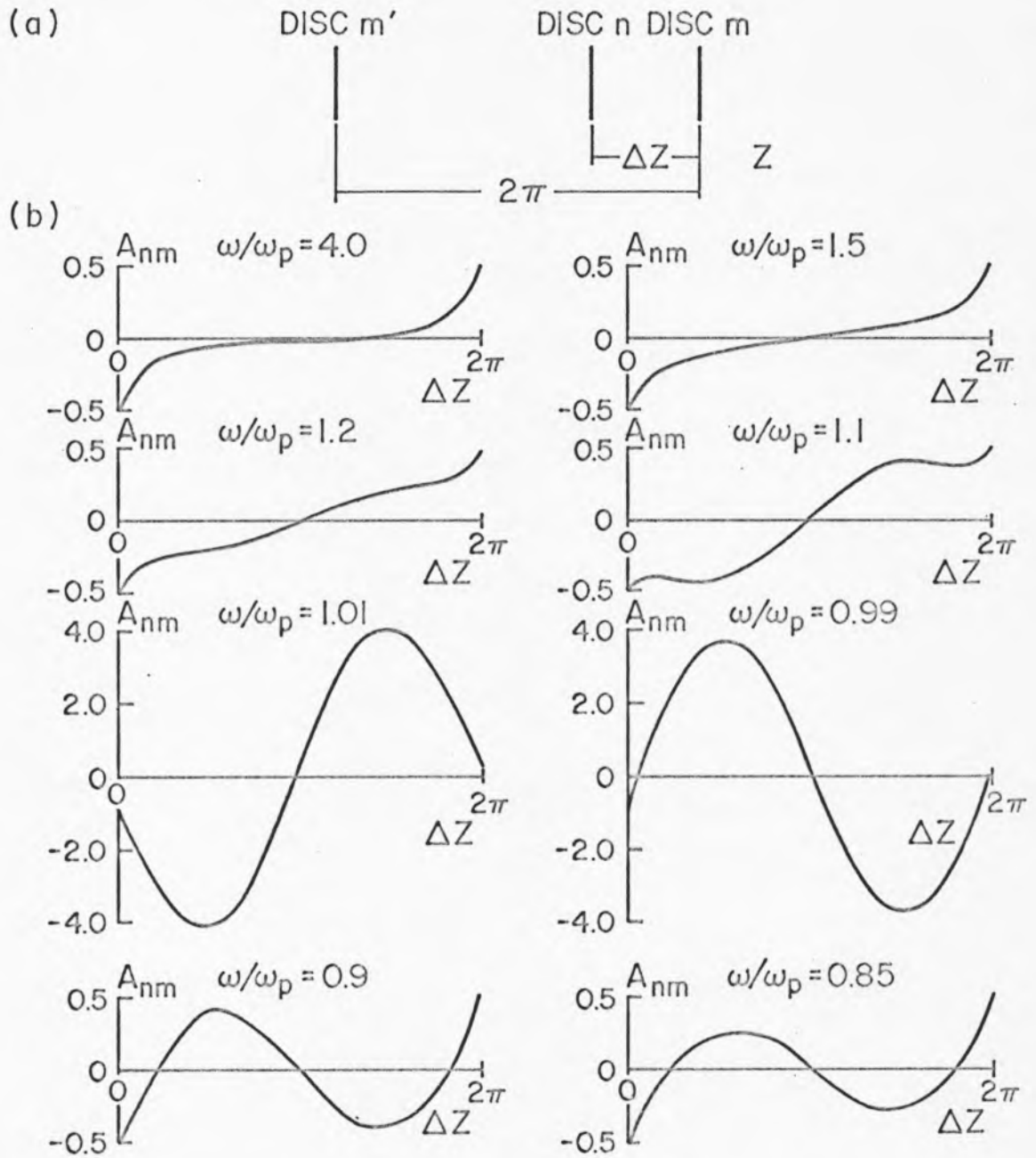


Figure 4.7 (a) Model for describing the normalized acceleration force A_{nm} ; and (b) the normalized acceleration force A_{nm} in the plasma region as a function of ΔZ for variation of the parameter ω/ω_p . $T_e = 0.23$, $v = 10$ mc

toward the midway position at which $\Delta Z = \pi$. As the ratio ω/ω_p decreases but is greater than unity, Figure 4.7b shows that the forces tending to keep disc n at the $\Delta Z = \pi$ position increase in a manner which effectively allows the charge on discs m and m' to act over a longer range (distance). Thus, for any given spacing, the repulsive force between discs increases with decreasing ω/ω_p to a maximum repulsive force at $\omega/\omega_p = 1 + \epsilon$ (plasma resonance). This has an effect similar to increasing the charge on the discs. At $\omega/\omega_p = 1$ a sharp change in the behavior of A_{nm} takes place. In the case for which $\omega/\omega_p = 0.99$ it is seen that when disc n is very close to disc m or m' , the normalized force A_{nm} is directed to cause the discs to move apart--a repulsive force. However, when the normalized spacing between the discs is of the order of $\pi/10$, the force vanishes and changes sign for any further increase in the spacing. Thus over most of the range of influence of disc m and its counterparts, disc n is attracted toward disc m or m' , tending to one of the equilibrium positions near m or m' where A_{nm} passes through zero. An equilibrium position still exists at $\Delta Z = \pi$, but this is now a position of unstable equilibrium since for a slight displacement, disc n is attracted toward disc m or m' . As ω/ω_p decreases still further, it is seen that the attractive force decreases, and the equilibrium spacing becomes larger. Hence for ω/ω_p greater than unity, increasing the plasma density (decreasing ω/ω_p) has the effect of inhibiting the bunching of discs or electrons due to the increase in range over which the repulsive force acts. The maximum effect occurs at

resonance ($\omega = \omega_p$) with the effective force changing abruptly to a force of attraction when ω_p becomes greater than ω (to within a small value of ΔZ) and bunching of discs or electrons is thereby enhanced. Further increase of ω_p reduces the range of the effective attractive force and enhancement of the bunching is correspondingly reduced.

The plasma parameters, plasma electron temperature, and collision frequency affect the behavior of the acceleration force $A_{nm}(\Delta Z)$ most severely for $\omega/\omega_p \approx 1$. While this is not readily apparent from the integral expressions for $A(Z)$ in Appendix B, it is easily seen by comparing the behavior of A_{nm} shown in Figures 4.8, 4.9 and 4.10 computed for $\omega/\omega_p = 0.99$, with that shown in Figure 4.11, computed for $\omega/\omega_p = 0.90$. Figure 4.8 shows the effect of changing the collision frequency with $\omega/\omega_p = 0.99$, and zero electron temperature. The effect of collisions changes the spatial or phase dependence of the acceleration force as well as the amplitude. It is seen that this effect becomes noticeable when v/ω_p is of the same order as $\Delta\omega/\omega_p = (1 - \omega/\omega_p)$. The asymmetry observed is caused by the damping of the plasma oscillations excited by the set of discs ahead of disc n corresponding to the index m . This means that in summing the potentials of these plasma oscillations, the amplitudes corresponding to the more distant m discs may be severely attenuated, thus modifying their contribution for any given ΔZ (ΔZ may be interpreted as a spacing measured in units of u_0/ω or a difference in crossing time at some reference plane measured in terms of $\omega \cdot \Delta t$) and resulting in an effective phase shift. The

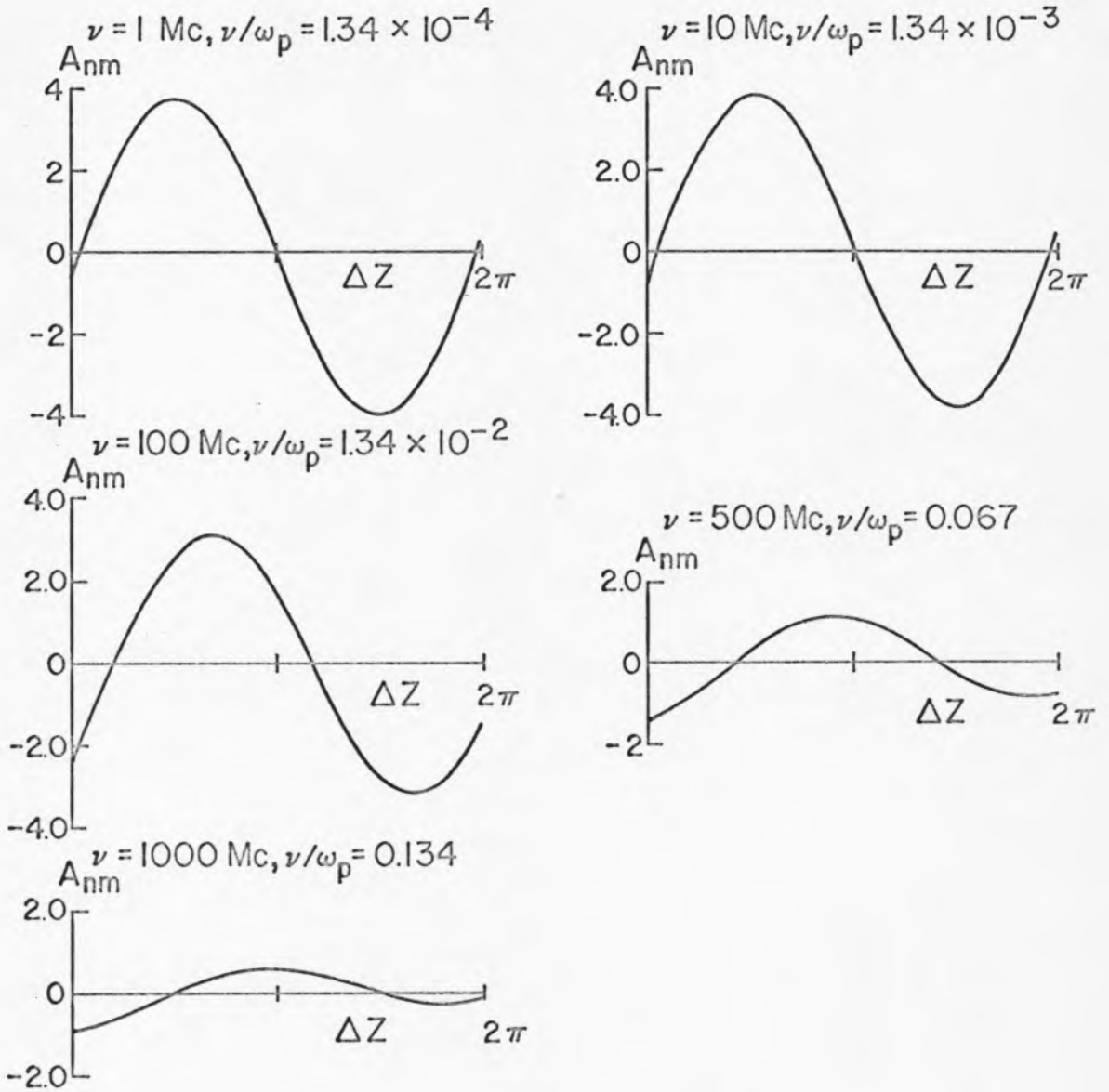


Figure 4.8 The normalized acceleration force A_{nm} as a function of ΔZ computed for $\omega/\omega_p = 0.99$, $T_e = 0'$, and varying collision frequency ν .

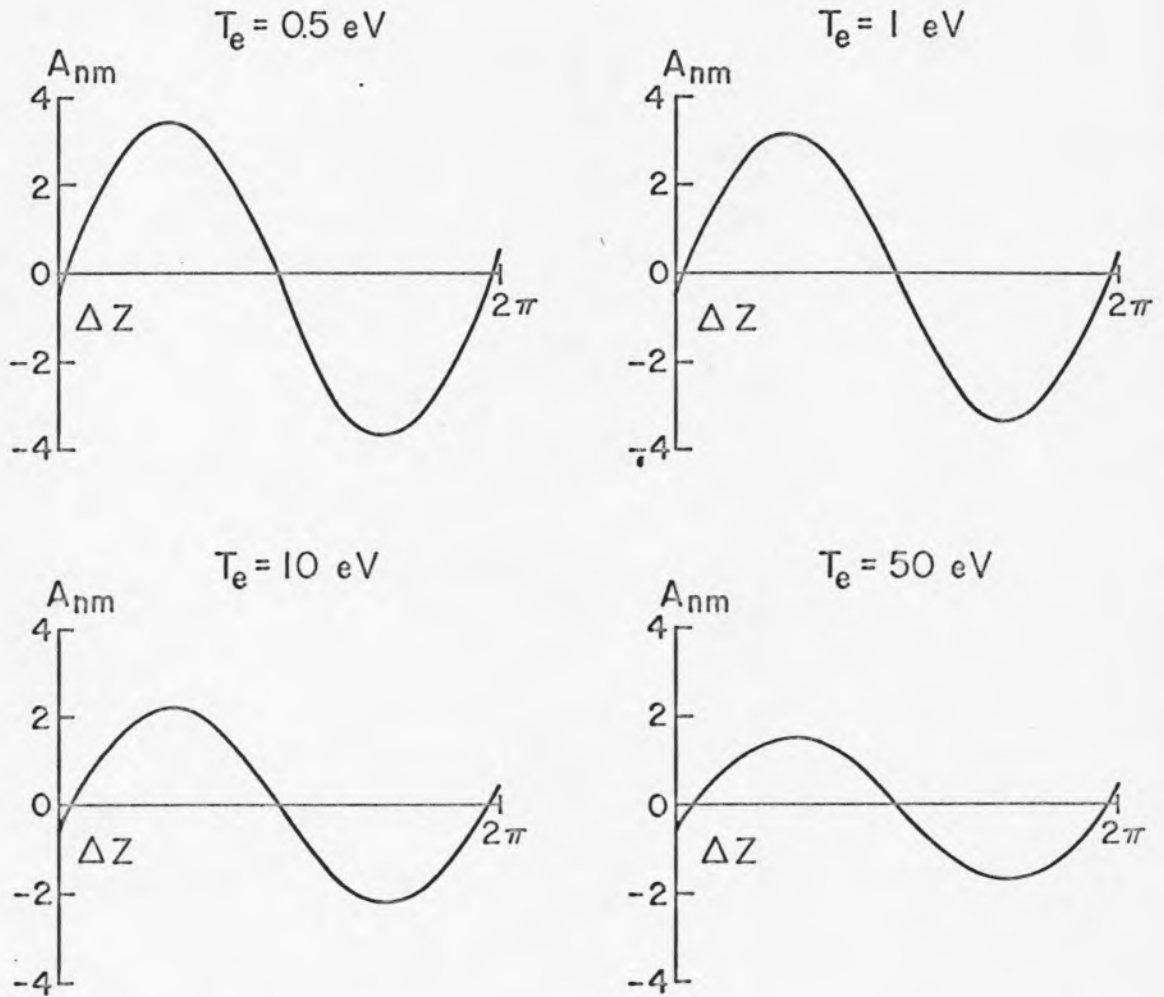


Figure 4.9 The normalized acceleration force A_{nm} as a function of ΔZ computed for $\omega/\omega_p = 0.99$, $v = 0$, and varying electron temperature T_e . The kinetic energy of the beam electrons is 1 KeV

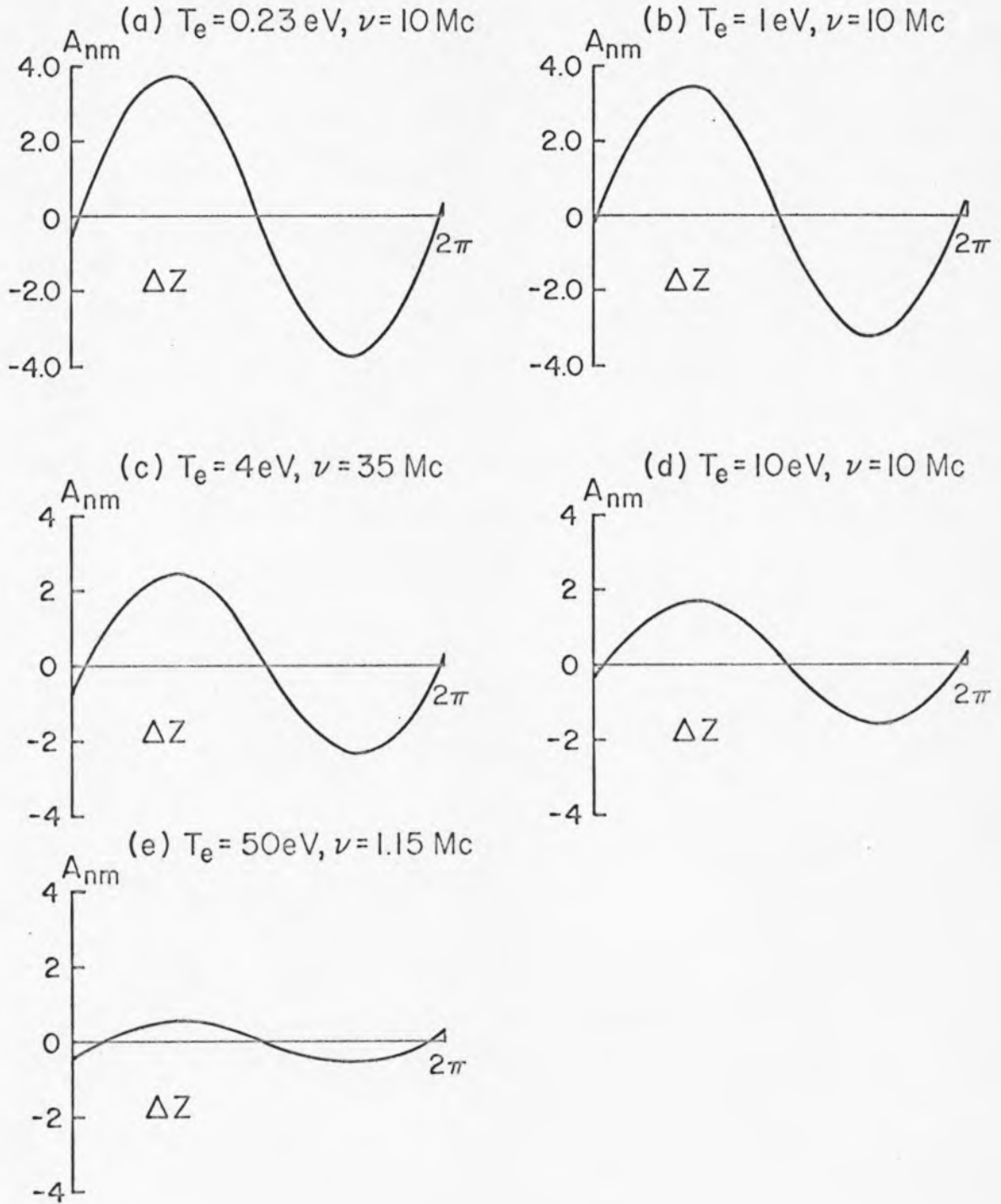


Figure 4.10 The normalized acceleration force A_{nm} as a function of ΔZ computed for $\omega/\omega_p = 0.99$ and several sets of typical plasma conditions.

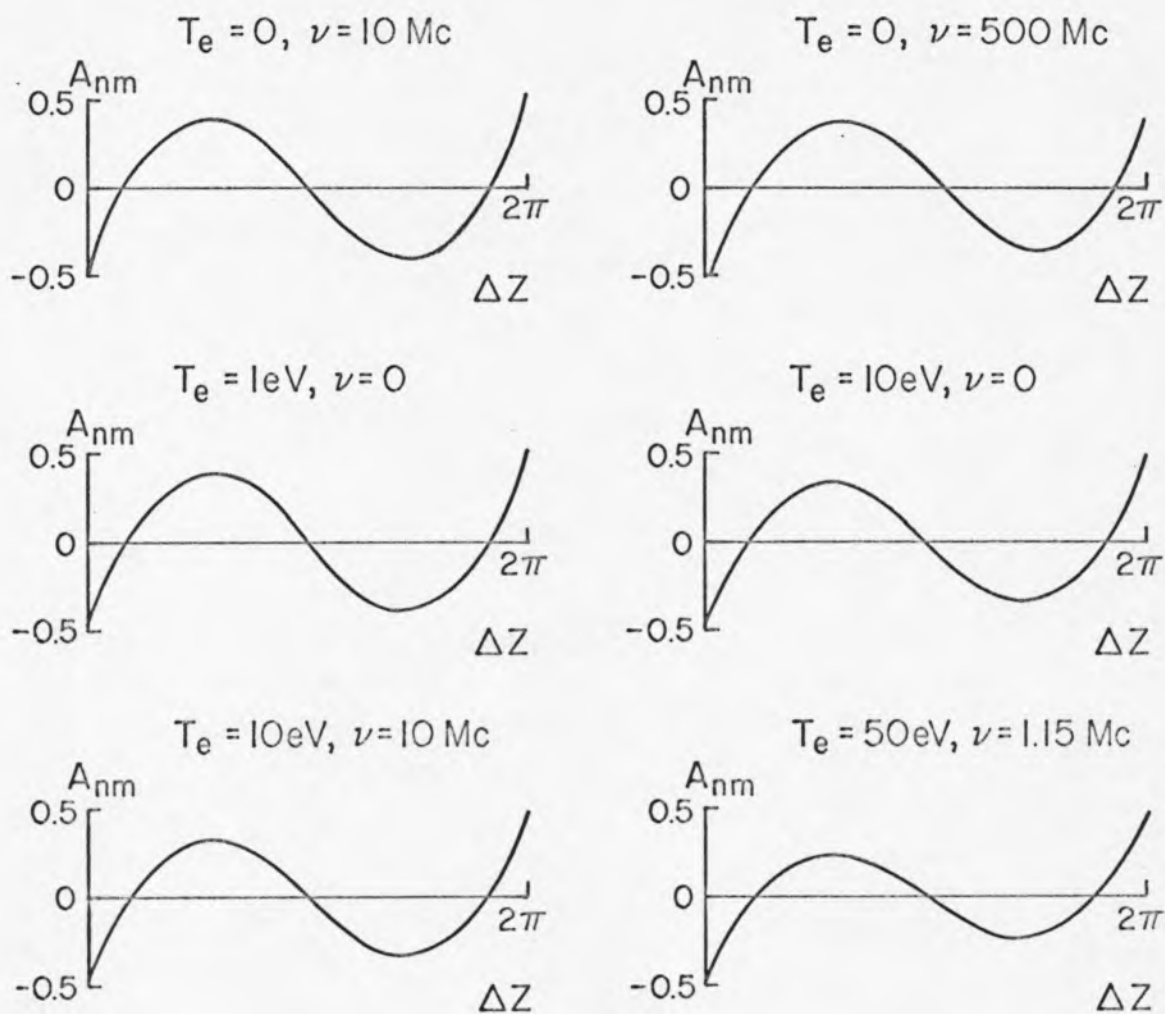


Figure 4.11 The normalized acceleration force A_{nm} as a function of ΔZ computed for $\omega/\omega_p = 0.9$ and varying values of T_e and ν .

collision frequency also modifies the effective resonant frequency of the plasma, thus changing the true ω/ω_p and also influencing the amplitude of the force law. Figure 4.9 shows the effect of increasing plasma electron temperature with $\omega/\omega_p = 0.99$ and zero collision frequency. Here there is no asymmetry, since there is simply an effective "Doppler shift" in the plasma resonant frequency due to the plasma oscillations being convected away at the plasma electron thermal speed. Figure 4.10 shows the behavior of the acceleration force A_{nm} for several sets of real plasma conditions and $\omega/\omega_p = 0.99$. Figure 4.10a represents a thermally generated cesium plasma; 4.10b, d, and e represent beam generated plasmas; and 4.10c represents a typical mercury vapor discharge. Figure 4.11 also shows a variety of plasma conditions with $\omega/\omega_p = 0.90$, illustrating the decrease in sensitivity of the acceleration force A_{nm} to plasma parameters when ω/ω_p is not near unity (off resonance).

The beam behavior computed using the acceleration force A_{nm} discussed above, for the plasma region (Region II of the theoretical model of Chapter II) is now shown in terms of the velocity-phase plots as was done for the no-plasma klystron case. The computations shown in Figure 4.12 are for a model with the vacuum region, Regions I and III, of unit length and the plasma region, Region II, 20 units in length (units of u_0/ω). The plasma electron temperature is 0.23 eV and the collision frequency 10 Mc. For Figure 4.12, the beam current is 10 ma and the initial velocity modulation V_0 is .025. The position of observation is $Z = 22$. It is seen that the velocity phase plots exhibit the same type of behavior for decreasing

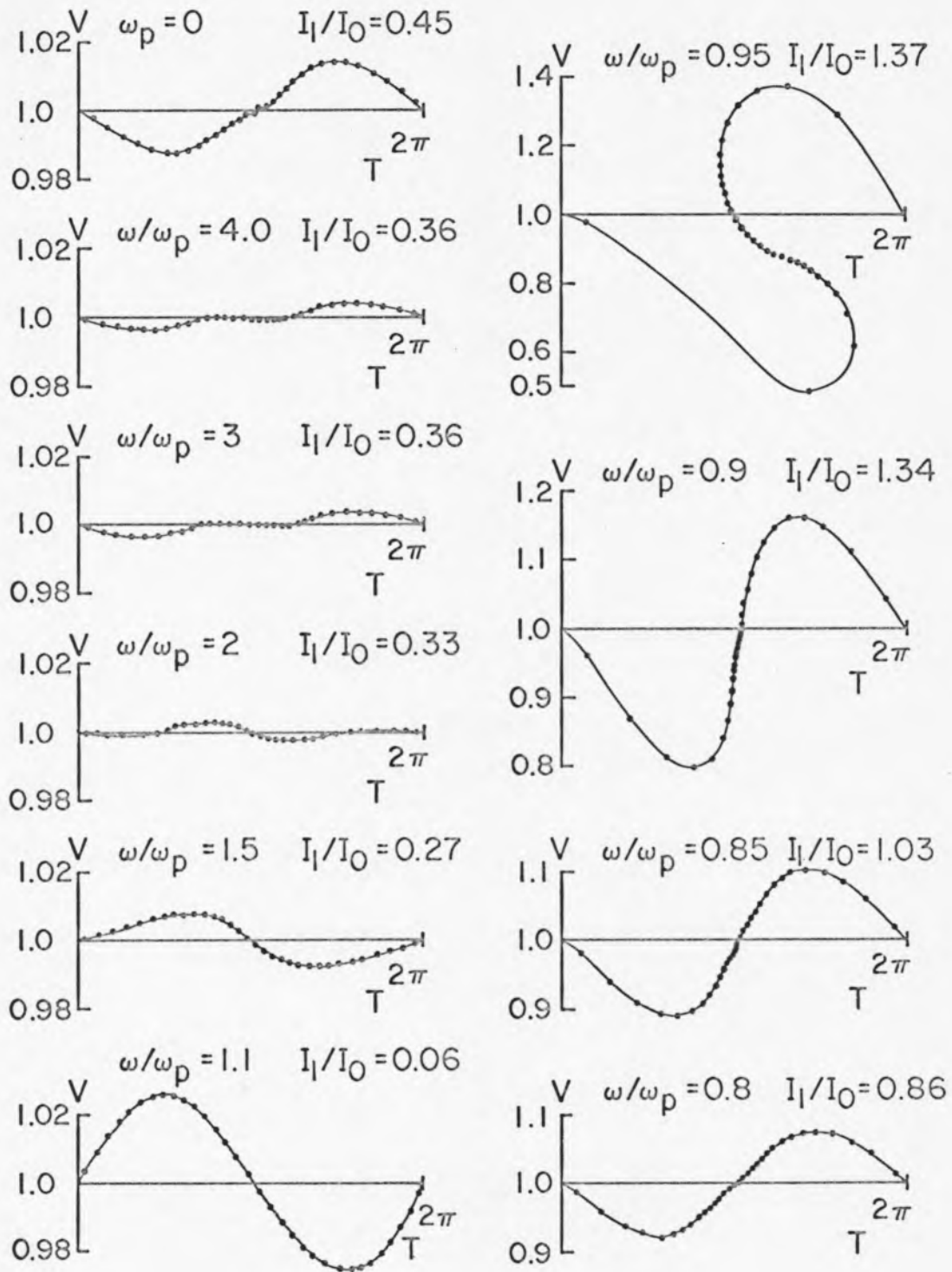


Figure 4.12 Velocity-phase plots at $Z = 22$ computed for $I_0 = 10$ ma and $V_0 = 0.025$ varying the parameter ω/ω_p

ω/ω_p (but $\omega/\omega_p > 1$) as seen in Figure 4.5 for increasing beam current. Hence for $\omega/\omega_p > 1$ the plasma has the effect of increasing the repulsive space charge forces between the beam discs (electrons) and prevents bunching. For $\omega/\omega_p = 1.5$ the point of maximum I_1/I_0 occurs at $Z = 18$ and the phase reversal of the velocity modulation is already complete at $Z = 22$, thus the space charge effect due to the presence of the plasma is the same as for a beam of four to five times the charge density of the beam being considered. For the plot of $\omega/\omega_p = 1.1$, the maximum I_1/I_0 occurs at $Z = 10$ and the velocity-phase plot at $Z = 22$ shows nearly full initial velocity modulation with almost no bunching, indicating that $Z = 22$ is approximately one-half space charge wavelength and the effective beam charge density is approximately 10 times the true beam charge density. In the same way that the acceleration force changes abruptly, the velocity phase plots change abruptly as ω/ω_p changes from a value of $\omega/\omega_p > 1$ to a value of $\omega/\omega_p < 1$. There is no parallel to beam behavior in the absence of a plasma since without the attractive acceleration force due to the plasma, the increase in velocity modulation is not possible. It is seen that for all values of $\omega/\omega_p < 1$, the velocity-phase plots show increased velocity modulation and bunching exceeding that for $\omega_p = 0$, as indicated by the I_1/I_0 ratio. In addition for the cases of $\omega/\omega_p = 0.95$ and $\omega/\omega_p = 0.9$ the bunching exceeds the maximum obtainable in the absence of the plasma. As the ratio of ω/ω_p decreases to 0.85 and 0.8, the degree of bunching decreases also and the velocity-phase plots show evidence of space charge forces limiting the bunching. Figure 4.13 shows the

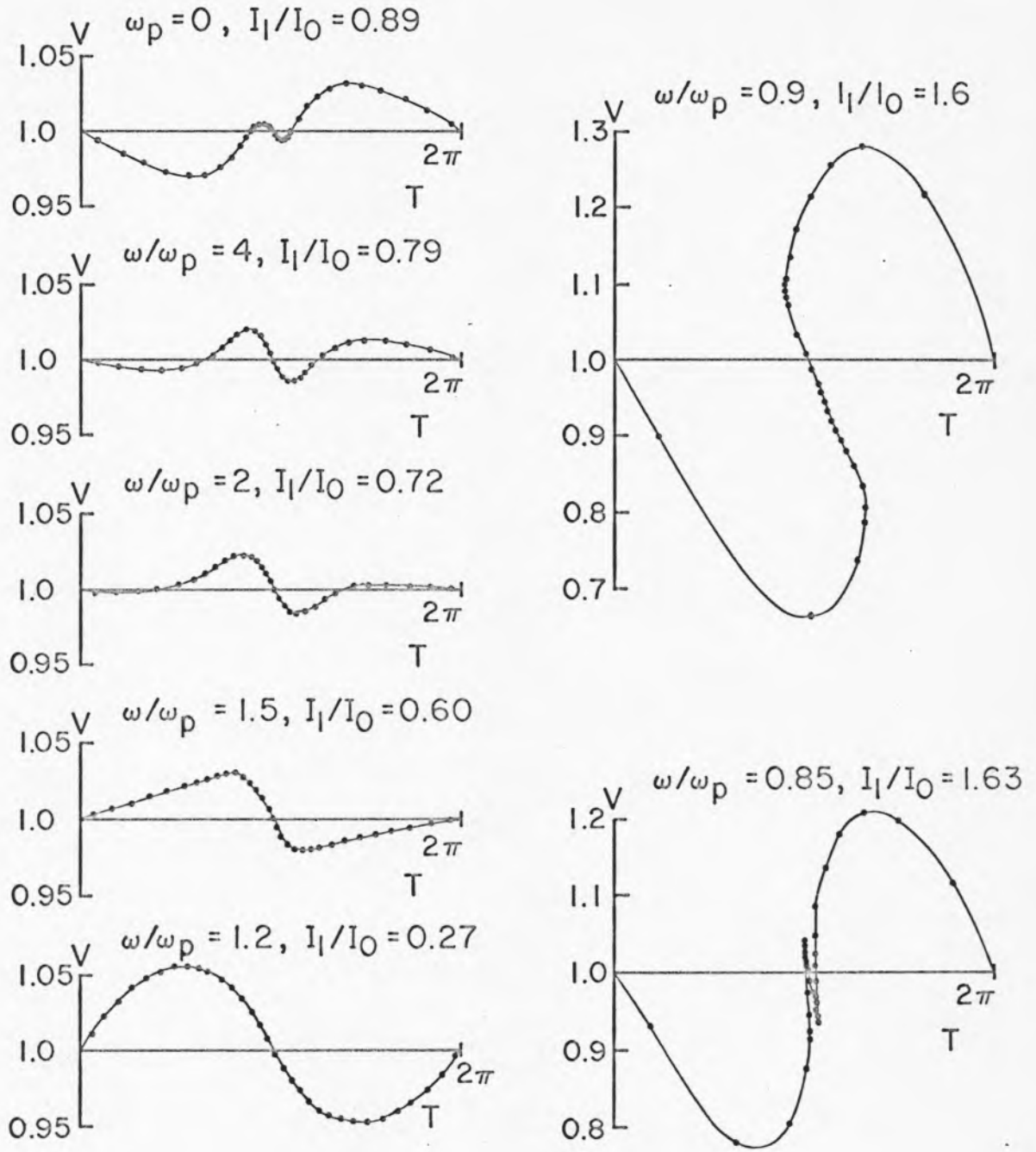


Figure 4.13 Velocity-phase plots computed for $I_0 = 10$ ma and $V_0 = 0.05$, varying the parameter ω/ω_p

behavior of a beam of the same space charge density with a higher percentage of initial velocity modulation. Again the beam appears to increase its effective charge density as ω/ω_p decreases, with the behavior changing abruptly as ω/ω_p becomes less than one. This case illustrates the high degree of bunching possible with $\omega/\omega_p < 1$ due to the discs exerting forces of attraction rather than repulsion. The maximum ratio of I_1/I_0 for the case of $\omega/\omega_p = 0.9$ is 1.63 and occurs at $Z = 21$. The maximum I_1/I_0 for the case of $\omega/\omega_p = 0.85$ does not occur until $Z = 25$ and is 1.71, the maximum value observed for the cases considered in this study. Note that the velocity-phase plot of Figure 4.13 for $\omega/\omega_p = 0.85$ shows evidence of the action of repulsive space charge forces in the region of tightly bunched discs, as should be expected from the behavior of the acceleration force seen in the case for $\omega/\omega_p = 0.85$ of Figure 4.7. The effect of the plasma on the beam behavior also depends on the importance of the beam space charge forces in the absence of the plasma. Hence, as seen in Figure 4.14, the modification seen in the beam behavior is directly proportional to beam current (charge density), increasing current having the effect of increasing the forces of both repulsion and attraction, depending on the ratio of ω/ω_p .

While the calculated velocity-phase plots show both the velocity-phase distribution and the density-phase distribution (the number of discs in a given phase interval), the reduced experimental velocity-phase plots show only the velocity-phase information. Thus the computed density-phase information (T_i) is used to construct a current waveform as described in Chapter II by simply "smearing out"

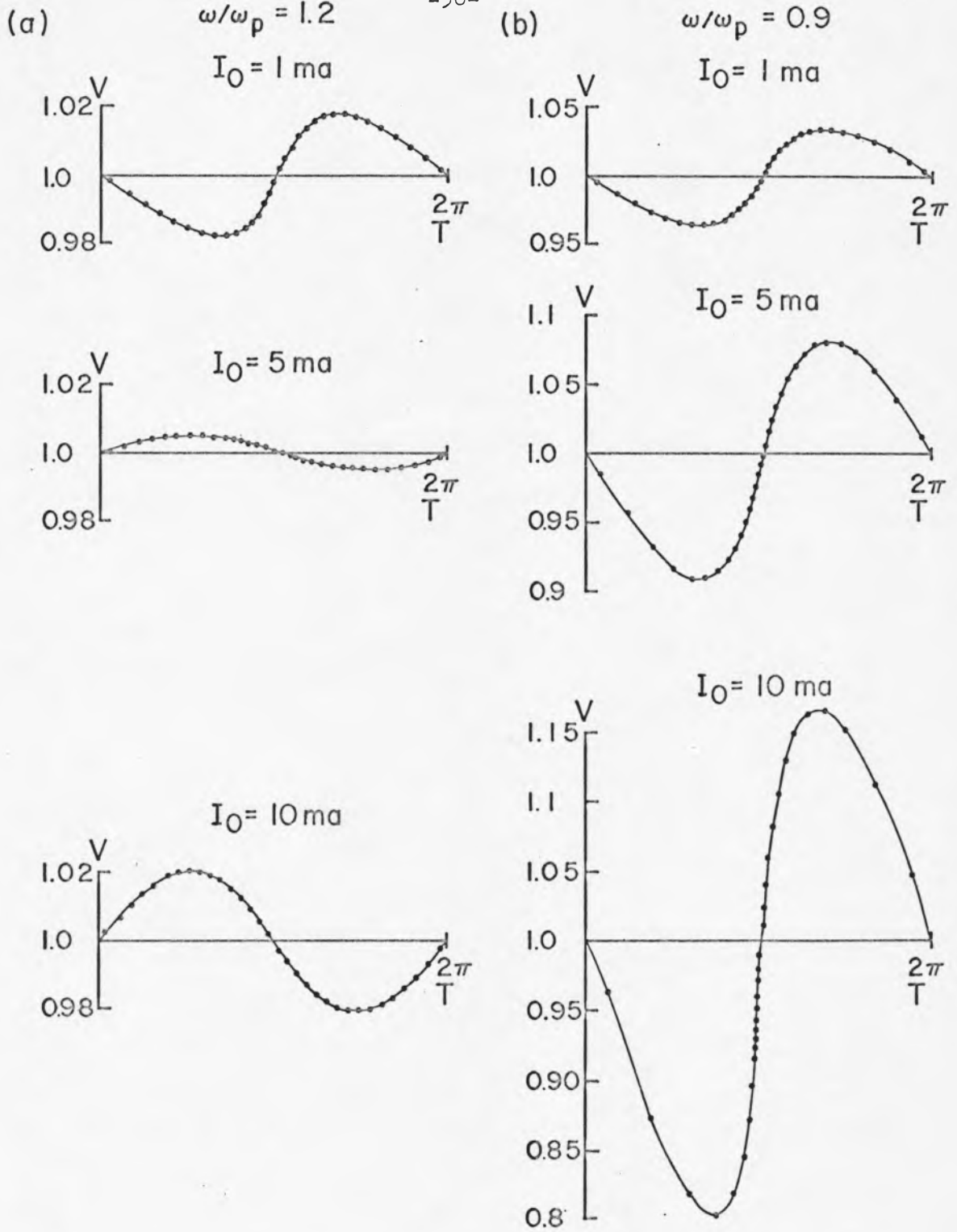


Figure 4.14 Velocity-phase plots computed for $V_0 = 0.025$, $T = 0.13 \text{ eV}$, $v = 10 \text{ Mc}$, showing the effect of increasing current with (a) $\omega/\omega_p = 1.2$ and (b) $\omega/\omega_p = 0.9$

(in time) the current contribution of each disc and summing over all the discs. A set of computed velocity-phase plots and the corresponding current waveforms are shown in Figure 4.15. If a smooth curve is drawn through the points representing the discs in the velocity phase plots of Figure 4.15, the computed results then have the same form as the experimental results. The computed current waveforms will be shown by dashed lines to prevent confusion with experimental waveforms.

Since early experimental results failed to show the sharp transition from repulsive to attractive space charge forces at $\omega/\omega_p = 1$ as predicted by theoretical computation, it was thought that a non-uniform axial plasma distribution might be responsible, and computations were made dividing the plasma region into five regions with densities determined by the scheme shown in Figure 4.16. While this approximation is not without faults, it leads to some interesting results. Figure 4.17 shows the velocity-phase plots and current waveforms for several cases computed. When $\omega/\omega_{p0} > 1$, the behavior is not very different from the situation in which the plasma is uniform. When $\omega/\omega_{p0} < 1$, however, the behavior is quite different. Depending on the value of ω/ω_{p0} , ω/ω_{pC} , and possibly ω/ω_{pB} may be larger than unity, and the disc trajectories become quite complicated. Figure 4.18 shows the phase trajectories for the computations of Figure 4.17 and an additional catastrophic case with $\omega/\omega_{p0} = 0.96$. For $\omega/\omega_{p0} = 0.96$ the plasma density in Region A, the center region is sufficiently near the "resonance" condition to cause what might be considered beam break-up. Some of the slower electrons with initial

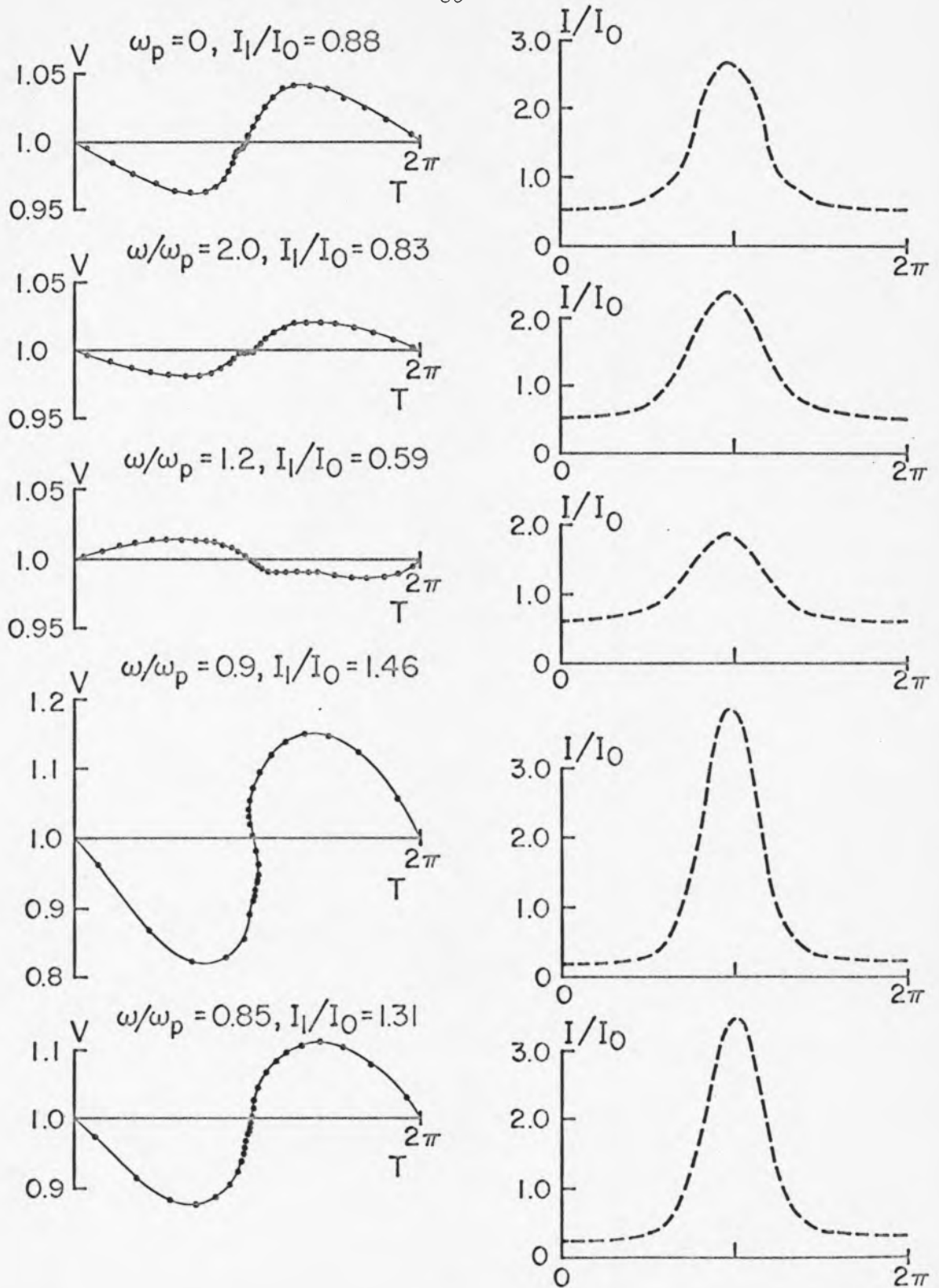
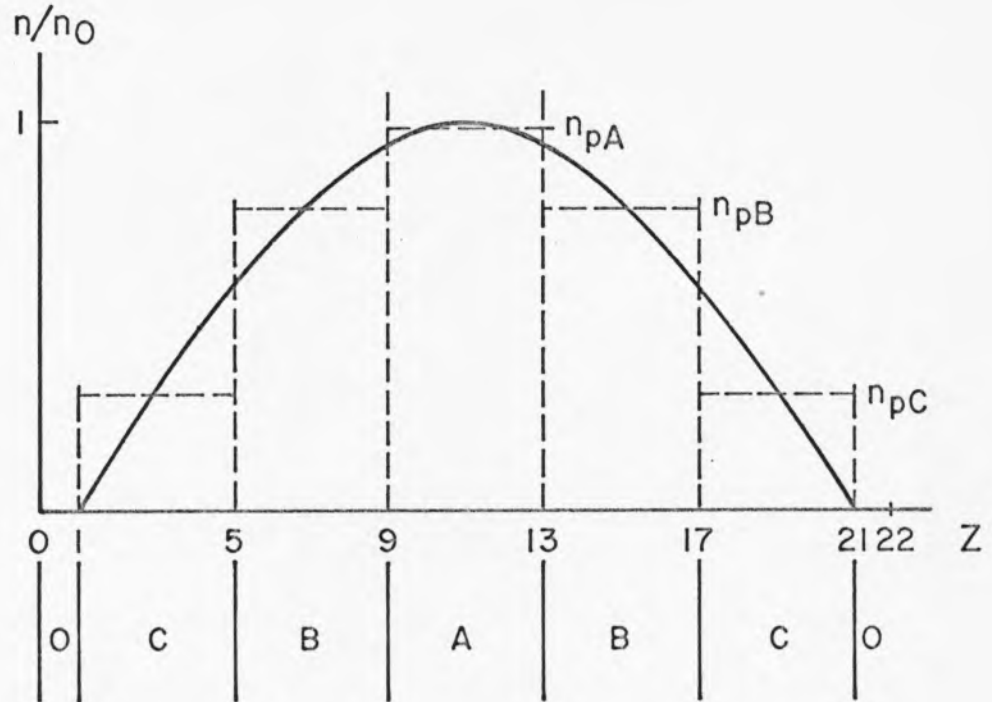


Figure 4.15 Velocity-phase plots with corresponding current waveforms computed for $I_0 = 5$ ma, $V_0 = .054$ and varying the parameter ω/ω_p .



REGION O , $n_p = 0$, $\omega_p = 0$

REGION C , $n_{pC} = 0.294 n_0$, $\omega/\omega_{pC} = 1.85 \omega/\omega_{p0}$

REGION B , $n_{pB} = 0.769 n_0$, $\omega/\omega_{pB} = 1.15 \omega/\omega_{p0}$

REGION A , $n_{pA} = 0.975 n_0$, $\omega/\omega_{pA} = 1.03 \omega/\omega_{p0}$

$$1 \leq Z \leq 21 \quad , \quad n = n_0 \sin \frac{\pi(Z-1)}{20}$$

Figure 4.16 Model for approximating sinusoidally varying axial plasma density profile

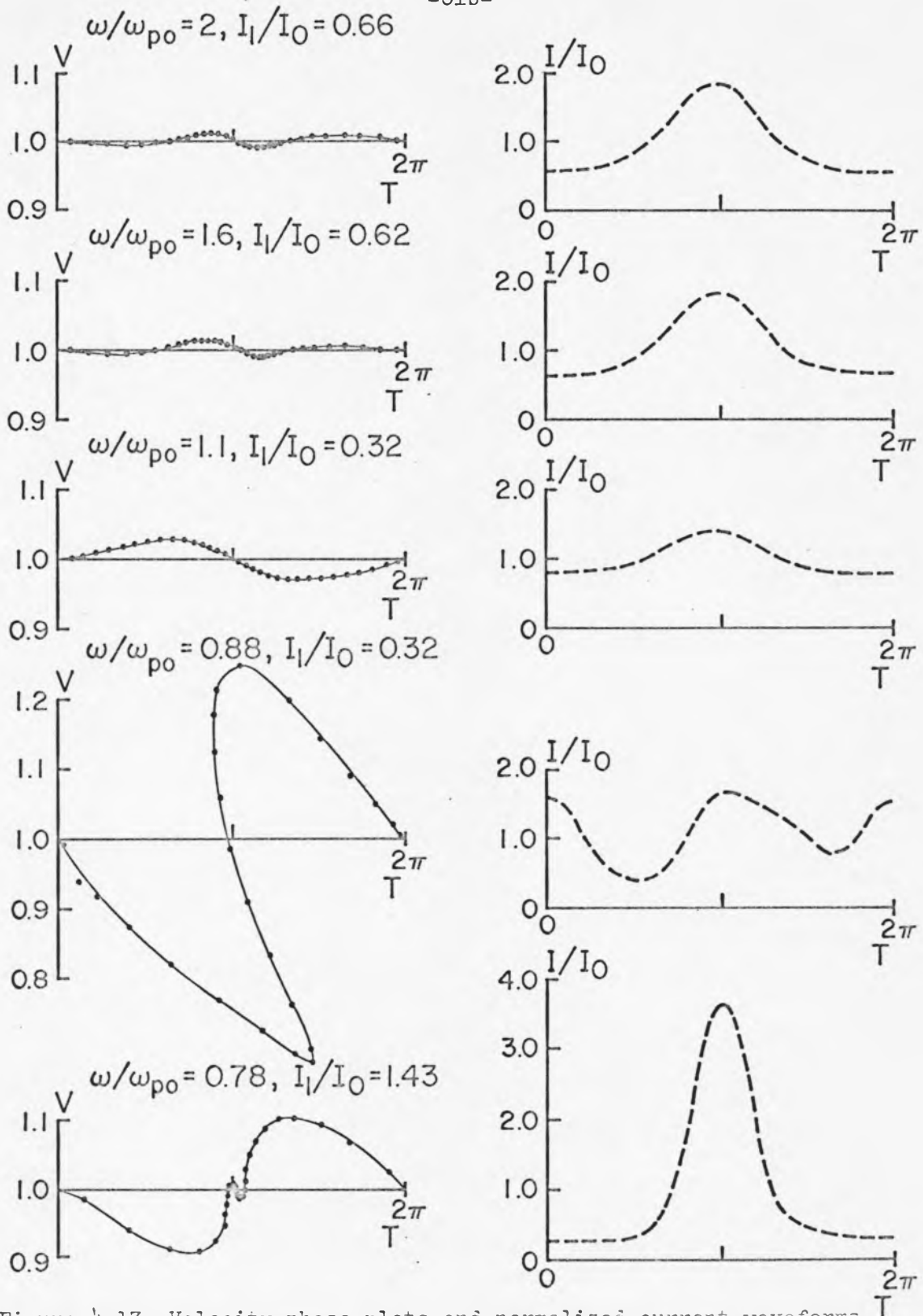


Figure 4.17 Velocity-phase plots and normalized current waveforms computed for $I_0 = 10$ ma, $V_0 = .05$, with the axial plasma density distribution of Figure 22.

phase less than π are so strongly attracted to the bunch that they are nearly brought to rest, and the magnitudes of their phases relative to the rest of the discs in the cycle is too large at $Z = 17$ to permit further computation. For $\omega/\omega_{po} = 0.88$ it is seen that the repulsive forces in region B reverse the disc velocities in the vicinity of $Z = 7$, and upon entering the region in which the forces become attractive (at $Z = 9$), the discs tend to bunch in phase near zero and 2π ! Since the discs are in close proximity physically (or in phase) when they enter the region of repulsive force at $Z = 13$, they strongly repel one another and some discs achieve sufficient velocity (momentum) to accomplish crossover near $Z = 19$. As can be readily seen from the current waveform for $\omega/\omega_{po} = 0.88$ in Figure 4.17, two bunches instead of one occur and the axial plasma density distribution has effectively doubled the modulation frequency. For $\omega/\omega_{po} = 0.78$, the behavior is less radical, and the beam discs are seen to approach the bunch in a rather desirable manner from the amplification standpoint. Here the increased velocity modulation in the regions of attractive force is decreased in the final region where the force is repulsive. Thus a fairly high degree of bunching is obtained with an actual decrease in velocity modulation from the initial value. It can be seen from the velocity-phase plot for $\omega/\omega_{po} = 0.78$ of Figure 4.17 that approximately 50 percent of the charge is bunched near $T = \pi$ with less than a 2 percent velocity spread. Figure 4.19 shows the velocity-phase plots at the boundaries between the plasma regions for the cases with $\omega/\omega_{po} < 1$ and illustrate the effects due to the interaction in each region. While

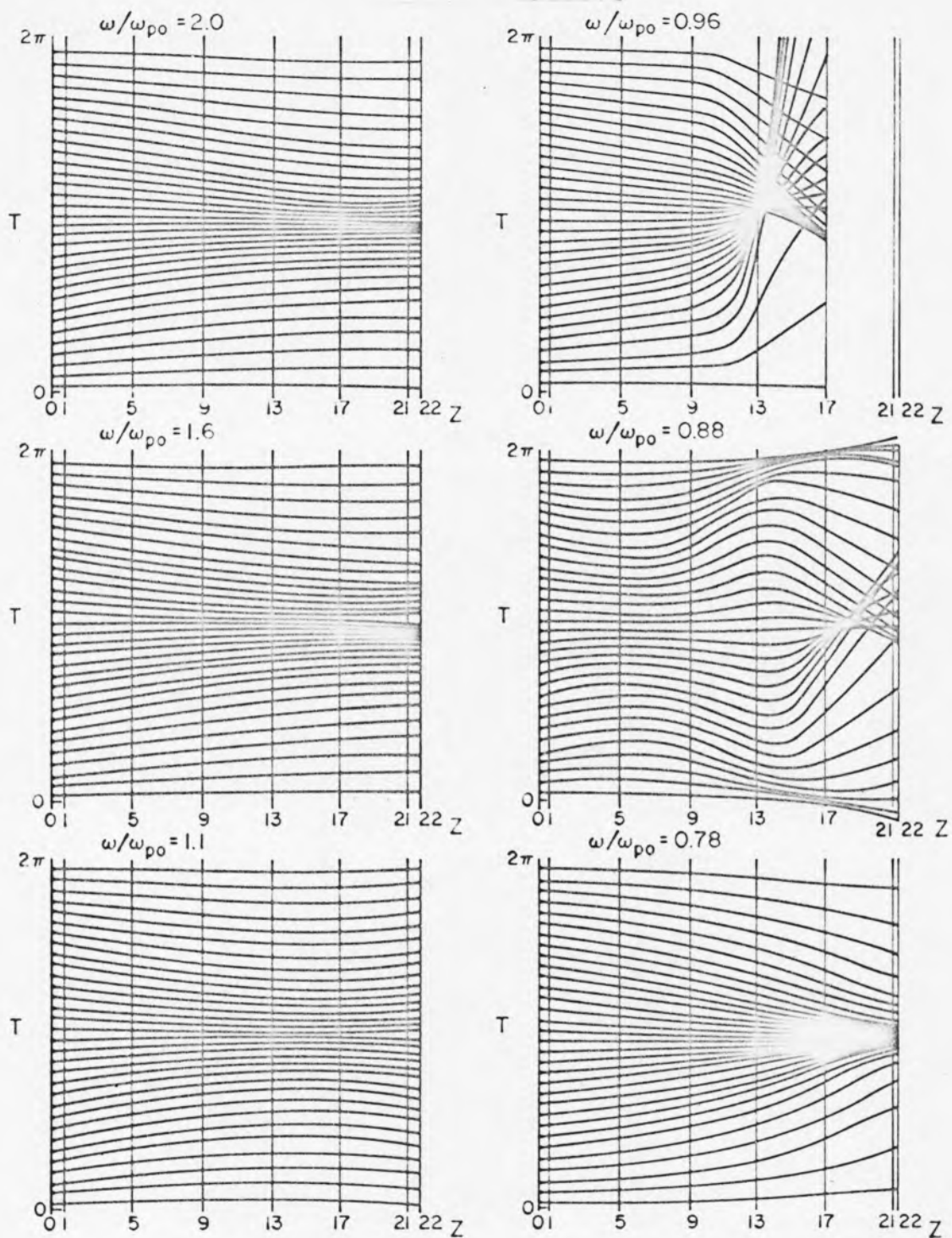


Figure 4.18 Phase trajectories computed for $I_0 = 10$ ma, $V_0 = 0.05$ with the axial plasma density distribution of Fig. 22

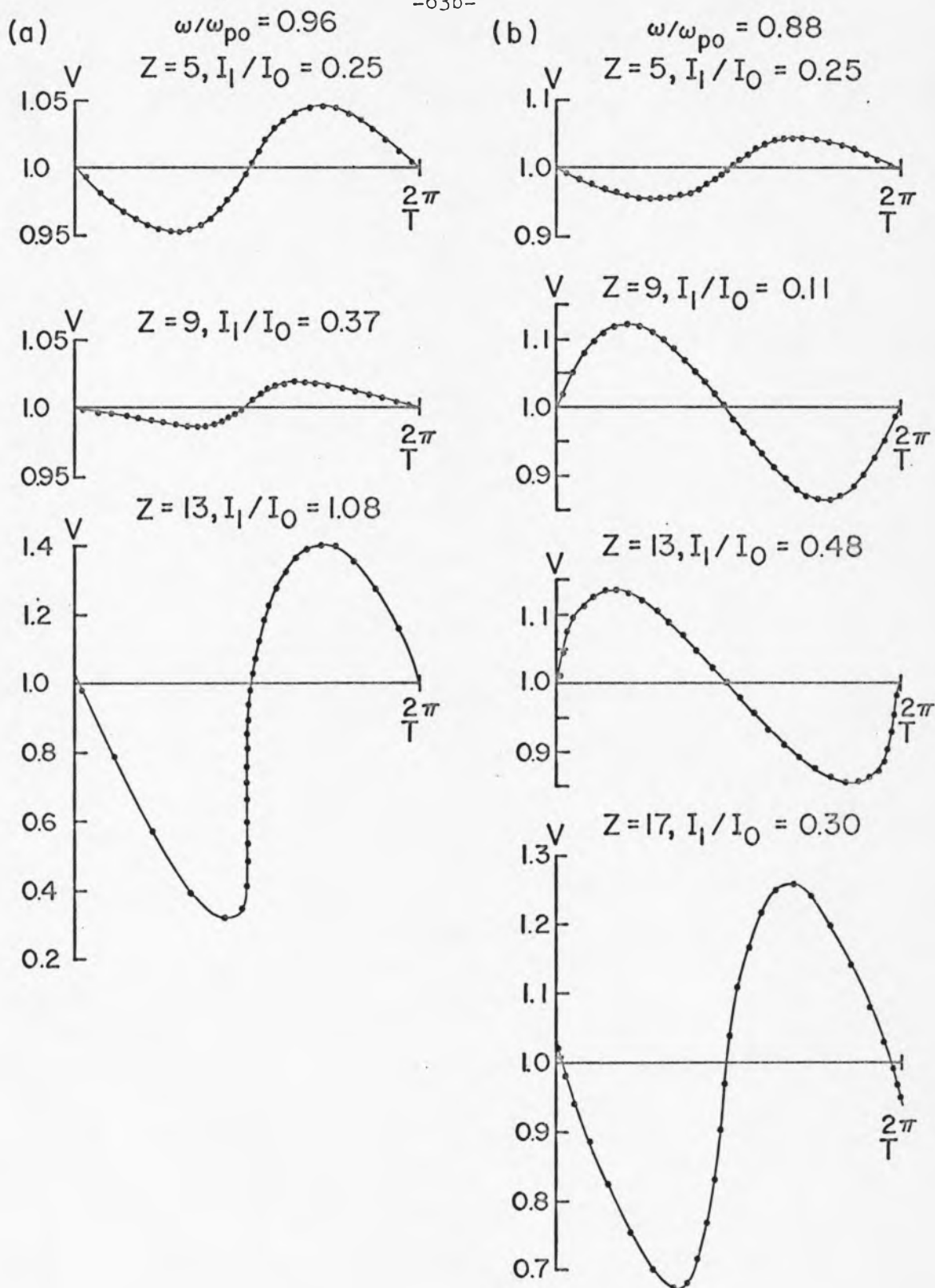


Fig. 4.19 Velocity-Phase plots at the boundaries of the regions approximating the axial plasma density distribution shown in Fig. 22 for (a) $\omega/\omega_{p0} = 0.96$, (b) $\omega/\omega_{p0} = 0.88$

(C)

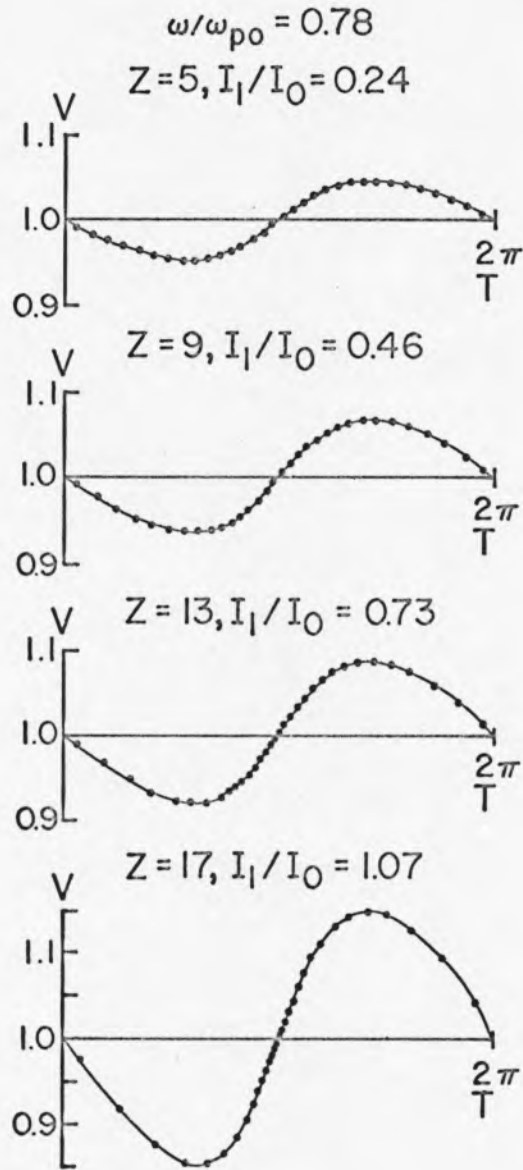


Figure 4.19 (continued)

(c) $\omega/\omega_{p0} = 0.78$. $I_0 = 10$ ma, $V_0 = 0.05$

the same information can be deduced, at least qualitatively, from the phase trajectories, the velocity-phase plots provide a quantitative emphasis of the large effects in some regions. For instance in Figure 4.19a, the velocity modulation is drastically reduced as the discs traverse the region from $Z = 5$ to $Z = 9$ by the strong repulsive force, then drastically increased in the region from $Z = 9$ to $Z = 13$. Upon studying the phase trajectories and velocity-phase plots, it becomes apparent that the amplification or bunching process will be highly nonlinear with respect to the initial velocity modulation, due to the fact that the behavior will depend on the bunching present as the beam enters a region of strong repulsive or attractive force. Thus, as seen earlier in the behavior of the acceleration force, when a beam which is already tightly bunched enters a region of strong attractive force ($\omega/\omega_p \lesssim 1$) the forces which act may be small due to the fact that an equilibrium position exists for small interparticle spacing and the behavior will be affected very little. On the other hand, when a tightly bunched beam enters a region in which interparticle forces are strongly repulsive ($\omega/\omega_p \gtrsim 1$), strong forces act to separate the particles and the behavior is greatly modified. Conversely, a beam which is not bunched will be little affected by entering a region where the forces are repulsive, but will be strongly influenced upon entering a region where the force becomes attractive. Thus in the case of $\omega/\omega_{p0} = 0.96$, the discs are kept from bunching by the strong repulsive force in region B, ($\omega/\omega_p = 1.1$) and because of this they enter region A with relatively large inter-disc spacings

and the discs strongly attract one another resulting in the large velocity spread and its catastrophic effect. If the initial velocity modulation had been sufficiently large in this case, sufficient bunching might have occurred in spite of the repulsive force in region B, so that the bunch would simply have become tighter and the velocity modulation increased somewhat for discs not in the bunch in region A. Thus the behavior illustrated in these cases of profiled plasma density indicate that bunching efficiency depends not only on the density profile, but on the compatibility of the bunching progress to the profile. This means that the beam should enter regions of repulsive force with a relatively high degree of velocity modulation but little bunching, and regions of attractive force with the opposite properties. This appears to be accomplished fairly well for the case with $\omega/\omega_{po} = 0.78$ and initial velocity modulation $V_0 = 0.05$ shown in Figures 4.17 and 4.18. Thus it is seen that the plasma greatly influences the beam behavior and for certain conditions, the bunching of the beam electrons is significantly enhanced.

B. Experimental Results

As described in Chapter III, the experimental results are processed and presented in the form of velocity-phase plots and normalized current-phase waveforms. A sufficient number of points are read from the raw data photographs, like those of Figure 4.10, to preserve detail in the process of correcting phase, normalizing, and replotting. These processed experimental plots are shown as solid, smooth curves, omitting the arbitrarily selected construction points

to avoid confusion with computed points, which represent discs and therefore have special significance. The computed current waveforms are shown as dashed curves to maintain a consistent representation. All the plots seen in the figures of this section are for the normalized drift distance $Z = 22$, which is the length of the experimental beam-plasma interaction region. An additional parameter appears with the experimental results--the background pressure of the vacuum chamber p_0 . As will be seen, the beam-generated plasma depends on this parameter and thus the ratio ω/ω_p . Where the ratio I_1/I_0 is given, it pertains to the theoretical plot shown.

The first experiments were performed as an attempt to investigate experimentally the $\omega_p = 0$ case--the nonlinear klystron interaction. The vacuum system was pumped to the best obtainable pressure p_0 of about 5×10^{-6} torr, and experiments were performed at various values of beam current and initial velocity modulation. Figures 4.20 and 4.21 show typical results of these experiments. As seen in Figure 4.20, for small beam currents and velocity modulation ($I_0 = 0.5, 1, 2\text{ma}$; $V_0 = .025$) the agreement appears to be within the accuracy of the experimental technique. The current waveform for the 2 ma beam indicates a higher degree of bunching than theoretically predicted and the velocity-phase plots for the 5 ma and 10 ma beams indicate that stronger repulsive space charge forces are acting on the beam than predicted from the beam current density. The velocity-phase plots for the 0.5 ma, 1 ma, and 2 ma beam also show a slightly smaller amplitude of velocity modulation than predicted--also an

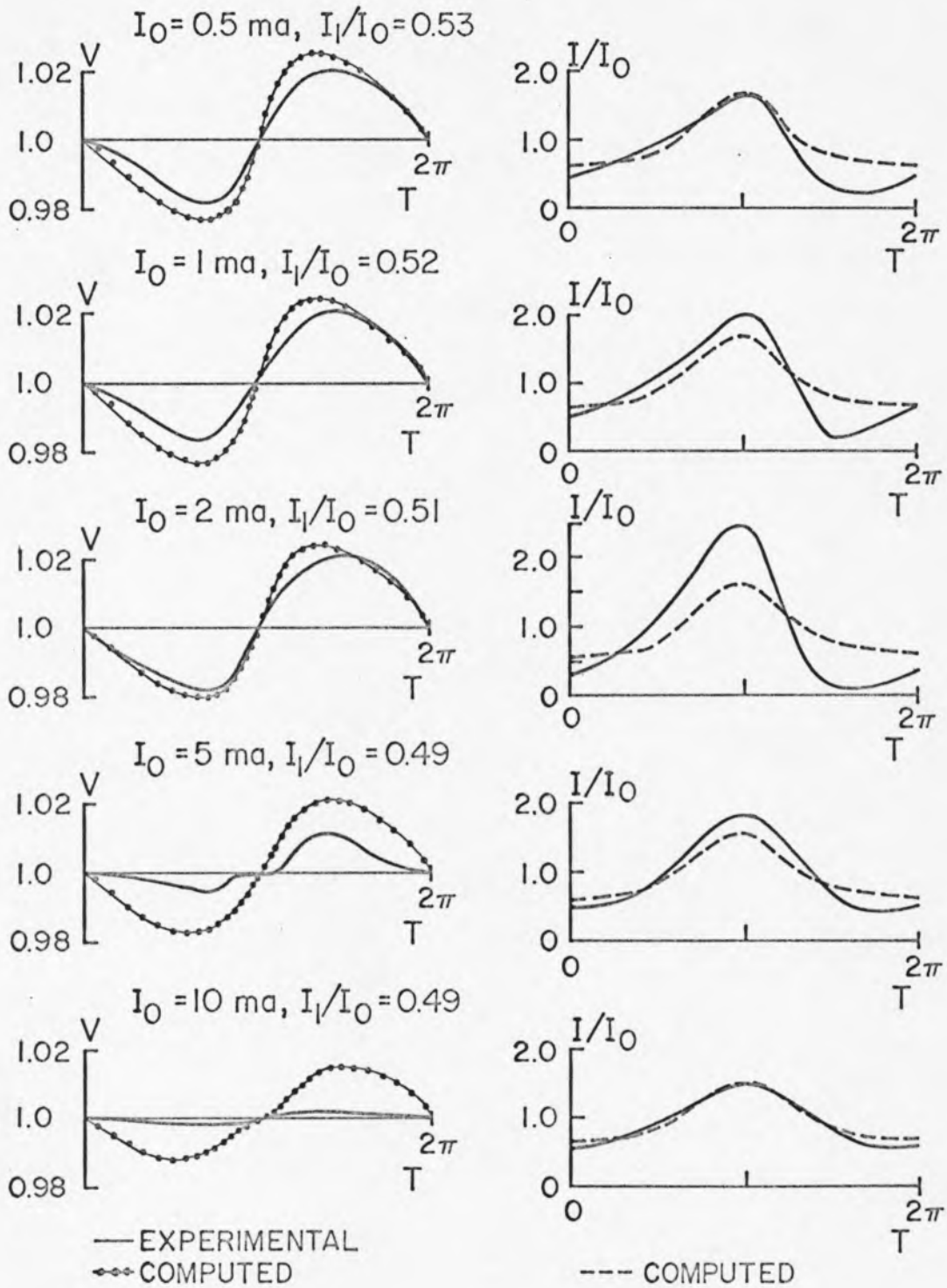


Figure 4.20 Comparison of Experimental velocity-phase and current plots obtained for $p_0 = 5 \times 10^{-6}$ with theoretical velocity-phase and current plots computed for $\omega_p = 0$, with $V_0 = 0.075$ and varying current I_0 .

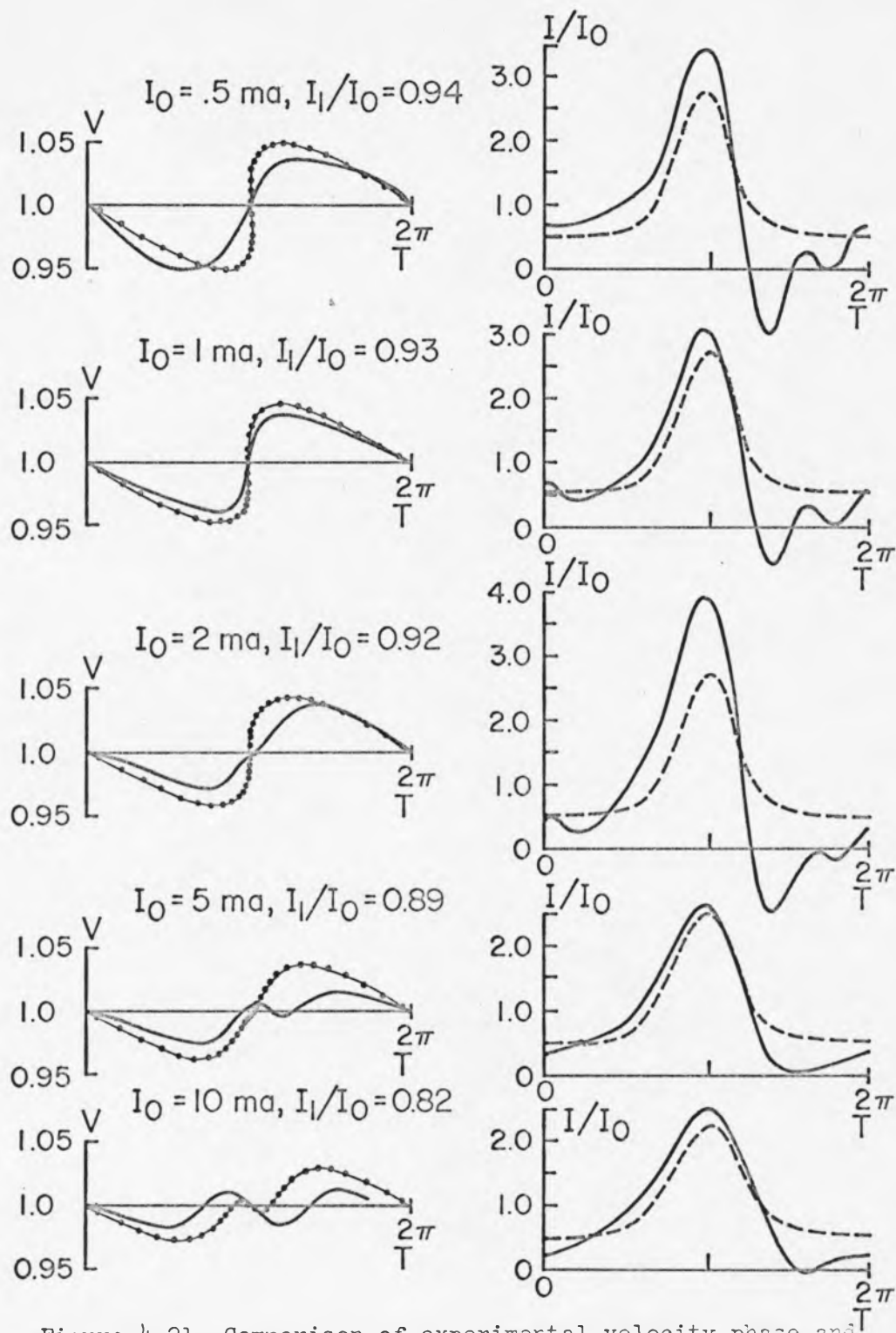


Figure 4.21 Comparison of experimental velocity-phase and current plots obtained for $p_0 = 5 \times 10^{-6}$ with theoretical velocity-phase and current plots computed for $\omega_p = 0$, with $V_0 = .05$ and varying current I_0 .

effect produced by an increase in space charge repulsion. This effective increase in repulsive space charge force is to be expected if a plasma is generated by the beam and trapped by the magnetic field. If this is the case, an increase in the initial velocity modulation, which causes the beam to bunch more tightly, should produce stronger repulsive space charge effects in the beam behavior. The velocity-phase plots of Figure 4.21 verify that this is the case, since even the 2 ma beam now displays the effect of repulsive space charge forces which are larger than those predicted for this current density with $\omega_p = 0$. To estimate the plasma density necessary to produce this effect, note the behavior of the experimental velocity-phase plots for the 10 ma beam. For $V_0 = 0.025$, the velocity modulation has nearly vanished. For $V_0 = 0.05$, the velocity modulation is only partially reduced, but the increased space charge forces cause the electrons to be "reflected" from the bunch near $T = \pi$ to a larger extent than displayed by the computed $\omega_p = 0$ case. Now, return to Figures 4.12 and 4.13 which show the velocity-phase plots for the 10 ma beam with ω/ω_p as a parameter. It is seen that for $\omega/\omega_p \sim 3$ to 4 , the velocity-phase plots show very nearly the same behavior as the experimental plots of Figures 4.20 and 4.21 for the 10 ma beam. If the beam-generated plasma has an ω/ω_p ratio of 3.5, the corresponding plasma density n_p is approximately $10^9/\text{cm}^3$. This is somewhat higher than expected.

Hedvall (17) has made measurements on beam-generated plasmas in the pressure range 5×10^{-5} to 10^{-3} torr with beam current densities ranging from 30 ma/cm^2 to 200 ma/cm^2 . The 10 ma beam has a current density of approximately 80 ma/cm^2 . Hedvall shows results for a

current density of 71 ma/cm^2 with one kilovolt acceleration potential for only three pressures. The lowest pressure for which he gives results is 7×10^{-5} and the beam-generated plasma density at this pressure is about $1.5 \times 10^9/\text{cm}^3$. Dunn and Self (18) have analyzed theoretically the density and potential profiles of beam-generated plasmas. Their results show that at low pressures, the beam-generated plasma density should be linearly proportional to the product of gas pressure and beam current density, that is

$$n_p \sim n_b p_0$$

where n_b is the beam electron density. Hedvall's results do not show this kind of behavior, but instead a relation of the form

$$n_p \sim n_b^r p_0^t$$

where the exponents r and t are constant only over limited current and pressure ranges. Consequently, extrapolating to lower pressures from Hedvall's experimental curves is somewhat questionable. If one does this, however, the plasma density generated by a beam corresponding to the 10 ma beam with $p_0 = 5 \times 10^{-6}$ torr is approximately $5 \times 10^8/\text{cm}^3$. Using Dunn and Self's calculation, the plasma density is given by

$$n_p = \frac{NV_0^{1/2}}{0.344} \left(\frac{m_i}{m_e}\right)^{1/2} \frac{n_b p_0 d}{\left(\frac{kT_e}{e}\right)^{1/2}}$$

where N is the number of electron-ion pairs per beam electron per cm per torr, V_0 is the beam acceleration voltage, m_i is the ion mass, and $2d$ is the length of the beam-plasma interaction region,

the rest of the quantities being self explanatory. The quantity N is a function of the gas used and the beam energy, and has a value of 3.7 for a one-kilovolt beam in argon (19). Substituting the parameters for argon with $p'_0 = 5 \times 10^{-6}$ and $T_e = 1\text{eV}$, n_p/n_b has a value of about 1.5 and the beam generated plasma density should be about $2.4 \times 10^8/\text{cm}^3$. Again this is a lower density than indicated by the velocity-phase diagrams; however, this value of n_p/n_b is outside the limit set by Dunn for the applicability of the theory.

An experiment was performed using the current probe to collect ion current in order to verify the existence of the beam-generated plasma, and to determine the plasma density dependence upon background pressure p_0 and beam current. With the probe biased at -22 volts and positioned about one centimeter away from the center of the electron beam (no beam current intercepted) the probe current is essentially ion current, and should be directly proportional to plasma density. Figure 4.22 shows the variation of probe current I_p with beam current (at constant pressure) and with background pressure (at constant current). In both cases the dependence appears linear over the range of interest. Since the probe was not designed for use as a Langmuir probe, and the collecting area is uncertain, no attempt is made to obtain electron density or temperature from the measurements. We can deduce, however, the pressure at which the $\omega/\omega_p = 1$ effects should appear by using the relations in 4.22a and b to determine what change in pressure is necessary to change the probe current I_p by a factor of ten. Since 4.22a shows a strictly linear relation, and 4.22b was obtained with a 2 ma current, a factor of five

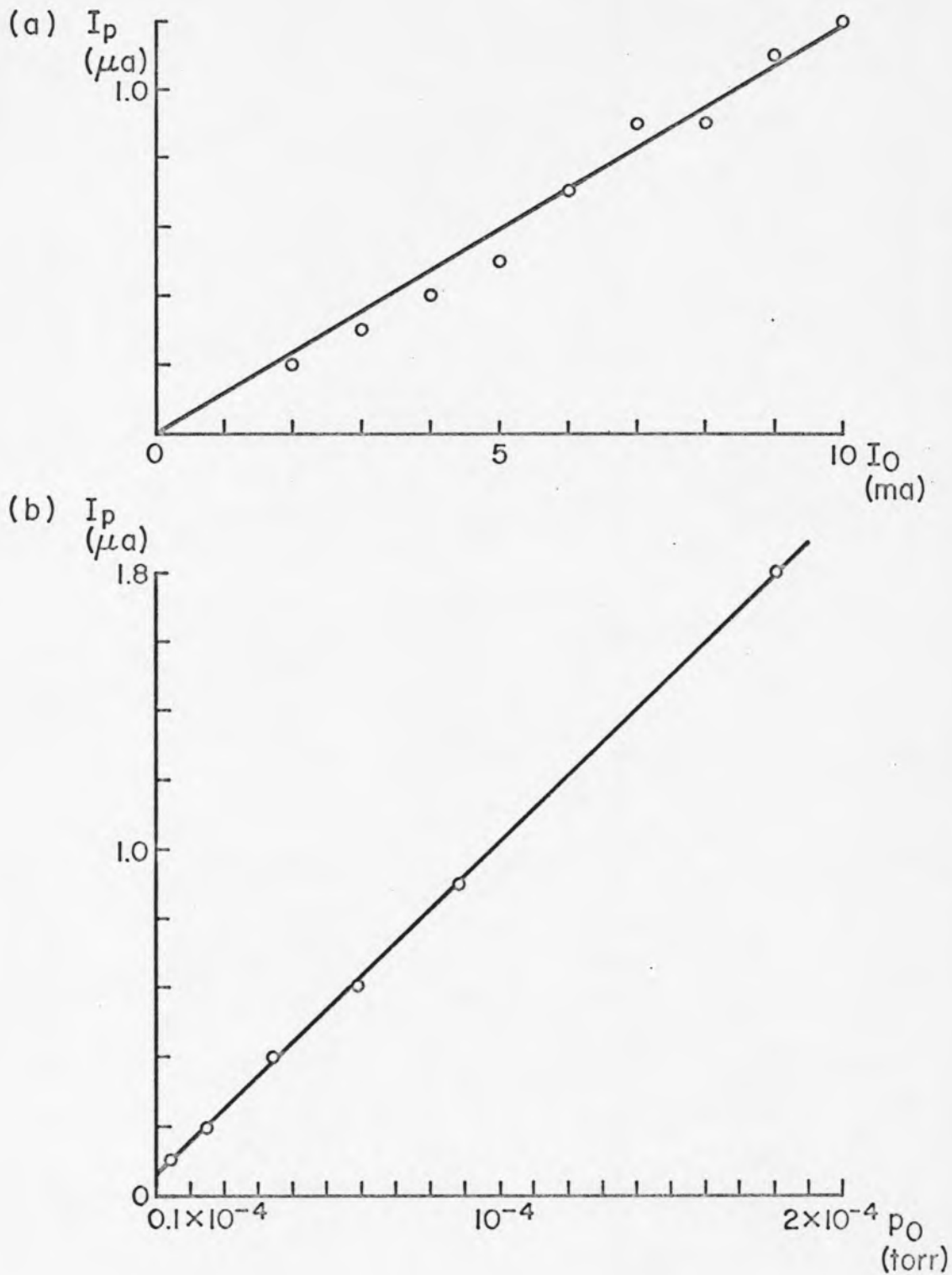


Figure 4.22 Probe current versus (a) Beam current I_0 with a background pressure $p_0 = 1.5 \times 10^{-5}$ torr; and (b) with beam current $I_0 = 2$ ma. Current is ion current with the probe biased at -22V.

is obtained by the increase in current, and from 4.22b it is seen that the remaining factor of two is obtained by increasing the pressure from $.05 \times 10^{-4}$ to $.15 \times 10^{-4}$ torr. Thus if the plasma density is 10^9 at a p_0 of 5×10^{-6} torr as indicated by the velocity-phase plots for $I_0 = 10$ ma of Figures 4.20 and 4.21, the plasma density should increase to 10^{10} by increasing p_0 to 1.5×10^{-5} torr and the transition in behavior observed at $\omega/\omega_p \sim 1$ should be observed.

Varying the background pressure p_0 in steps by admitting argon, the plasma frequency is effectively increased (ω/ω_p decreased) and Figure 4.23 shows the results for the 10 ma beam with initial velocity modulation of 0.05. Instead of a sharp transition between repulsive force behavior and attractive force behavior at $\omega/\omega_p = 1$, the velocity phase plots indicate an increase in repulsive forces from $p_0 = 6 \times 10^{-6}$ torr to $p_0 = 9 \times 10^{-6}$ torr, then a decrease again as p_0 is increased to 1.4×10^{-5} torr with a transition to less repulsive force than would occur if $\omega_p = 0$ at $p_0 = 2.3 \times 10^{-5}$ torr. While these velocity-phase plots exhibit a distinct change in behavior between the values of p_0 of 1.4×10^{-5} torr and 2.3×10^{-5} torr, the behavior shown in the latter case does not directly verify that the forces acting are forces of attraction, since the theory predicts that such forces increase the degree of velocity modulation, while it is seen to be decreased here. Furthermore, the theoretical results show that the change in the acceleration force has maximum influence at the transition, while the observed maxima appear to be away from the transition--the cases for which p_0 is 9×10^{-6} torr and 3×10^{-5} torr for the experiment of Figure 4.23. The current waveforms also indicate

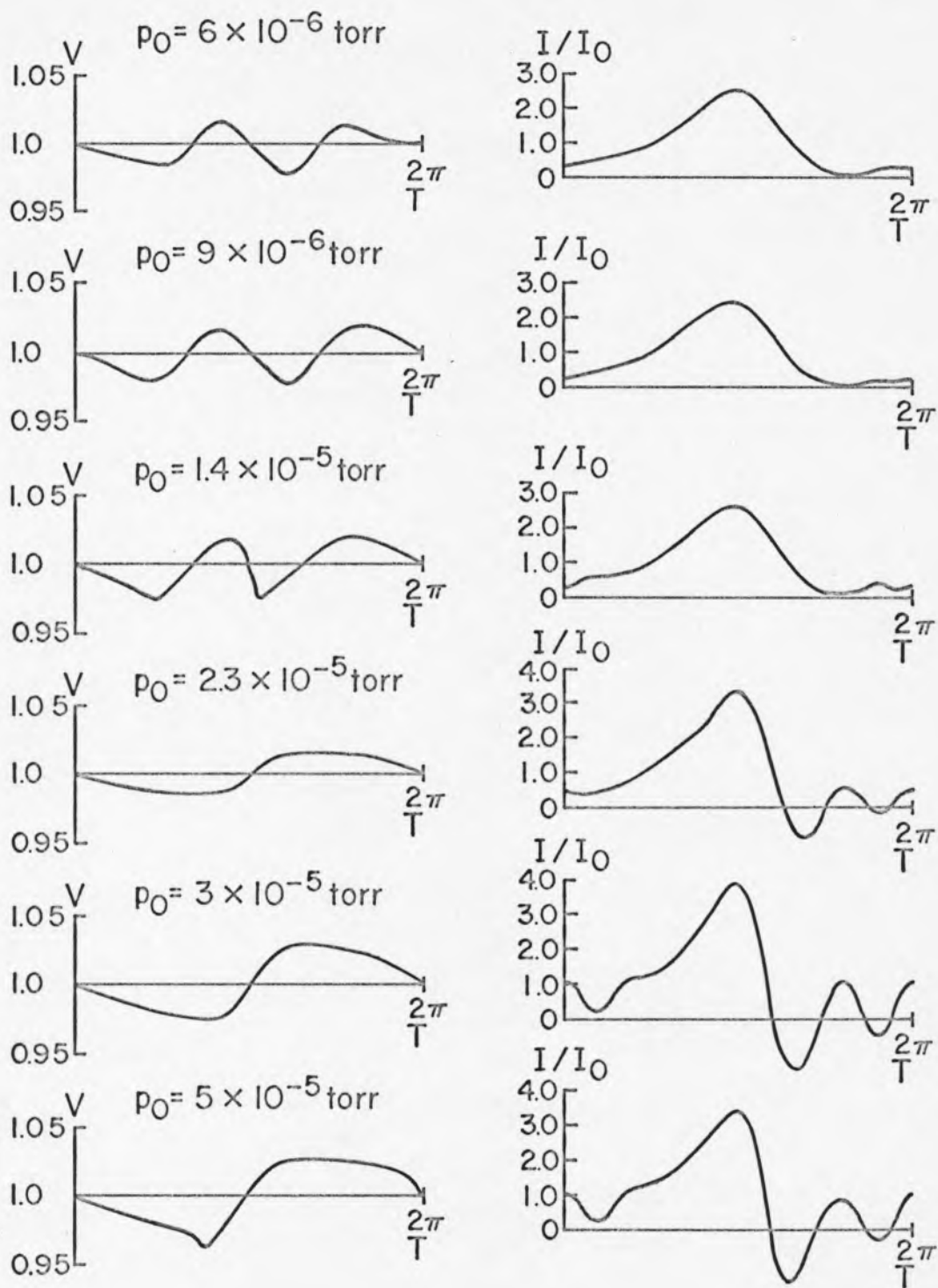


Figure 4.23 Velocity-phase and current plots for $I_0 = 10$ ma
 $V_0 = .05$ with ω_p varied by increasing background
 pressure p_0 .

that the minimum and maximum bunching occur for these values of p_0 . Note also the indication of the return of repulsive space charge effects in the velocity-phase plot for $p_0 = 5 \times 10^{-5}$ torr.

While the transition from $\omega/\omega_p > 1$ to $\omega/\omega_p < 1$ does not display the extreme behavior predicted by the computations, the transition occurs at approximately the right pressure, as predicted from the ion current measurements. The discrepancy between the plasma density inferred by these measurements and the densities obtained using the results of Dunn and Self, and Hedvall, is not too disturbing since the conditions of validity for Dunn's calculation are not well satisfied, and the experimental conditions are sufficiently different from Hedvall's to account for the discrepancy. Hedvall's experiment was performed with a pulsed electron beam so that his indicated pressure is perhaps truer than that with a continuously operating beam. He also states that by increasing the length of his measuring cavity, the plasma density is increased by a factor of 2.5 which would put the results in close agreement. The gradual rather than sharp transition in the beam behavior cannot be explained as simply. The computations for a plasma with an axial density variation predict a behavior different from that of an axially uniform plasma, but the transition from $\omega/\omega_p > 1$ to $\omega/\omega_p < 1$ still displays an abrupt change in behavior. It is possible that the model used, which represents the plasma profile by only three values of ω/ω_p is an oversimplification of the physical situation and therefore may bear little relation to reality, since for a sinusoidal axial density dependence, the beam experiences resonance interaction ($\omega \sim \omega_p$) only over a short distance. It is

also possible that in the physical situation no plasma region may exist in the steady state for which $\omega \sim \omega_p$, since for this condition the local plasma oscillations grow rapidly and the potentials associated with them grow to large values and are capable of generating more plasma by the mechanism observed by Smullin and Getty (20). If this is the case, resonance no longer occurs and the attractive forces decrease again at the location of plasma generation. On the other hand, the large local plasma oscillations may give rise to turbulence and enhanced diffusion, reducing the local plasma density and restoring repulsive forces. Since observations are made only at the end of the drift region, the effect of such localized density fluctuations may appear only as a modification in the time average of the beam behavior (since both the sampling oscilloscope and the phosphor screen of the velocity analyzer have an integrating or averaging property). Measurements are needed as a function of axial distance to check these suppositions, and unfortunately this is not feasible with the experimental technique used here.

The computations using an axially varying plasma density fail to explain directly the observed gradual transition in behavior as ω/ω_p passes through resonance ($\omega \sim \omega_p$), however, the behavior of the beam due to the axial density distribution and varying initial velocity modulation as deduced from the phase trajectories for these computations, can be observed experimentally. Figure 4.24 shows three sets of velocity-phase plots for the 10 ma beam with $p_0 = 10^{-5}$ and variation of ω_p by increasing the Penning discharge current I_{PD} . Figure 4.25 shows the corresponding current plots. The

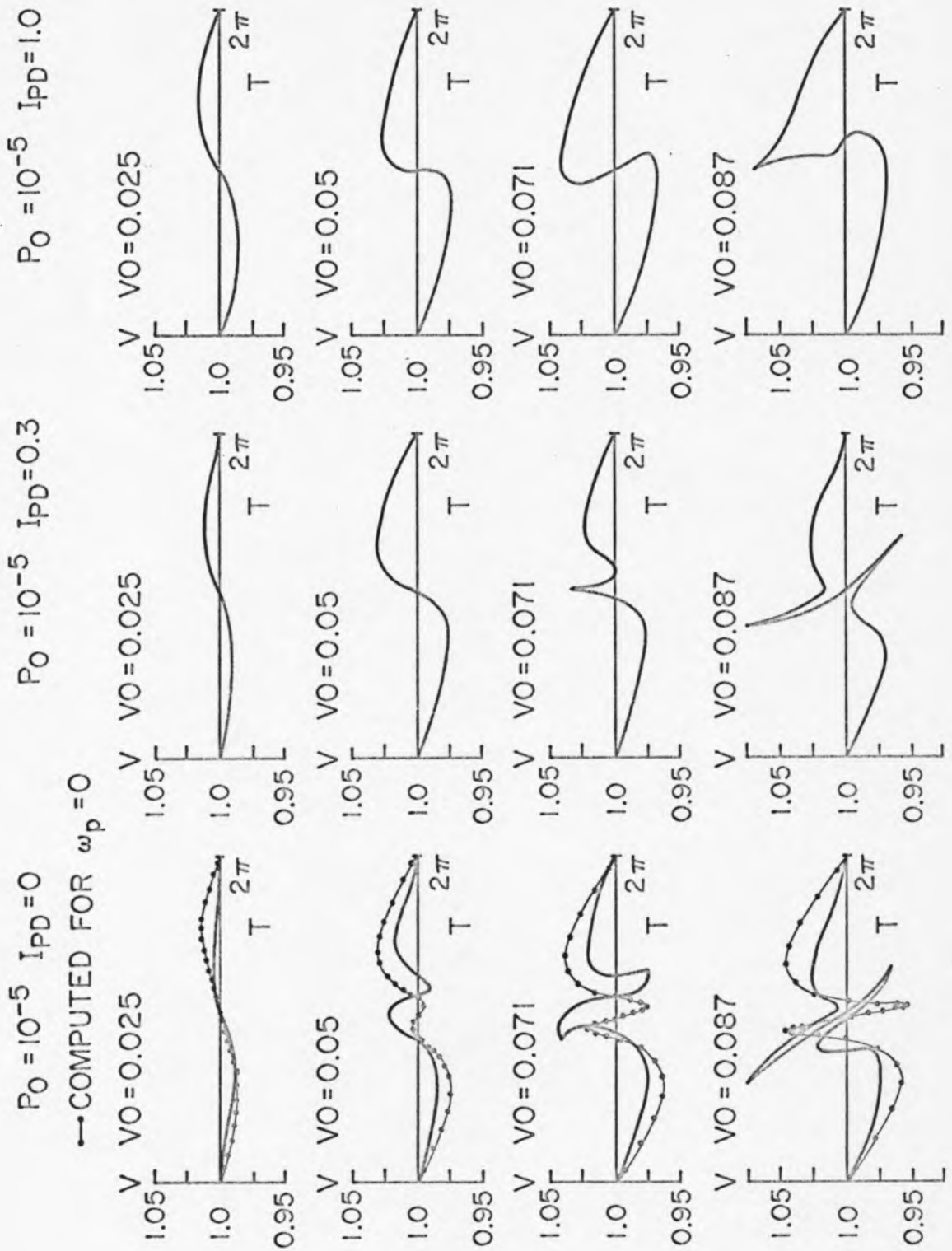


Figure 4.24 Velocity-phase plots for $I_0 = 10$ ma with varying V_0 , and variation of plasma density by changing discharge current.

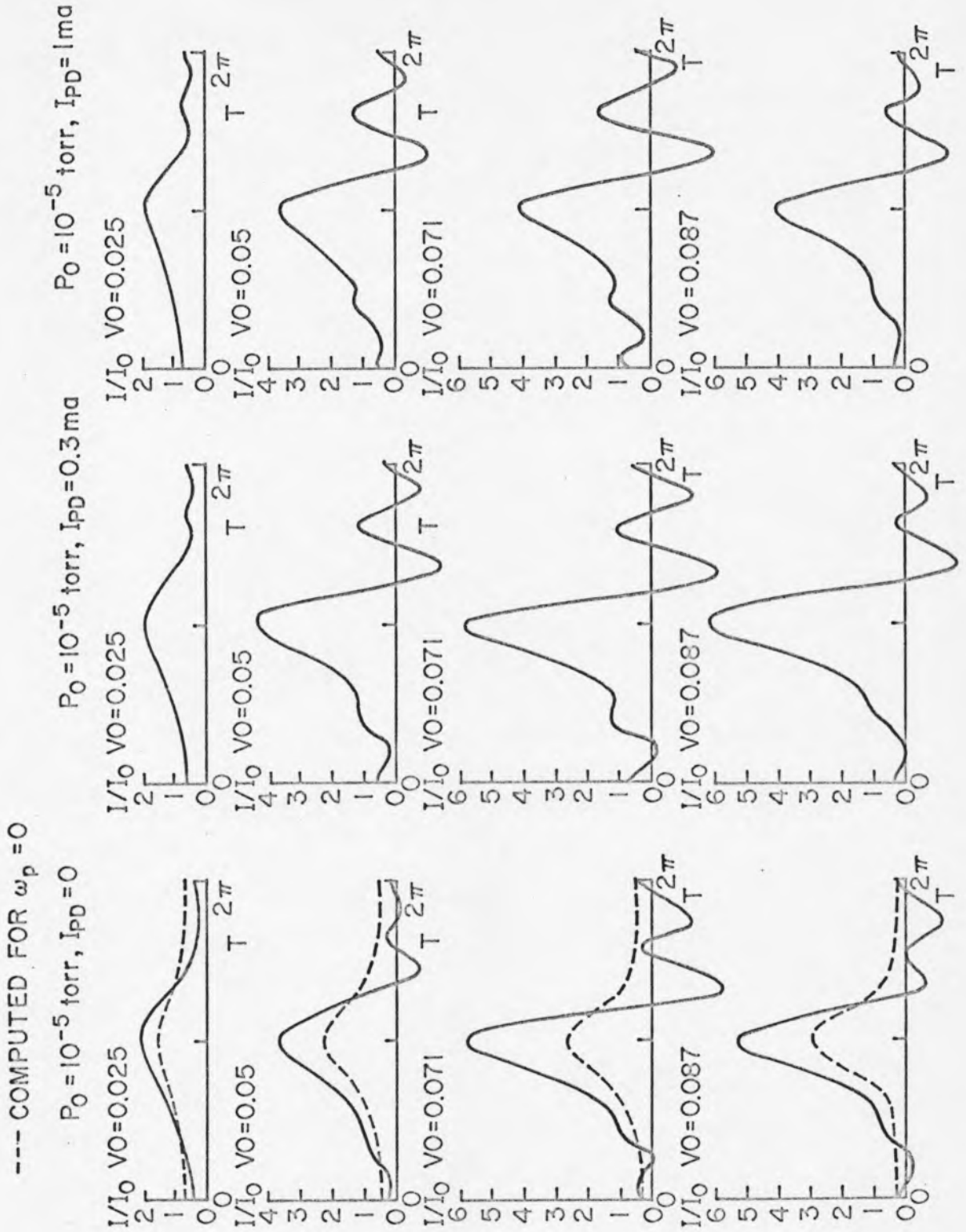


Figure 4.25 Normalized current waveforms for the conditions of Figure 4.24.

theoretical plots shown for the $I_{PD} = 0$ cases are for $\omega_p = 0$. For $I_{PD} = 0$ the $V_0 = 0.025$ velocity-phase plot shows an increase in velocity modulation over that seen in Figure 4.20, as well as an increase in bunching displayed by the current waveform, indicating that for this small degree of initial velocity modulation, the bunching process is enhanced by the increase in plasma density due to a higher p_0 . If the axial plasma density profile were uniform, any enhanced bunching for $\omega/\omega_p > 1$ would have to be accompanied by a decrease in velocity modulation, which is not the case. If the axial plasma density profile is not uniform, and ω/ω_p is less than one in the center region, then the bounding electrons pass first through a region where the forces are attractive and finally through a region of repulsive force. If the tendency to bunch in the first repulsive region is small, the debunching effect of the repulsive space charge will also be small, although the electrons will be bunched less upon entering the region of attractive force than if there were no plasma in that region. If then, the attractive force region is small and the electrons are not bunched upon entry, the electrons will be accelerated toward the bunch, but will leave the region and enter the final repulsive force region without much bunching having occurred. The electron velocities attained in the attractive force region will be sufficient, however, for a higher degree of bunching to occur than would be expected if no plasma were present, and with nearly the same initial velocity modulation. If the degree of initial velocity modulation is too large, the electrons may attain rather tight bunching before entering the region of attractive force, but at the expense of

their tendency to bunch (their relative velocity toward the bunch). Thus the bunch maintains its integrity while traversing the region of attractive force, those electrons which are not a part of the bunch attaining some velocity toward it. Upon entering the final repulsive force region the bunch disintegrates again and electrons are repelled from it, yielding a velocity-phase plot as seen for $V_0 = 0.05$ of the $I_{PD} = 0$ series. The velocity-phase for $V_0 = 0.071$ shows the same sort of behavior except that crossover has just begun to occur, while for $V_0 = 0.087$ crossover has occurred before the beam electrons reach the observation point. As the center plasma frequency is increased, the distance the beam travels in the attractive force region relative to distance traveled in the repulsive force region increases. Therefore, the initial velocity modulation may be greater without causing the beam to be so tightly bunched upon entering the region of attractive force that the beam reaches maximum bunching in the attractive force region, thus causing the bunch to disintegrate upon entering the repulsive region. The three series of Figures 4.24 and 4.25 illustrate this behavior; the velocity-phase plots showing that as I_{PD} is increased (the plasma density is increased) the repulsive force effects diminish for each value of initial velocity modulation. The current waveforms show that maximum bunching occurs for $I_{PD} = 0.3$ ma. The explanation for this is that for $I_{PD} = 0.3$ ma the axial plasma density is distributed in such a way as to impart sufficient velocity modulation to the beam in the attractive space charge region to overcome the severe space charge forces in the repulsive region and achieve bunching, while for $I_{PD} = 0$, or

$I_{PD} = 1.0$ ma, the distribution is such that in the former, insufficient velocity modulation is developed, and in the latter the velocity modulation is too great for the shorter, final region of repulsive force to be effective in bunching, i.e. to convert velocity modulation to density modulation.

The behavior displayed in Figures 4.23, 4.24 and 4.25 constitutes a type of experimental result which can be obtained repeatably with the apparatus used in this investigation. Experiments were also performed at 5 ma, 3 ma, and 1 ma beam current, varying pressure, magnetic field, and discharge current. Qualitatively the results show essentially the same behavior. At 1 ma the changes in behavior are practically unmeasurable, since the space charge forces are insufficient to cause significant variation from ballistic behavior. At 3 ma it is necessary to use the Penning discharge to achieve the indication of the transition from $\omega/\omega_p > 1$ to $\omega/\omega_p < 1$. For the 5 ma beam the transition from $\omega/\omega_p > 1$ to $\omega/\omega_p < 1$ occurs when ω_p is increased by increasing the pressure p_0 , for $p_0 \sim 10^{-4}$ torr, and as in the 10 ma beam behavior and for a slightly lower pressure with some discharge current being drawn. Except for the focussing of the beam and the trapping of the beam-generated plasma, the behavior appears to be independent of the magnetic field up to fields of 300 gauss. The beam does not focus (for the velocity analyzer) well below 70 gauss, and most experiments were performed with approximately 140 gauss, since at this value the beam is easily focussed and the magnet current does not heat the magnet excessively.

Thus experimentally the beam behavior at $Z = 22$ indicates an increase in effective repulsive space charge force for ω/ω_p approaching unity from above, then a gradual decrease in repulsive space charge force to behavior indicating less than normal ($\omega_p = 0$) space charge repulsion. It cannot be definitely said that the experimental results indicate the presence of attractive space charge forces, since in no instance is the degree of velocity modulation observed to be greater than the initial value as predicted by the calculations. The observed behavior, which is qualitatively explained above in terms of an axial plasma density variation, seems reconcilable with the phase trajectory plots of Figure 4.18 computed for an axial plasma density profile. In terms of the interpretation of the behavior seen in Figures 4.24 and 4.25 given above, it would appear that the representation of the axial density profile used for computations is inadequate, since not enough weight is given to the relative lengths of the $\omega/\omega_p > 1$ and $\omega/\omega_p < 1$ regions. In order to check the discrepancies experimentally, measurements are needed as a function of drift distance.

V. CONCLUSIONS

A. Summary and Conclusions

Computations using Gould's analysis of a klystron type beam-plasma amplifier show that when a velocity modulated electron beam traverses a plasma, the forces between electrons are significantly altered and the beam behavior is appreciably modified. When the modulation frequency ω is greater than the plasma frequency ω_p , the electrons repel one another more strongly than with the ordinary Coulomb force and the dependence of the force on electron spacing is also modified. As ω_p increases from zero, the repulsive force between electrons effectively increases, reaching its maximum repulsive effect at plasma resonance ($\omega_p \sim \omega$). As ω_p becomes greater than ω , the force between electrons essentially reverses sign and becomes a force of attraction! Again, the maximum effect is at $\omega_p \approx \omega$. For spacings smaller than a "minimum approach" spacing, which depends on ω/ω_p , the force between electrons remains repulsive, but for greater spacings the electrons attract. In this condition the plasma is said to be an inductive medium and electrons tend to bunch. Thus by introducing such a plasma into the drift space of a klystron type amplifier, the debunching space charge forces which limit efficiency could, in effect, be eliminated. In nearly all cases computed, however, the increase in bunching was accompanied by an increase in the velocity spread of the beam electrons. Thus an increase in bunching efficiency could be lost to a decrease in coupling efficiency, due to this velocity spread.

In terms of the velocity-phase plots and current waveforms which characterize the beam behavior, computations show that for $\omega > \omega_p$, the increase in the repulsive force between electrons has the effect of modifying the beam behavior in the same manner as increasing the beam space charge density. When $\omega < \omega_p$, the beam behaves in a ballistic-like manner (as if the beam space charge density had been decreased) and the percent velocity modulation is increased. Experimental measurements show that for $\omega > \omega_p$, the behavior is modified in the same manner as predicted by the computations and is in reasonable quantitative agreement with the computations. The experimental measurements show no abrupt change in the behavior at $\omega = \omega_p$ as computed, but instead a gradual transition. The experimental observations for $\omega/\omega_p < 1$ do not display the increase in velocity spread which would provide direct evidence of forces of attraction; however, the observed current waveforms and the visually observed intensity modulation seen on the velocity analyzer screen indicate that the high degree of bunching predicted is present. While the absence of an increase in velocity spread is desirable from a device standpoint, it means that a significant difference exists between experiment and analysis.

The experimentally observed beam behavior can be explained in terms of an axial plasma density distribution in a qualitative way by observing the combined effects of increasing plasma density, and changing the initial velocity modulation. If the plasma occupying the drift region has an axial density distribution with a maximum at

the center, and $\omega_p > \omega$ at the central plane, then the beam must pass through three regions; first, a region in which the forces are forces of repulsion; next, a region in which the forces are forces of attraction; and finally, a second region in which the forces are forces of repulsion. Thus, depending on the degree of initial velocity modulation, the relative lengths of the attractive force region and the repulsive force regions, the beam behavior observed at the plane of the collector may exhibit behavior indicative of different space charge conditions for a fixed value of central plasma frequency. The computation based on a model similar to that used by Allen (6) and Chorney (7) tends to support this conclusion. However, this model does not attach the appropriate importance to the relative length of the regions of forces of attraction and forces of repulsion. A qualitative description of the bunching process with optimum axial density distribution and initial electron beam velocity modulation is as follows. In the first region of repulsive force, the beam electrons start to bunch but are inhibited by the increased repulsive forces such that upon entering the region of attractive force, their velocity spread is decreased and the degree of bunching is little altered. In the region of attractive force, the electrons are accelerated to high velocities which tend to bunch them, but before tight bunching occurs, the final repulsive region is entered. Here, the strong repulsive forces again tend to prevent bunching, but the momentum attained by the electrons allows them to overcome these forces and tight bunching does occur, the faster electrons being

decelerated in the process. If the conditions are just right, this process could produce a tightly bunched beam with little spread in velocity as observed experimentally. In fact, for one set of parameters used in computing the behavior with an axial density distribution, 50 percent of the total charge is bunched in a phase interval of 0.1π with 96 percent of these bunched charges having only 20 percent of the initial velocity spread. In terms of this interpretation of the axially varying plasma model, the experimental and computed results display at least qualitatively the same behavior.

A more quantitative investigation requires either measurements as a function of drift distance, or extensive manipulation of the axial density distribution in the computations. Measurements as a function of drift distance would be extremely difficult to perform without disturbing the axial plasma density distribution and the manipulation of the distribution in the computations would be not only costly, but subject to question due to the inability to account for the resonance oscillations which can exist. While the results of the beam plasma investigation indicate that the mechanism would be successful in improving the performance of a klystron type amplifier, the technological difficulties and the beam coupling problems which arise due to the presence of the plasma probably more than offset any gain in performance.

B. Suggestions for Further Work

If further information is to be gained about the bunching process resulting due to the beam-plasma interaction studied here, measurements must be made either with a uniform plasma, or with one in which the axial density distribution is well known. Perhaps the most suitable plasma for this purpose would be a cesium plasma, generated by a device with very low background pressure to minimize the amount of beam generated plasma. This type of plasma was considered at the outset of this investigation, but rejected due to the complexity of the apparatus required for its generation and control. The velocity analyzer should be more versatile in that it should be capable of measuring current as a function of velocity as well as phase. This could be accomplished using a portion of the beam collector as a retarding potential probe and sampling the current (in the sampling oscilloscope sense) as a function of both phase (time) and retarding potential. The apparatus must be capable of high vacuum, 10^{-9} torr or better, to check the $\omega_p = 0$ results and thereby truly determine the plasma effects. This requirement is compatible with the cesium plasma generation, but requires extreme care in the selection of the construction materials and severely complicates the r.f. instrumentation techniques.

APPENDIX A

Equations of Motion for the Electron Beam

In writing the equations of motion the electron beam is characterized by the quantities I_0 the beam current, b the beam radius, V_0 the accelerating voltage, and u_0 the average velocity of the beam electrons. The disc model represents the beam by discs of radius b , mass m , and charge q which leave the electron gun every $2\pi/N\omega$ seconds with velocity u_0 (there are N discs per modulation cycle). Thus the charge q is given by

$$q = \frac{2\pi I_0}{N\omega} \quad (\text{A-1})$$

and the mass m_0 by

$$m_0 = \frac{2\pi I_0 m}{N\omega e} \quad (\text{A-2})$$

where m and e are the electron mass and charge. Defining v_n and z_n as the velocity and position of disc n , the differential equations for the trajectories are

$$\frac{dv_n}{dt} = \sum_{\substack{l \\ m \neq n}}^N a_{nm} \quad (\text{A-3})$$

$$\frac{dz_n}{dt} = v_n \quad (\text{A-4})$$

where $m_0 a_{nm}$ is the force exerted on disc n by another disc m . This force is expressed in terms of the inter-disc spacing, e.g., in Regions I and III of Figure 2.1a by simple exponentials, in Region II

the plasma region, by a table of values computed beforehand for a set of inter-disc spacings covering the range. The evaluation of a_{nm} is discussed in detail in Appendix B.

For computational purposes it is more convenient to work with dimensionless variables and to modify the equations of motion somewhat. In order to observe the behavior of the beam along its path, it is desirable to compute $v_n(z)$ and $t_n(z)$ instead of $v_n(t)$ and $z_n(t)$ so that equations (A-3) and (A-4) are transformed to

$$\frac{dv_n}{dz} = \frac{1}{v_n} \sum_{\substack{1 \\ m \neq n}}^N a_{nm} \quad (\text{A-5})$$

$$\frac{dt_n}{dz} = \frac{1}{v_n} \quad (\text{A-6})$$

The variables are normalized by setting

$$V_n = \frac{v_n}{u_0} \quad (\text{A-7})$$

$$T_n = \omega t_n \quad (\text{A-8})$$

$$Z_n = \frac{\omega z}{u_0} \quad (\text{A-9})$$

To facilitate integration of the equations in this form, it is desirable to express a_{nm} in terms of t_n and t_m . For a small velocity spread

$$|z_n - z_m| \approx v_m |t_n - t_m| \quad (\text{A-10})$$

or

$$|Z_n - Z_m| = V_m |T_n - T_m| \quad (\text{A-11})$$

Writing A-5 and A-6 in terms of the dimensionless variables, one obtains

$$\frac{dV_n}{dZ} = \frac{2\pi}{N} \frac{\omega_{pb}^2}{2} \frac{1}{V_n} \sum_{\substack{1 \\ n \neq m}}^N A_{nm} \quad (A-12)$$

$$\frac{dT_n}{dZ} = \frac{1}{V_n} \quad (A-13)$$

where

$$a_{nm} = \frac{q^2}{\pi \epsilon_0 m_0 b^2} A_{nm} \quad (A-14)$$

and ω_{pb} is in terms of q and m

$$\omega_{pb}^2 = \frac{q^2}{m_0 \epsilon_0} \frac{N\omega}{2\pi^2 u_0 b^2} \quad (A-15)$$

For small signals, V_n is approximately unity so that $T_n \sim Z$.

Hence define $T'_n(Z)$ by

$$T'_n(Z) \equiv T_n(Z) - Z \quad (A-16)$$

and therefore $T'_n(Z)$ is a more slowly varying function of Z than $T_n(Z)$. Now define $G_n(Z)$ by

$$G_n(Z) \frac{dT'_n}{dZ} \equiv \frac{dT_n}{dZ} - 1 \quad (A-17)$$

$$= \frac{1}{V_n} - 1 \quad (A-18)$$

From this the differential equation for $G_n(Z)$ is

$$\begin{aligned} \frac{dG_n}{dZ} &= -\frac{1}{V_n^2} \frac{dV_n}{dZ} \\ &= -\frac{2\pi}{N} \frac{\omega^2}{\omega^2} \frac{1}{V_n^3} \sum_{m \neq n}^N A_{nm} \end{aligned} \quad (\text{A-19})$$

By assuming an ideal velocity modulator (no current modulation) the starting conditions for numerically integrating equation A-19 are determined as $G_n(0) = 0$ and the values of $V_n(0)$ and $T_n(0)$ which also determine $A_{nm}(0)$ are given by

$$T_n(0) = \frac{2n-1}{2} \cdot \frac{2\pi}{N} \quad (\text{A-20})$$

and

$$V_n(0) = 1 - V_0 \sin T_n \quad (\text{A-21})$$

where V_0 is the fractional velocity modulation. V_0 is related to the gap voltage V_1 and the gap factor α by

$$V_0 = 1 - \sqrt{1 + \frac{\alpha V_1}{V_0}} \approx \frac{1}{2} \frac{\alpha V_1}{V_0} \quad (\text{A-22})$$

Equation A-19 is of the form

$$\frac{dy}{dx} = f(u(x), v(x))$$

with $y(0)$, $u(0)$ and $v(0)$ given and therefore lends itself to numerical solution by a Taylor series or Euler method solution of the form

$$y(a+h) = y(0) - hf(u(a), v(a))$$

with the error of the order $h^2 f'(u(a), v(a))$ which is small if the integration step h is small. Thus G_n is given by

$$G_n((m+1)\Delta Z) = G_n(m\Delta Z) - h \frac{d}{dZ} G_n(V(m\Delta Z), T(m\Delta Z)) \quad (A-23)$$

From G_n , V_n is computed by

$$V_n = \frac{1}{1 + G_n} \quad (A-24)$$

Since it is of primary interest to follow the discs belonging to the same cycle as they progress along the beam path, it is of more interest to compute T'_n than T_n . The reason for this is that T'_n is in fact the phase of disc n relative to the phase of a disc emitted at $Z = 0$ at time $t = 0$ with velocity u_0 . Thus T'_n is given in terms of a Taylor series solution in G_n and G'_n

$$T'_n((m+1)\Delta Z) = T'_n(m\Delta Z) + h G_n(m\Delta Z) + \frac{h^2}{2} G'_n(m\Delta Z) \quad (A-25)$$

The trajectories of the discs are thus generated step by step using equations A-23, A-24, and A-25. By this method only the initial velocities and spacings of the discs need be specified and the equations can be integrated along the path. As will be shown in Appendix B, the acceleration term a_{nm} includes forces due to discs belonging to other cycles, both ahead of and behind the point of integration. If the relative phase of a disc changes by large amounts from cycle to cycle, this method of integration is not accurate, since the acceleration due to discs past the point of integration cannot be computed.

Similarly, some error is introduced at the boundaries since a_{nm} is computed assuming the discs in the adjacent cycles are in the same region also. The error is slight, however, due to the exponential dependence.

APPENDIX B

The Acceleration Force Law

The acceleration force law, as has been noted earlier, should be expressible in terms of the disc separation $|z_n - z_m|$ as described in Figure 2.1c. In the vacuum drift regions I and III, the force between disc n and disc m in Figure 2.1c is expressed

$$f_{nm} = - \frac{q^2}{2\pi\epsilon_0 b^2} e^{-k|z_n - z_m|} \quad (B-1)$$

as given by Tien (9). In this relation k is a function of beam radius and Tien has shown that the exponential is a good approximation when

$$k = 2/b \quad (B-2)$$

Thus to evaluate a_{nm} for disc n at z_n the sum of the forces arising from the discs to the right of z_n in terms of $z = |z_n - z_m|$ is

$$\begin{aligned} \sum f_n^+ &= - \frac{q^2}{2\pi\epsilon_0 b^2} \left[e^{-\frac{2z}{b}} + e^{-\frac{2}{b}(z + \frac{2\pi u_0}{\omega})} + e^{-\frac{2}{b}(z + \frac{4\pi u_0}{\omega})} + \dots \right] \\ &= - \frac{q^2}{2\pi\epsilon_0 b^2} e^{-\frac{2z}{b}} \left[1 + e^{-\frac{4\pi u_0}{b\omega}} + e^{-\frac{8\pi u_0}{b\omega}} + e^{-\frac{12\pi u_0}{b\omega}} + \dots \right] \\ &= - \frac{q^2}{2\pi\epsilon_0 b^2} \frac{e^{-\frac{2z}{b}}}{1 - e^{-\frac{4\pi u_0}{b\omega}}} \end{aligned} \quad (B-3)$$

The sum of the forces due to the discs to the left (behind) disc n in terms of z is

$$\begin{aligned}
 \sum f_n &= \frac{q^2}{2\pi\epsilon_0 b^2} \left[e^{-\frac{2}{b}\left(\frac{2\pi u_0}{\omega} - z\right)} + e^{-\frac{2}{b}\left(\frac{4\pi u_0}{\omega} - z\right)} + e^{-\frac{2}{b}\left(\frac{6\pi u_0}{\omega} - z\right)} + \dots \right] \\
 &= \frac{q^2}{2\pi\epsilon_0 b^2} e^{\frac{2z}{b}} e^{-\frac{4\pi u_0}{\omega}} \left[1 + e^{-\frac{4\pi u_0}{b\omega}} + e^{-\frac{8\pi u_0}{b\omega}} + \dots \right] \\
 &= \frac{q^2}{2\pi\epsilon_0 b^2} \frac{e^{\frac{2z}{b}} e^{-\frac{4\pi u_0}{b}}}{1 - e^{-\frac{4\pi u_0}{b}}} \tag{B-4}
 \end{aligned}$$

Writing B-3 and B-4 in terms of the normalized variables, the total force due to all discs corresponding to m and the normalized separation Z becomes

$$\sum f_n^+ + \sum f_n^- = -\frac{q^2}{2\pi\epsilon_0 b^2} \frac{e^{2\alpha Z} - e^{2\alpha(\pi-Z)}}{1 - e^{2\pi\alpha}} \tag{B-5}$$

where Z is $\omega Z/u_0$ and α is $2u_0/b\omega$. The normalized acceleration term A_{nm} can now be written directly in terms of Z as

$$A_{nm} = -\frac{1}{2} \frac{e^{2\alpha Z} - e^{2\alpha(\pi-Z)}}{1 - e^{2\pi\alpha}} \tag{B-6}$$

This is the expression for A_{nm} used for integrating equation A-19 in drift Regions I and III.

In Region II, the plasma region, the computation of A_{nm} is more complex since f_{nm} cannot be written in a simple form as was the case in the vacuum drift regions. It is necessary to start from fundamentals and solve Poisson's equation for the disturbance

potentials arising from the presence of the discs in the plasma. Rather than do this for each necessary computation of A_{nm} , the solutions are carried out for a set of disc separations and tabulated. Hence the force law becomes a table of values in terms of disc separation Z , and interpolation must be used for values of Z not tabulated.

Since only axial motion is considered, the system has cylindrical symmetry and use of Fourier-Bessel transforms is in order. Thus $\tilde{\phi}$ and ϕ are defined by

$$\phi(\rho, z, t) = \frac{1}{(2\pi)^2} \int_{-\infty}^{\infty} \int_{-\infty}^{\infty} \int_0^{\infty} \tilde{\phi}(k_{\perp}, k_z) J_0(k_{\perp} \rho) e^{i(\omega t - k_z z)} k_{\perp} dk_{\perp} dk_z d\omega \quad (B-7)$$

and

$$\tilde{\phi}(k_{\perp}, k_z, \omega) = \int_{-\infty}^{\infty} \int_{-\infty}^{\infty} \int_0^{\infty} \phi(\rho, z) J_0(k_{\perp} \rho) e^{-i(\omega t - k_z z)} 2\pi \rho d\rho dz dt \quad (B-8)$$

In terms of the transform variables, Poisson's equation is

$$-k^2 \tilde{\phi} = - \frac{(\tilde{\rho}_{\text{plasma}} + \tilde{\rho}_{\text{source}})}{\epsilon_0} \quad (B-9)$$

where ρ_{source} represents the disc. The generalized susceptibility $\chi(\omega, \underline{k})$ given by

$$\chi(\omega, \underline{k}) = - \frac{\omega_p^2}{\omega(\omega - i\nu) - k^2 w^2} \quad (B-10)$$

is introduced at this point to relate ρ_{plasma} to the potential $\tilde{\phi}$. The quantities ν and w in B-10 are the plasma electron

collision frequency and thermal speed respectively. In terms of χ and $\tilde{\phi}$, ρ_{plasma} is

$$\tilde{\rho}_{\text{plasma}} = -k^2 \epsilon_0 \chi \tilde{\phi} \quad (\text{B-11})$$

Substituting in Poisson's equation

$$k^2(1 + \chi) \tilde{\phi} = \frac{\tilde{\rho}_{\text{source}}}{\epsilon_0} \quad (\text{B-12})$$

or

$$\tilde{\phi} = \frac{\tilde{\rho}_{\text{source}}}{k^2 K(\underline{k}, \omega) \epsilon_0} \quad (\text{B-13})$$

where $K(\underline{k}, \omega)$ sometimes is called the plasma dielectric constant, and is

$$K(\underline{k}, \omega) = 1 + \chi = 1 - \frac{\omega_p^2}{\omega(\omega - iv) - k^2 v^2} \quad (\text{B-14})$$

For a charged disc of radius b and velocity v , $\tilde{\rho}_{\text{source}}$ is

$$\tilde{\rho}_{\text{source}} = q \frac{2J_1(k_{\perp} b)}{k_{\perp} b} \delta(\omega - k_z v) \quad (\text{B-15})$$

Thus

$$\tilde{\phi}(k_{\perp}, k_z, \omega) = \frac{q \frac{2J_1(k_{\perp} b)}{k_{\perp} b} \delta(\omega - k_z v)}{(k_{\perp}^2 + k_z^2) K(\underline{k}, \omega) \epsilon_0} \quad (\text{B-16})$$

With $z' = z - vt$, B-16 is substituted into B-8 to obtain $\phi(\rho, z')$

as

$$\phi(\rho, z') = \frac{q}{(2\pi)^2 \epsilon_0} \int_{-\infty}^{\infty} \frac{2J_1(k_{\perp} \rho)}{k_{\perp} \rho} \cdot \frac{J_0(k_{\perp} \rho) e^{-ik_z z'} k_{\perp} dk_{\perp} dk_z}{(k^2 + k_z^2) \frac{\omega_p^2}{k_z v(k_z v - iv) - (k^2 + k_z^2) w^2}} \quad (\text{B-17})$$

To calculate the force f_z on another disc located at z

$$\begin{aligned} f_z &= - \frac{\partial}{\partial z} \int \phi(\rho, z - vt) dq \\ &= - \frac{\partial}{\partial z} \frac{q}{b^2} \int_0^b \phi(\rho, z - vt) 2\pi \rho d\rho \end{aligned} \quad (\text{B-18})$$

Since $z - vt$ is just the separation between discs, this is the desired form and

$$\begin{aligned} a(z') &= \frac{f_z}{m_0} \\ a(z') &= - \frac{2q}{m_0 b^2} \frac{\partial}{\partial z} \int_0^b \phi(\rho, z') \rho d\rho \end{aligned} \quad (\text{B-19})$$

Substituting ϕ from equation B-17, integrating with respect to and differentiating with respect to z yields

$$a(z') = \frac{1}{(2\pi)^2} \frac{q^2}{m_0 \epsilon_0} \int_{-\infty}^{\infty} \int_0^{\infty} \left(\frac{2J_1(k_{\perp} b)}{k_{\perp} b} \right)^2 \frac{ik_z e^{-ik_z z'} k_{\perp} dk_{\perp} dk_z}{(k^2 + k_z^2) \left(1 - \frac{\omega_p^2}{k_z v(k_z v - iv) - (k^2 + k_z^2) w^2} \right)} \quad (\text{B-20})$$

Integration with respect to k_z is over the range $-\infty$ to ∞ and the integration is performed in the complex plane by contour integration.

Consider the integral

$$I = \int_{-\infty}^{\infty} \frac{ik_z e^{-ik_z z'} dk_z}{(k_z^2 + k_{\perp}^2) \left(1 - \frac{\omega_p^2}{k_z v(k_z v - iv) - (k_z^2 + k_{\perp}^2)w^2}\right)} \quad (\text{B-21})$$

which can be written in the form

$$I = \int_{-\infty}^{\infty} \frac{ik_z e^{-ik_z z'} (k_z - \alpha_1)(k_z - \alpha_2) dk_z}{(k_z + ik_{\perp})(k_z - ik_{\perp})(k_z - \beta_1)(k_z - \beta_2)} \quad (\text{B-22})$$

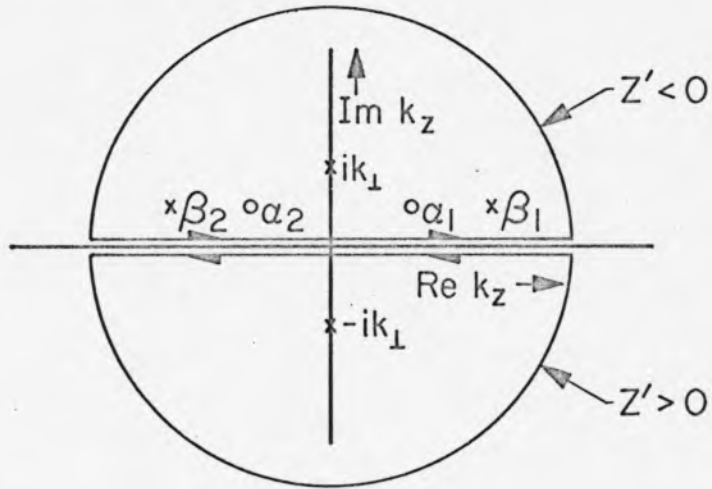
where $\beta_1, \beta_2, \alpha_1$ and α_2 are given by

$$\beta_{1,2} = i \frac{\frac{v}{2v}}{1 - \frac{w^2}{v^2}} \pm \sqrt{\frac{k_{\perp}^2 \frac{w^2}{v^2} + \frac{\omega_p^2}{v^2}}{1 - \frac{w^2}{v^2}} - \frac{(\frac{v}{2v})^2}{(1 - \frac{w^2}{v^2})^2}} \quad (\text{B-23})$$

$$\alpha_{1,2} = i \frac{\frac{v}{2v}}{1 - \frac{w^2}{v^2}} \pm \sqrt{\frac{k_{\perp}^2 \frac{w^2}{v^2}}{1 - \frac{w^2}{v^2}} - \frac{(\frac{v}{2v})^2}{(1 - \frac{w^2}{v^2})^2}} \quad (\text{B-24})$$

The pole-zero configuration in the complex k_z plane for an arbitrary choice of parameters in the integrand of I is shown in Fig. B-1a. Note that for finite collision frequency the poles $\beta_{1,2}$ are always in the upper half plane and that the complex poles are always farther from the imaginary axis than the zeroes. The path of integration is taken around the lower contour for $z' > 0$ and around the upper path for $z' < 0$ to assure that the integrand vanishes on the contour. Thus it is seen that when the test disc at z is ahead of

(a)



(b)

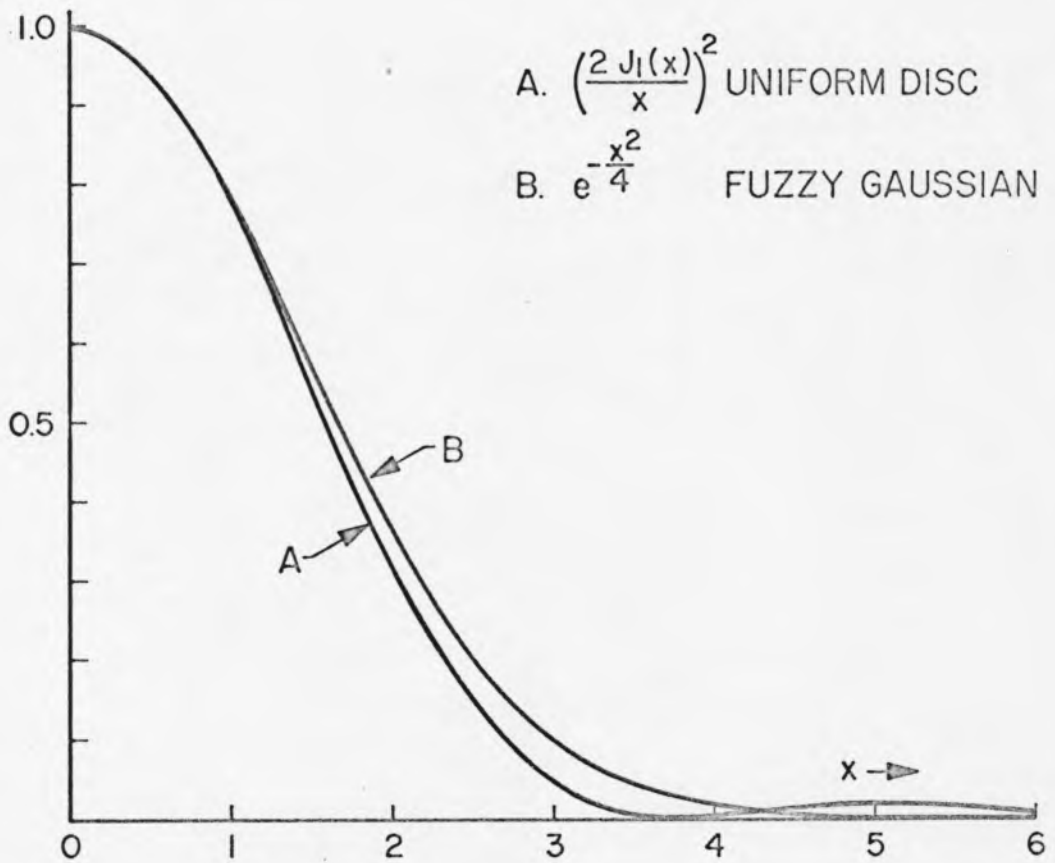


Figure B1. (a) Complex plane pole-zero plot for the integrand of Equation 50

(b) Comparison of the exponential approximation to the Bessel function "weight function".

the disc exerting the force and whose position is vt , $(z - vt) = z'$ is greater than zero and only one pole contributes to the force--this is just the partially screened coulomb force. However, when the test disc at z is behind the disc at vt , three poles contribute to the force thus modifying the coulomb force more radically.

The evaluation of I must consequently be done in two parts.

For $z' > 0$, I is simply

$$I^+ = \frac{\pi e^{-k_{\perp} z'}}{1 + \frac{\omega_p^2}{k_{\perp}^2 v^2 + k_{\perp} v v}} \quad \text{for } z' > 0 \quad (\text{B-25})$$

For $z' < 0$ three poles are involved and the expression for I^- is complicated by the contribution of the complex poles. Rather than discuss I^- at this point, the expression for I^+ is generalized, as was done for the vacuum regions, to include the forces of all discs behind the test disc which can be represented by the spacing z as shown in Figure 2.1c

$$I^+(z) = \frac{\pi e^{-i \frac{2\pi u_0}{\omega} k_{\perp} z}}{(1 - e^{-k_{\perp} \frac{2\pi u_0}{\omega}}) (1 + \frac{\omega_p^2}{k_{\perp}^2 v^2 + k_{\perp} v v})} \quad (\text{B-26})$$

Now B-26 could be substituted into B-20 and integrated numerically.

Instead of doing so, note that the contribution to $I^-(z)$ from the pole at ik_{\perp} will have the same form, hence I^- is divided into I_1^- and I_2^- where I_1^- is the contribution due to the pole at ik_{\perp} and I_2^- is the contribution from the poles at $iA \pm B$. Thus

$$I_1^- = - \frac{\pi e^{k_{\perp} z}}{1 + \frac{\omega^2}{p} \frac{1}{k_{\perp}^2 v^2 - k_{\perp} v v}} \quad (\text{B-27})$$

and

$$I_1^-(z) = \frac{\pi e^{-k_{\perp} z}}{(1 - e^{-k_{\perp} \frac{2\pi u_0}{\omega}}) (1 + \frac{\omega^2}{p} \frac{1}{k_{\perp}^2 v^2 - k_{\perp} v v})} \quad (\text{B-28})$$

Combining B-26 and B-27 and substituting into B-20 obtains $a_1(z)$.

Changing variables with the substitution $x = k_{\perp} b$ and noting in Figure B-1b that the behavior of the Bessel function term is approximately the same as the behavior of the exponential, the normalized acceleration force is expressed in terms of the normalized variables and previous definitions as

$$A_1(z) = \frac{1}{4} \int_0^{\infty} \frac{e^{-\frac{x^2}{4}}}{1 - e^{-\pi \alpha x}} \left\{ \frac{(x^2 + \frac{vb}{u_0} x) e^{-\frac{\alpha}{2}(2\pi - z)x}}{(x^2 + \frac{vb}{u_0} x + \frac{\omega^2 b^2}{u_0^2})} - \frac{(x^2 - \frac{2b}{u_0} x) e^{-\frac{\alpha}{2} z x}}{(x^2 - \frac{2b}{u_0} x + \frac{\omega^2 b^2}{u_0^2})} \right\} x dx \quad (\text{B-29})$$

where $\alpha = 2u_0/b\omega$.

Before proceeding with the evaluation of I_2^- and $A_2(z)$, it is convenient to define several quantities in terms of the poles

and zeroes of the integrand of I defined in B-21. Define

$$\beta_{1,2}^b = iA \pm B \quad (B-30)$$

and

$$\alpha_{1,2}^b = iA \pm E \quad (B-31)$$

Summing the residues at the poles β_1 and β_2 gives the value for I_2^- in terms of A, B and E as

$$I_2^- = -2\pi \operatorname{Re} \left\{ i \frac{B^2 - E^2}{B} \frac{(A + iB) e^{\frac{(A + iB)Z'}{b}}}{k^2 b^2 + B^2 - A^2 - i2AB} \right\} \quad (B-32)$$

Including the contributions due to all corresponding discs ahead of the test disc, normalizing and substituting the exponential for the Bessel function, $A_2(Z)$ is written

$$A_2(Z) = \frac{e^{-\frac{\alpha}{2}AZ}}{2} \int_0^\infty e^{-\frac{x^2}{4} \frac{B^2 - E^2}{B}} \cdot \operatorname{Re} \left\{ \frac{(B - iA) e^{-i \frac{\alpha}{2} BZ}}{(x^2 + B^2 - A^2 - i2AB)[1 - e^{-\alpha\pi(A + iB)}]} \right\} x dx \quad (B-33)$$

This is not the final form for computation, since both B and E contain x, and the real part of the expression within the brackets has yet to be determined. Further manipulation only tends to complicate the expression from the standpoint of obtaining a form in which dependence on electron temperature and collision frequency can be deduced by inspection.

For computational purposes further auxiliary functions are defined to facilitate the numerical integration of $A_1(Z)$ and $A_2(Z)$ and these expressions are integrated using Simpson's rule. The sum of A_1 and A_2 is thus the normalized acceleration force A_{nm} between two discs belonging to the same modulation cycle with $Z_m > Z_n$ and separated by a distance Z . In this way a force table, or force law of values of A_{nm} versus Z , is established for use in integrating the equations of motion. The dependence of this force law on ω/ω_p , T_e , and v is discussed in Chapter IV.

APPENDIX C

The Computer Program

The computer analysis and program used to obtain the theoretical results was developed by Gould as a consultant for Microwave Associates. The flow chart is shown in Figure C1. Starting at point 1, the entry point, data is read which determines the relative lengths of the plasma and vacuum drift regions, the integration step size, and the electron beam characteristics and initial velocity modulation. The length of the plasma drift region is determined by $M2$ so that if $M2 > 0$, a plasma region is included; if not, the computation is simply carried out for the klystron geometry. Taking the $M2 > 0$ branch, the computer reads data which either determines the plasma properties for which an acceleration force law table is computed, or reads a set of acceleration force values from input cards. At this point the integration of the equations of motion can be performed. The initial values of V_i and T_i for the discs representing the beam are determined by the input value of V_0 . For $V_0 > 0$, the V_i and T_i are computed by the relationships given in Appendix A, equations A-20 and A-21. For $V_0 \leq 0$ the V_i and T_i are read in from cards, thus permitting a computation to be continued where an earlier one left off. The remaining blocks integrate the equations of motion for each region, compute the Fourier components of the beam current, and control the output. The output has three forms. The printed output consists of the values of the first three Fourier current components, computed according to equation 2.8 of Chapter IIB and the values of V_i and T_i printed at intervals specified by the

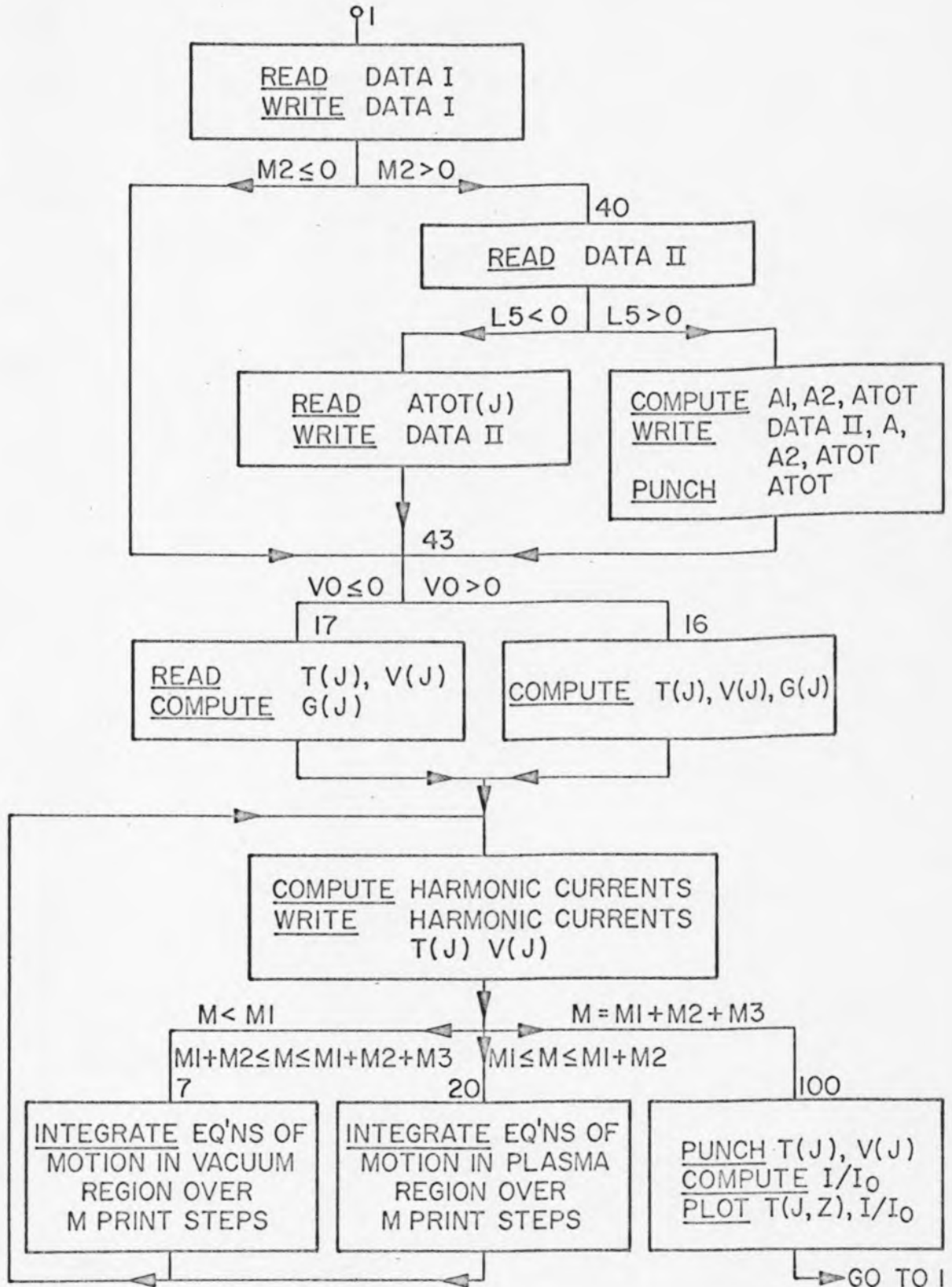


Figure C1. Flow Chart for Computer Program.

input data. After the final integration step, a current waveform is computed as described in Chapter IIB using equation 2.9 and, together with $T_i(Z)$, is plotted in a continuous plot form. The third output is punched on cards and consists of the final values of V_i and T_i and, if an acceleration force is computed, the values of the plasma parameters and of $A_{nm}(Z)$ (called ATOT in the flow chart) are punched on cards also. The V_i and T_i punched on cards may be used as inputs for additional computations, or for convenience in point plotting the velocity-phase plots using the computer. The acceleration force cards may be used in additional calculations for which the plasma parameters are the same.

The program is quite versatile and allows much latitude in the computational study. The execution time in the Fortran IV version is approximately 2-1/2 minutes for 300 integration steps and 32 discs for each set of parameters and only slightly less if the acceleration force in the plasma region is read in from cards. Extensive variation of parameters is thereby costly. In computing a case for an axial plasma density distribution, it is necessary to resubmit the program as many times as the number of plasma regions, reading the exit values of V_i and T_i as inputs to the next region. Hence for this type of investigation the program needs to be modified as done by Allen (6) in the Microwave Associates' computation, to be really useful.

REFERENCES

1. D. Bohm and E. P. Gross, Phys. Rev. 75, 1851 (1949a); 75, 1864 (1949b); 76, 992 (1950c).
2. G. D. Boyd, L. M. Field, R. W. Gould, Phys. Rev. Letters 109, 1393 (1958).
3. G. D. Boyd, R. W. Gould, L. M. Field, Proc. IRE 49, 1906 (1961).
4. E. V. Bogdanov, V. J. Kislov, Z. S. Tchernov, Proc. Symp. on Millimeter Waves 9, 57 (1959).
5. M. A. Allen, G. S. Kino, Phys. Rev. Letters 6, 163 (1961).
6. R. W. Gould, M. A. Allen, Tubes pour Huperfrequencies, Dunod Editeur, Paris, France, 445-49 (1964).
7. M. A. Allen, C. S. Biechler, P. Chorney, Tubes pour Hyperfrequencies, Dunod Editeur, Paris, France, 435-438 (1964); and Bull. Am. Phys. Soc. 11, 575 (1966).
8. J. V. Parker, J. C. Nickel, R. W. Gould, Phys. of Fluids 7, 1489 (1964).
9. P. K. Tien, L. Walker, V. Wolontis, Proc. IEEE 43, 260-277 (1955).
10. S. E. Webber, Trans. IEEE, ED, 98-108 (1958).
11. D. Bohn, D. Pines, Phys. Rev. 85, 338 (1952).
12. T. Moreno, Microwave Transmission Data, Dover, New York (1948), pp. 229-238.
13. E. L. Ginzton, Microwave Measurements, McGraw-Hill Book Company, New York, 1957, pp. 213-217.
14. W. Knauer, Jour. App. Phys. 33, 2093-2099 (1962).
15. C. C. Cutler, Bell Systems Tech. Jour. 35, 841-876 (1956).
16. J. W. Gewartowski, Trans. IEEE, ED, 215-222 (1958).
17. P. Hedvall, Jour. App. Phys. 33, 2426-2429 (1962).
18. D. A. Dunn, S. A. Self, Jour. App. Phys. 35, 113-122 (1964).

19. P. T. Smith, Phys. Rev. 36, 1293 (1931)
20. L. D. Smullin, W. D. Getty, Phys. Rev. Letters 9, 3 (1962).

DOCUMENT CONTROL DATA - R&D

(Security classification of title, body of abstract and indexing annotation must be entered when the overall report is classified)

1. ORIGINATING ACTIVITY (Corporate author) California Institute of Technology Pasadena, California		2 a. REPORT SECURITY CLASSIFICATION	
		2 b. GROUP	
3. REPORT TITLE A NONLINEAR STUDY OF BEAM PLASMA AMPLIFICATION			
4. DESCRIPTIVE NOTES (Type of report and inclusive dates) Technical Report, September 1966			
5. AUTHOR(S) (Last name, first name, initial) POESCHEL, Robert L.			
6. REPORT DATE Sept. 1966	7 a. TOTAL NO. OF PAGES 112	7 b. NO. OF REFS 20	
8 a. CONTRACT OR GRANT NO. Nonr 220(50)	9 a. ORIGINATOR'S REPORT NUMBER(S) TR No. 33		
b. PROJECT NO.	9 b. OTHER REPORT NO(S) (Any other numbers that may be assigned this report)		
c.			
d.			
10. AVAILABILITY/LIMITATION NOTICES Distribution of this report is unlimited.			
11. SUPPLEMENTARY NOTES		12. SPONSORING MILITARY ACTIVITY Office of Naval Research	
13. ABSTRACT The interaction between an electron beam and the plasma oscillations it excites in traversing a plasma region effectively changes the magnitude and direction of the force between beam electrons. This effect has been studied theoretically and experimentally by computing and observing beam electron velocities and phases for a beam which is initially velocity modulated at frequency ω and allowed to drift through a plasma filled region of plasma frequency ω_p . When $\omega > \omega_p$ the force between electrons is repulsive and effectively increases in magnitude as ω approaches ω_p . When $\omega < \omega_p$, the force between electrons becomes a force of attraction, to within a given inter-electron spacing, and the maximum effect is also at the resonance condition $\omega \sim \omega_p$. This property could be used to improve the efficiency of electron bunching in a klystron type amplifier by filling the drift space with a plasma of appropriate density. The beam behavior is studied theoretically by computing in an exact, non-linear manner, the trajectories of a disc model electron beam which traverses a linear, dielectric model plasma. The parameters varied are the beam space charge conditions (beam current), the degree of initial velocity modulation, and the ratio of modulation frequency to plasma frequency (ω/ω_p). Computations show that it is possible to bunch the beam electrons within 85% of delta function bunching under some beam and plasma conditions. The electron beam behavior is studied experimentally by observing the beam electron velocity phase distribution with a crossed-field velocity analyzer, and observing the beam current waveform (density-phase distribution) using a wide-band sampling oscilloscope. Experimental results show essentially the same beam behavior as predicted by computation with some differences			

Security Classification

14.	KEY WORDS	LINK A		LINK B		LINK C	
		ROLE	WT	ROLE	WT	ROLE	WT
	electron beams beam-plasma interaction Nonlinear plasma interaction						

INSTRUCTIONS

1. **ORIGINATING ACTIVITY:** Enter the name and address of the contractor, subcontractor, grantee, Department of Defense activity or other organization (*corporate author*) issuing the report.

2a. **REPORT SECURITY CLASSIFICATION:** Enter the overall security classification of the report. Indicate whether "Restricted Data" is included. Marking is to be in accordance with appropriate security regulations.

2b. **GROUP:** Automatic downgrading is specified in DoD Directive 5200.10 and Armed Forces Industrial Manual. Enter the group number. Also, when applicable, show that optional markings have been used for Group 3 and Group 4 as authorized.

3. **REPORT TITLE:** Enter the complete report title in all capital letters. Titles in all cases should be unclassified. If a meaningful title cannot be selected without classification, show title classification in all capitals in parenthesis immediately following the title.

4. **DESCRIPTIVE NOTES:** If appropriate, enter the type of report, e.g., interim, progress, summary, annual, or final. Give the inclusive dates when a specific reporting period is covered.

5. **AUTHOR(S):** Enter the name(s) of author(s) as shown on or in the report. Enter last name, first name, middle initial. If military, show rank and branch of service. The name of the principal author is an absolute minimum requirement.

6. **REPORT DATE:** Enter the date of the report as day, month, year; or month, year. If more than one date appears on the report, use date of publication.

7a. **TOTAL NUMBER OF PAGES:** The total page count should follow normal pagination procedures, i.e., enter the number of pages containing information.

7b. **NUMBER OF REFERENCES:** Enter the total number of references cited in the report.

8a. **CONTRACT OR GRANT NUMBER:** If appropriate, enter the applicable number of the contract or grant under which the report was written.

8b, 8c, & 8d. **PROJECT NUMBER:** Enter the appropriate military department identification, such as project number, subproject number, system numbers, task number, etc.

9a. **ORIGINATOR'S REPORT NUMBER(S):** Enter the official report number by which the document will be identified and controlled by the originating activity. This number must be unique to this report.

9b. **OTHER REPORT NUMBER(S):** If the report has been assigned any other report numbers (*either by the originator or by the sponsor*), also enter this number(s).

10. **AVAILABILITY/LIMITATION NOTICES:** Enter any limitations on further dissemination of the report, other than those

imposed by security classification, using standard statements such as:

- (1) "Qualified requesters may obtain copies of this report from DDC."
- (2) "Foreign announcement and dissemination of this report by DDC is not authorized."
- (3) "U. S. Government agencies may obtain copies of this report directly from DDC. Other qualified DDC users shall request through _____."
- (4) "U. S. military agencies may obtain copies of this report directly from DDC. Other qualified users shall request through _____."
- (5) "All distribution of this report is controlled. Qualified DDC users shall request through _____."

If the report has been furnished to the Office of Technical Services, Department of Commerce, for sale to the public, indicate this fact and enter the price, if known.

11. **SUPPLEMENTARY NOTES:** Use for additional explanatory notes.

12. **SPONSORING MILITARY ACTIVITY:** Enter the name of the departmental project office or laboratory sponsoring (*paying for*) the research and development. Include address.

13. **ABSTRACT:** Enter an abstract giving a brief and factual summary of the document indicative of the report, even though it may also appear elsewhere in the body of the technical report. If additional space is required, a continuation sheet shall be attached.

It is highly desirable that the abstract of classified reports be unclassified. Each paragraph of the abstract shall end with an indication of the military security classification of the information in the paragraph, represented as (TS), (S), (C), or (U).

There is no limitation on the length of the abstract. However, the suggested length is from 150 to 225 words.

14. **KEY WORDS:** Key words are technically meaningful terms or short phrases that characterize a report and may be used as index entries for cataloging the report. Key words must be selected so that no security classification is required. Identifiers, such as equipment model designation, trade name, military project code name, geographic location, may be used as key words but will be followed by an indication of technical context. The assignment of links, roles, and weights is optional.